

Chapter 1

INTRODUCTION

1.1. Background

Atmospheric corrosion is the degradation and gradual destruction of a steel material and its vital properties due to electrochemical reactions of its surface with the elements of the atmosphere surrounding the material. Corrosion changes the micro structure and drastically reduces the mechanical strength and useful life of the steel materials. The effects of atmospheric corrosion process enhance a problem significantly. Furthermore, everyday it encounters with form of degradation, costly maintenance, and expensive overdesign. It can also endanger safety and hinder technological progress. Since the corrosion damages the material of the structures in outside condition, the studies about the corrosion process had paid special attention from the researchers.

Mietz and Bernd, 1996, studied the potential mapping technique, i.e. measuring half-cell potentials at concrete surfaces with reference electrodes to obtain information about the actual state of rebar corrosion. The security aspects as well as economic reasons it is desirable to localize reinforcement corrosion at an early stage and with non-destructive techniques in order to initiate the necessary re- habilitation measures

in time. Potential mapping and plotting of iso-potential values is the most effective method of assessing the results from the use of the technique since reliable diagnosis of corrosion activity depends on assessment of potential differences and rate of potential change more than absolute potential values. The potential measurement can be modified by additionally applying a short anodic pulse by means of a small counter electrode and a galvanostatic.

Shamsad Ahmad, 2003, studied the reinforcement corrosion in concrete structures comprised of the mechanism of reinforcement corrosion, techniques utilized to monitor reinforcement corrosion and methodologies for the prediction of remaining service life of structures. Prediction of the remaining service life of a corroding reinforcement concrete structure can be done by the empirical models and experimental methods.

Ha-Won Song and Saraswathy, 2007, identified the methods and any possible durability problems for corrosion monitoring of reinforced concrete structures by reviewing all the electrochemical and nondestructive techniques from the point of view of corrosion assessment and their applications to bridges, buildings and other civil engineering structures. The maximum information about the corrosion state of rebar in a particular structure would be recommended by using a combination of measuring techniques.

Morcillo et al, 2011, studied the characteristic of corrosion products, kinetics and mechanisms of the corrosion process, the morphology of steel rust and long-term atmospheric corrosion. This study presented the goodness of exponential law to predict long-term atmospheric corrosion in a view of two layered structures that formed the corrosion products on mild steel long-term exposed to atmosphere.

Xiangli Wen et al, 2018, studied the progress regarding carbon steel corrosion products and its classification, their effects on the subsequent corrosion process, their dependence on the initiation, growth, transformation processes in H₂S environments, and the corrosion behavior of carbon steels under wet H₂S environments.

M.T. Kesim et al, 2018, investigated the effect corrosion, oxidation, erosion behavior, and arcing to performance of Ag/W as composite materials as conductor in low voltage circuit breakers. The comparison between oxidation and corrosion behaviors of pure metal, pure Ag and pure Ag in actual contact are in quite good agreement.

In addition, many researchers develop the sensors to detect the atmospheric corrosion using a radio-frequency identification (RFID) sensor, passive wireless sensor, corrosion potential sensor and the other atmospheric corrosion monitoring such as ACM. Alamin et al, 2016, presented the novel use of RFID technology as a sensor for corrosion detection. The RFID corrosion sensor operates according to the principles of electromagnetic induction from the coated and uncoated mild steel plates, which have rectangular regions that have been exposed to the environment for different durations to create different levels of corrosion and it distinguish all the different levels of corrosion. Zhang et al, 2016 investigated the balance of sensing and positioning of RFID sensors for corrosion detection by analyzing real and imaginary parts of the complex impedance. Maria Yasri et al, 2014, designed the UHF wireless corrosion sensor based on the coupling between wide band antennas and an active multi resonator by interrogating the sensor with multi frequency signal. Perveen et al demonstrated a passive wireless corrosion potential sensor design and encapsulation suitable for long-term installed monitoring on a PCB. It detected corrosion potential

by tracking sensor resonant frequency with a resolution of less than 10 mV and an uncertainty of 50 mV. The accelerated corrosion test results for embedded sensors in new and existing structure show a linear relationship between the corrosion potential and the sensor resonant frequency shift. T. Dara et al and T.S, Araceli et al in 2016 were using atmospheric corrosion monitoring (ACM) to investigate the behavior of corrosion product on low carbon steel.

Beside developing the sensors, several techniques for atmospheric corrosion monitoring such as weight and thickness loss, electrochemical impedance spectroscopy (EIS), scanning electron microscope (SEM) and X-ray diffraction (XRD) are necessary to used.

Ridha et al 2013 in Aceh Indonesia, Palsson et al 2016 in Thailand, L. Thi et al 2016 in Vietnam and Tadashi Odara et al 2016 in Japan were using the thickness and weight loss to determine the corrosion loss and the corrosion rate in their countries. Shitanda et al 2009, C. Li et al 2010 and Ch. Tee et al 2015 studied on corrosion monitoring technique based on electrochemical impedance spectroscopy. W. Hu et al 2011 and J. Lue et al 2016 studied on corrosion monitoring technique based on SEM to investigate the morphology of the corrosion. N. Zhang et al 2015 and W.K. Jun Hua Dong et al 2016 were using the XRD to identify the material content of corrosion.

In addition to these techniques, electrochemical methods are useful because they allow in situ corrosion monitoring. However, precise monitoring is difficult because electrochemical methods are very sensitive to corrosion reactions. Once an electrode begins to corrode, the redox reactions of the corrosion products affect the current density signals. In the case of steel, ferrous and ferric ions coexist in the corrosion product. These factors ultimately prevent precise evaluation of atmospheric corrosion.

Thus, a highly accurate in situ sensor capable of monitoring atmospheric corrosion is needed. The sensor for the atmospheric corrosion monitoring that the author focus on is atmospheric corrosion monitoring based on strain measurement.

1.2. Atmospheric Corrosion Sensor based on Strain Measurement (ACSSM)

The study on strain measurement has a widely used in corrosion monitoring especially using the sensors such as strain gauge and fiber optic sensor (FBG). Many researchers also investigated various characteristics of corrosion product/rust.

O. Almubaied et al, 2017 studied on monitoring corrosion process of reinforced concrete tructure using FBG sensor and provided indicative change in wavelength shift due to propagation of concrete cracks.

C.H. Tan et al, 2017 developed the early corrosion detection for structural health monitoring by monitoring rebar corrosion via FBG bare and coated. The sensors were embedded on the specimen to monitor the expansion strain caused by rebar corrosion, and their performances were monitored by observing the Bragg wavelength shift.

M.R.A. Hassan et al, 2012 developed the testing of an optical-based sensor for monitoring the corrosion of reinforcement rebar via an etched cladding Bragg grating. Progression of corrosion can be sensed by observing the reflected wavelength shift of the FBG sensor. In addition, with an increase in fringe pattern and continuously, step-like drop in power of the Bragg reflected spectrum was also displayed

W. Chen et al, 2012 modified the wavelength-strain coefficient of FBG for the prediction of steel bar corrosion embedded in concrete using a cylindrical and elastic model to analyze the strain distribution of a steel bar embedded in the concrete, and obtained a new relation between the Bragg wavelength shift of the FBG wrapped

around the steel bar and the axial strain of the fiber. With this modified coefficient the corrosion of the steel bar embedded in the concrete can be predicted more accurately

Martines et al, 2009 presented the corrosion potential, electrical resistance and corrosion rates data of several examples of reinforcement corrosion monitoring by embedded sensors in concrete structures with a methodology to obtain a representative corrosion rate. It can be used for corrosion predictive models to calculate the remaining time life

K. Al Handawi et al, 2016 , developed and tested the sensor based on strain of FBG sensor and strain gauge for real-time corrosion rate monitoring in pre-stressed structures. This property was exploited to detect thickness changes in pre-stressed mild steel specimens in a double bending configuration under an electrochemically excited corrosion reaction. The reaction was accelerated by galvanostatic electrolysis to the specimens as anodes, while graphite rods serve as cathodes. The strain was logged using fiber optic Bragg grating technology and conventional electrical strain gages simultaneously.

Grattan et al, 2009 conducted the monitoring of corrosion in structural reinforcing bars to perform the comparison using fiber optic and strain gauge in situ monitoring system. By undertaking a series of tests over prolonged periods, coupled with acceleration of corrosion, the performance of fiber Bragg grating-based sensor systems attached to high tensile steel reinforcement bars, and cast into concrete blocks was determined, and the results compared with those from conventional strain gauges where appropriate.

In addition, new method to develop the atmospheric corrosion monitoring based on strain measurement that had lot of noise because of measuring the very small signal,

the a highly accurate in situ sensor is needed. However, in actual applications, there is significant noise due to variations in temperature and other factors during field measurements. Therefore, the purpose of this study is to develop an amplifier circuit for atmospheric corrosion monitoring based on strain measurement by using the active dummy method, which has high sensitivity and can reduce the effect of temperature on the measurement environment. A dummy circuit compensated for the temperature drift in the signal with an active circuit was successfully designed, and experiments involving galvanostatic electrolysis were conducted by using the amplifier circuits to determine the thinning of test pieces through strain measurements.

The author in 2017 developed ACSSM with an active dummy method using strain gauges. Because the accuracy of measurements collected by atmospheric corrosion sensor with strain gauge depends on the thermal strain generated by the effects of environmental temperature drift, the configuration of active and dummy strain gauges to accurately measure the thickness reduction in low-carbon steel test pieces was compared with the analytical results obtained by the finite element method (FEM). An experiment with the proposed strain gauge configuration was then carried out galvanostatic electrolysis and under dry wet condition. The ACSSM using FBG sensors also were presented in this doctoral study with carried the experiment of Galvanostatic electrolysis and under dry wet condition. The ACSSM would be appropriate for atmospheric corrosion monitoring in many types of structures.

1.3. Objectives

The main objectives of this study are to explore the strain behavior due to the corrosion by making the fundamental method to measure the atmospheric corrosion monitoring by measuring the thickness of test piece with strain measurement which it

measures very small signal with $S/N < 1$ and very affected by environmental condition. The two design sensors had developed to realize the main objectives of this study. The design of the atmospheric corrosion sensor based on strain measurement with an active dummy method using the strain gauges and FBG sensors can compensate the environmental effect especially the temperature effect which has a large effect on strain measurement. Using finite element method to observe the best configuration the sensors on the test piece before and after the corrosion occur gives the strengthen methodology in ACSSM system. The improvement accuracy of the atmospheric corrosion monitoring by measuring the thickness of test piece with strain measurement was investigated using FBG sensors. To simulate the atmospheric corrosion monitoring with the rust / corrosion product and observe the characteristic of the corrosion phenomena with rust in larger environmental variation the experiment under dry wet condition was conducted by describing the evolution of the corrosion product in mechanism of corrosion behavior based on strain measurement. Figure 4 presents research flow chart of ACSSM study

Mainly, the purpose of this study is to develop an amplifier circuit for atmospheric corrosion monitoring based on strain measurement by using the active dummy method, which has high sensitivity and can reduce the effect of temperature on the measurement environment. A dummy circuit that compensated for the temperature drift in the signal with an active circuit was successfully designed, and experiments involving Galvano static electrolysis and under dry wet condition were conducted by using the ACSSM to determine the thinning of test pieces through strain measurements.

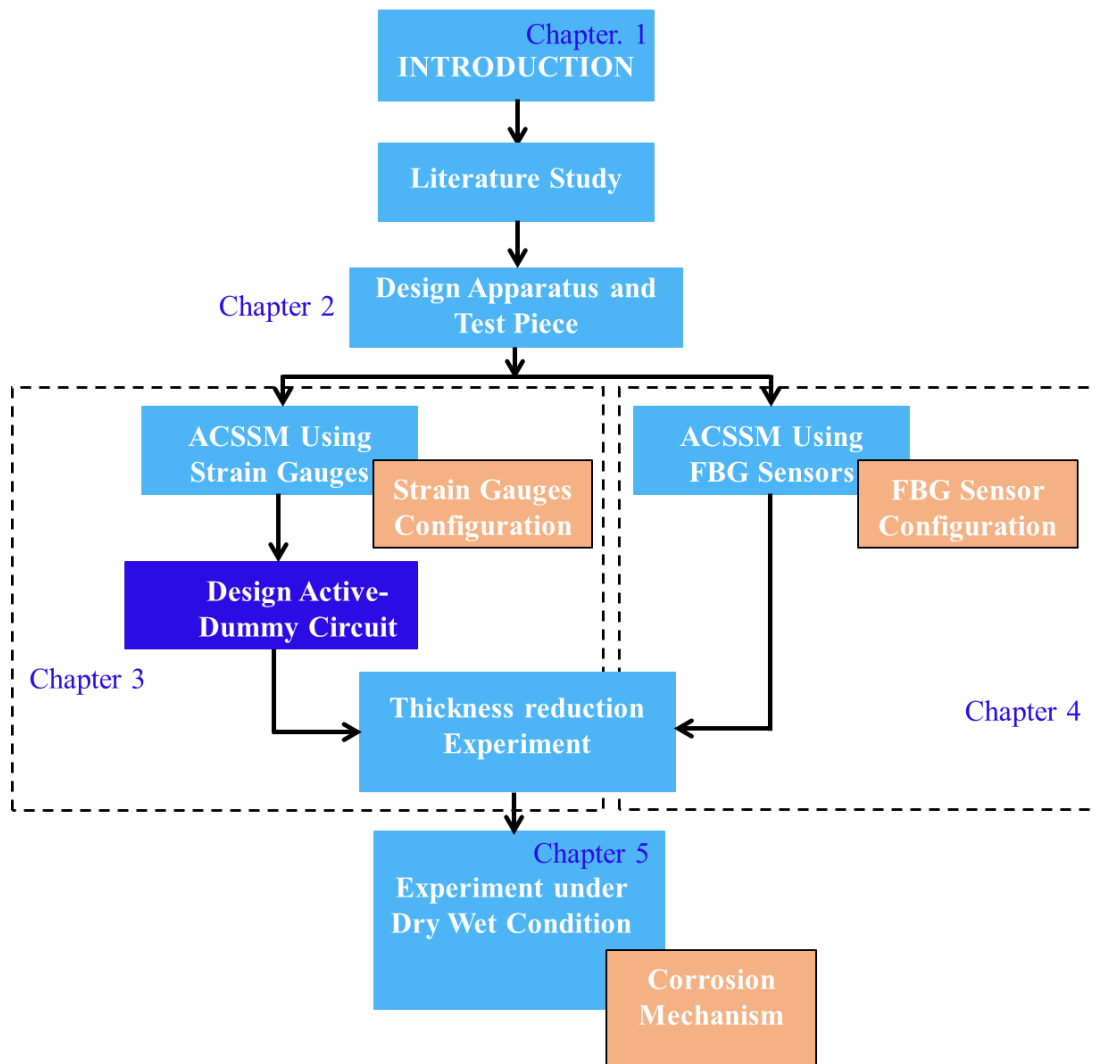


Figure 1.1 Research flow chart of ACSSM study

1.4. The Outline of Dissertation

The outline of the dissertation is assembled into 6 chapters. **Chapter 1** presents the background of this study related to the corrosion and atmospheric corrosion sensor technical issues. The atmospheric corrosion is necessary to be studied further in order to reduce the risk due to the corrosion. In addition, the ACSSM is proposed by investigating the evolution of the corrosion behavior in relationship between the strain

and thickness reduction of the low-carbon steel. The objectives and the short research flow chart are present in this chapter.

Chapter 2 presents a summary review of relevant literature to the principle of atmospheric corrosion monitoring sensor based on strain measurement with an active dummy method including strain in bending, the design circuit of ACSSM using strain gauges that is core of the research, finite element method to strengthen the methodology, the concept of active dummy method that emphasizes the temperature effect in strain measurement and the ACSSM using FBG sensors to improve the accuracy of strain measurement.

Chapter 3 presents a performance of ACSSM with an active dummy method using strain gauges in the electrolysis process, the initial result that show the relationship between temperature vs strain before the electrolysis process and the behavior of strain due to the corrosion after applied the constant current in electrolysis experiment.

Chapter 4 presents a performance of ACSSM with an active dummy method using FBG sensors in the electrolysis process, the initial result that show the relationship between temperature vs strain before the electrolysis process and the behavior of strain due to the corrosion after applied the constant current in electrolysis experiment.

Chapter 5 presents the performance of ACSSM with an Active dummy method using strain gauges and FBG sensors in experiment under dry wet condition. The evolution of the corrosion product on the test piece is conducted by the experiment with dry-wet method by applying 5% NaCl solution to the test piece in order to investigate the performance of ACSSM with an active dummy method. Besides, the

thickness obtained from weight loss of coupons is carried out simultaneously. The mechanism of corrosion behavior based on strain measurement is presented.

Chapter 6 presents the last chapter summarizes the substantial results obtained from this study regarding ACSSM with an active dummy method during the electrolysis process and experiment under dry wet condition using strain gauges and FBG sensors. The future research and recommendation are presented.

Chapter 2

Principle of ACSSM

2.1 Introduction

The ACSSM with an active dummy method comprises the apparatus and test piece, strain measurement circuit that consist of active, dummy and differential circuit and sensor its self, using strain gauges or FBG sensors. This chapter describes the basic of mechanical design of apparatus and test piece by calculating the radius of curvature for strain under bending condition. The relationship between strain and thickness reduction was obtained. The configuration of sensor in the test piece can be determined by FEM simulation. The test piece in bending condition and after thickness reduction of the test piece were simulated, the distribution of strain on the test piece is presented by FEM simulation.

The design of strain measurement circuit for ACSSM with an active dummy method involved the concept of active dummy method using strain gauges, the bridge circuit concept, the instrumentation stage amplifier circuit for amplification of active and dummy signal and the differential circuit concept. The output of the circuit is the voltage. To convert the voltage to the strain, the test for Voltage vs Strain was conducted. The temperature effect to the strain was investigated. To increase the accuracy of the sensor, the ACSSM using FBG sensor is carried out.

2.2. Strain under Bending

The principle of the ACSSM is a measurement of the thickness reduction in a test piece using the mechanical theory of deformation, as shown in Figure 2.1. A test piece with a thickness h is deformed elastically according to the radius of curvature (ρ) and the center angle $d\theta$. The neutral plane (N-N) is unaltered by the deformation. The shortened curvature in the compressed strain position (C-C) where the FBG sensor is installed is equal to $(\rho - \frac{h}{2})d\theta$. The strain ε on the compressed surface can be expressed by:

$$\varepsilon = \frac{l - l_0}{l_0}$$

$$\varepsilon = \frac{\overline{(C - C)} - \overline{(N - N)}}{\overline{(N - N)}}$$

$$\varepsilon = \frac{(\rho - \frac{h}{2})d\theta - \rho d\theta}{\rho d\theta}$$

$$\varepsilon = \frac{(\rho - \frac{h}{2}) - \rho}{\rho}$$

$$\varepsilon = -\frac{h}{2\rho} \dots\dots\dots (2.1)$$

Where l_0 is curvature length before bending and l is curvature length after bending. When the thickness of the test piece decreases due to corrosion, the distance between the neutral plane and the surface of the test piece changes, as shown in Figure 1(b).

From Equation (1), the change in strain $\Delta\varepsilon$ is expressed by:

$$\varepsilon' = \frac{\overline{(C' - C')} - \overline{(N' - N')}}{\overline{(N' - N')}}$$

And

$$h' = h - \Delta h$$

$$\varepsilon' = \frac{\left(\left(\rho - \frac{\Delta h}{2} \right) - \frac{h'}{2} \right) d\theta - \left(\rho - \frac{\Delta h}{2} \right) d\theta}{\left(\rho - \frac{\Delta h}{2} \right) d\theta}$$

$$\varepsilon' = \frac{\left(\left(\rho - \frac{\Delta h}{2} \right) - \frac{(h - \Delta h)}{2} \right) d\theta - \left(\rho - \frac{\Delta h}{2} \right) d\theta}{\left(\rho - \frac{\Delta h}{2} \right) d\theta}$$

$$\varepsilon' = \frac{\left(\rho - \frac{\Delta h}{2} \right) d\theta - \frac{(h - \Delta h)}{2} d\theta - \left(\rho - \frac{\Delta h}{2} \right) d\theta}{\left(\rho - \frac{\Delta h}{2} \right) d\theta}$$

$$\varepsilon' = \frac{-(h - \Delta h)}{\rho - \frac{\Delta h}{2}}$$

$$\varepsilon' = -\frac{(h - \Delta h)}{2\rho - \Delta h} \dots\dots\dots (2.2)$$

From Equation 2.1 and 2.2

$$\Delta\varepsilon = \varepsilon - \varepsilon'$$

$$\Delta\varepsilon = -\frac{h}{2\rho} - \left(-\frac{(h - \Delta h)}{2\rho - \Delta h} \right)$$

$$\Delta\varepsilon = \frac{-h(2\rho - \Delta h) + 2\rho(h - \Delta h)}{2\rho(2\rho - \Delta h)}$$

$$\Delta\varepsilon = \frac{-2\rho h + h \cdot \Delta h + 2\rho h - 2\rho \Delta h}{2\rho(2\rho - \Delta h)}$$

$$\Delta\varepsilon = \frac{h \cdot \Delta h - 2\rho \cdot \Delta h}{2\rho(2\rho - \Delta h)}$$

$$\Delta\varepsilon = \frac{-\Delta h (2\rho + h)}{2\rho(2\rho - \Delta h)}$$

$$\Delta\varepsilon = -\frac{\Delta h}{2\rho} \dots\dots\dots (2.3)$$

$$\rho \gg h$$

$$\Delta\rho \gg h$$

The change in strain of the concave surface determines the change in thickness of the test piece under constant ρ according to Equation (2.3). Equation (2.3) can be transformed into Equation (2.4).

$$\Delta h = -2\rho \Delta\varepsilon \dots\dots\dots (2.4)$$

Equation (2.4) is the important equation to calculate the thickness of the test piece from the strain measurement.

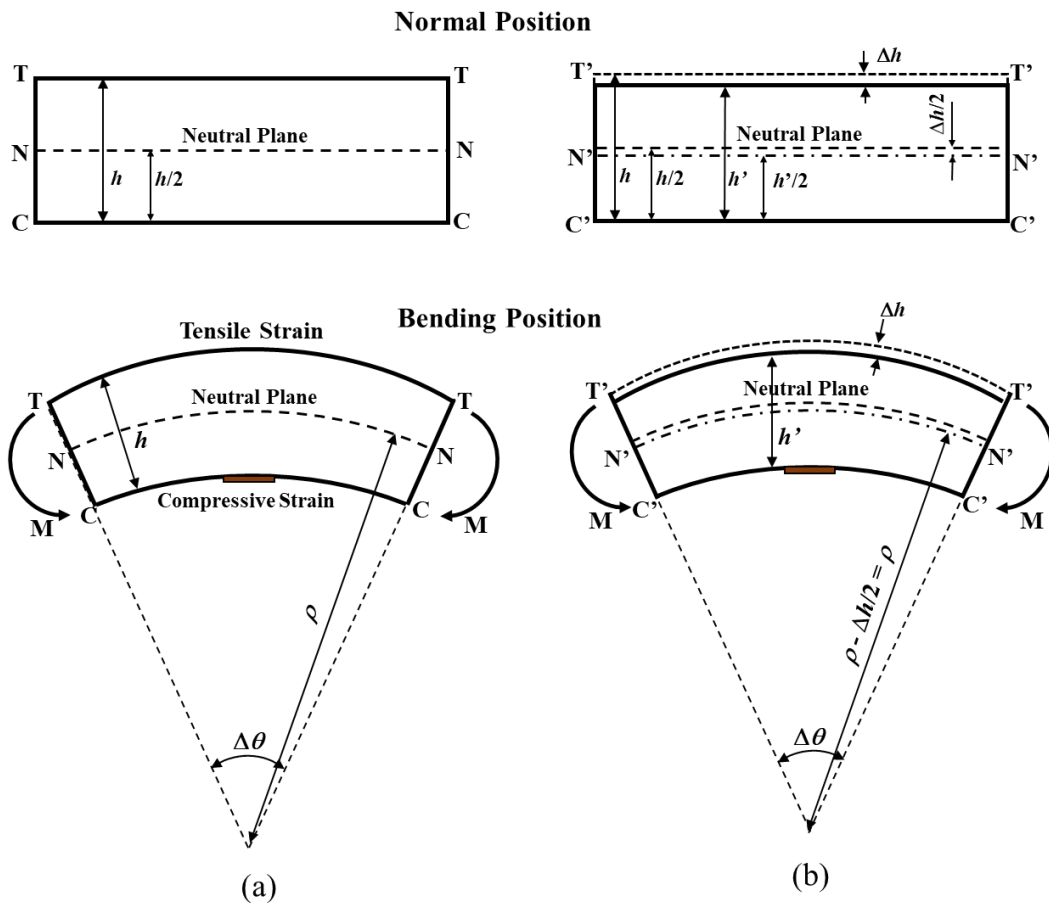


Figure 2.1 The illustration of test piece in normal position and bending position: (a) non-corroded test piece, (b) corroded test piece

2.3. FEM Simulation for ACSSM

FEM simulation is necessary to determine the configuration of the sensor on the test piece. Using the commercial finite element software (ANSYS Mechanical APDL 18.2 from ANSYS Inc.), simulation for accurately measuring the thickness reduction in low-carbon steel test piece was conducted. Figure 2.2 shows the geometry of the test piece and the analytical boundary condition of the full model of the test piece. The analytical conditions include a Young's modulus of 210 GPa, a Poisson ratio of 0.3, elastic deformation conditions and an isotropic material. The element type was SOLID186 which is a hexahedral element with 20 nodes. The displacement z at the node of the test piece at $x = 0$ was fixed to 0 along the y -axis. The x and z coordinates of the test piece had a ρ 430 mm, which was calculated and applied as the boundary condition. The accuracy of measurements obtained by using ACSSM with FBG sensors is affected by thermal strain. The z displacement was determined according to the equation below:

$$z = -\rho + \sqrt{\rho^2 - x^2} \quad \dots\dots\dots (2.5)$$

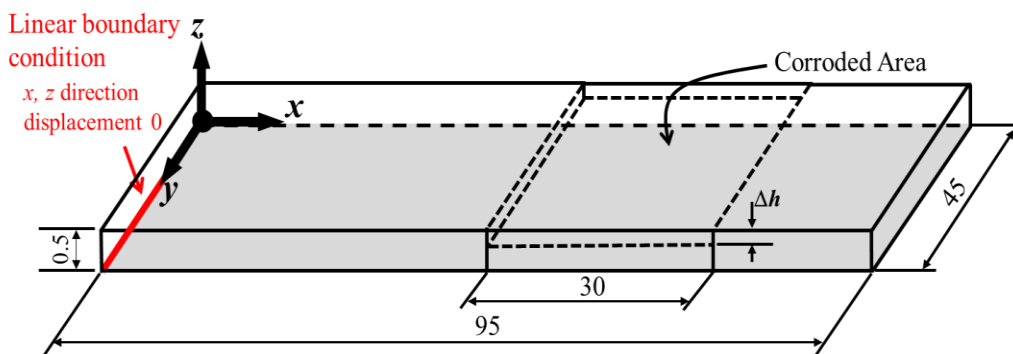


Figure 2.2 The test piece model and boundary condition

Figure 2.3 shows the strain distribution simulated by FEM at upper side and back side of the test piece in bending position. The strain in range $-620 \mu\epsilon$ to $620 \mu\epsilon$, for the

back side is $-569 \mu\epsilon$ to $640 \mu\epsilon$ and the upper side is $556 \mu\epsilon$ to $677 \mu\epsilon$. The back side of the test piece shows compressive strain, and the upper side of the test piece shows tensile strain. For ACSSM, the sensors are installed in back side of test piece and it applied the compressive strain.

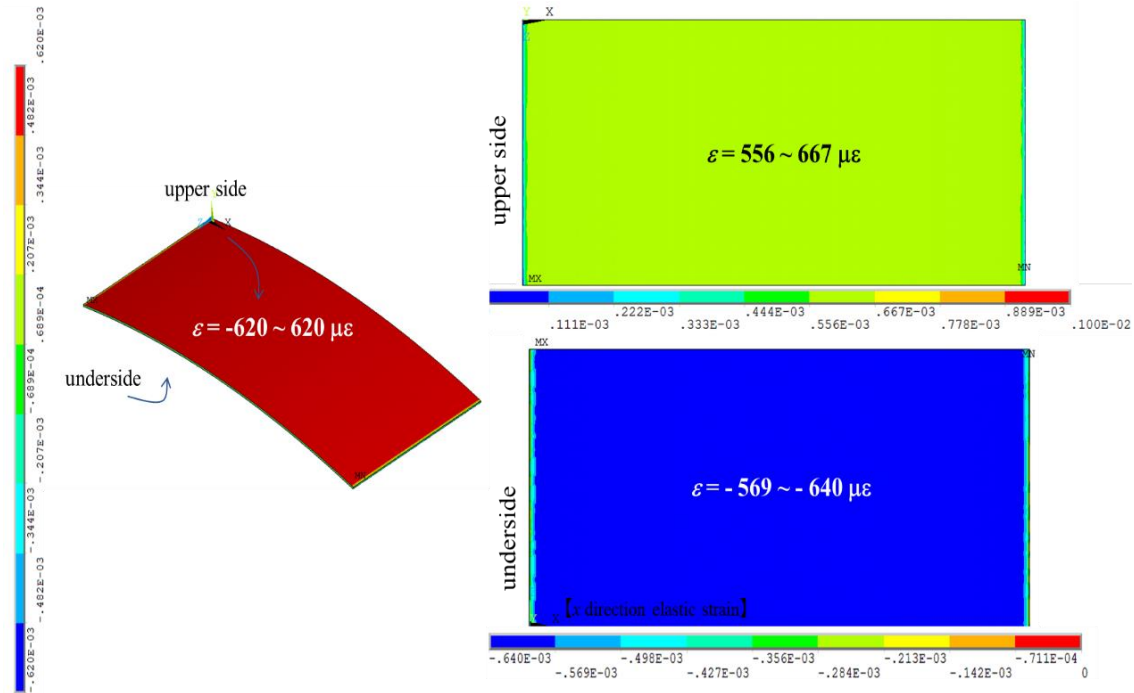


Figure 2.3 Strain distribution on the test piece before reduction of thickness

Figure 2.4 shows the strain distribution simulated by FEM at the back side of the test piece and the upper side when the corroded happen. Figure 2.4 represents the strain distribution at upper side and back side of the test piece with reduction in thickness in the x direction, and Figure 2.5 represents the strain distribution at the backside and back side of the test piece with the thickness in the z direction. Without a reduction in thickness ($h = 0.5 \text{ mm}$) in the x direction, the strain indicated by the blue area was $-579 \mu\epsilon$, which was calculated from an average of five points. The same values were

obtained for the FEM simulation and the analytical model, which predicted a value of $-581 \mu\epsilon$. In contrast, in the y direction, the strain in the was $0 \mu\epsilon$. This behavior indicates that the moment was applied in the longitudinal strain in the x direction of the test piece. The strain distribution in the region of the test piece with decreased thickness for $\Delta h = 0.4 \text{ mm}$ and $\Delta h = 0.23 \text{ mm}$ in the x direction had the same absolute value as the strain calculated using Equation (2.3) in the analytical model. Based on FEM results, a decreased in thickness did not affect the strain distribution in the y direction. The absolute value of the strain was $0 \mu\epsilon$.

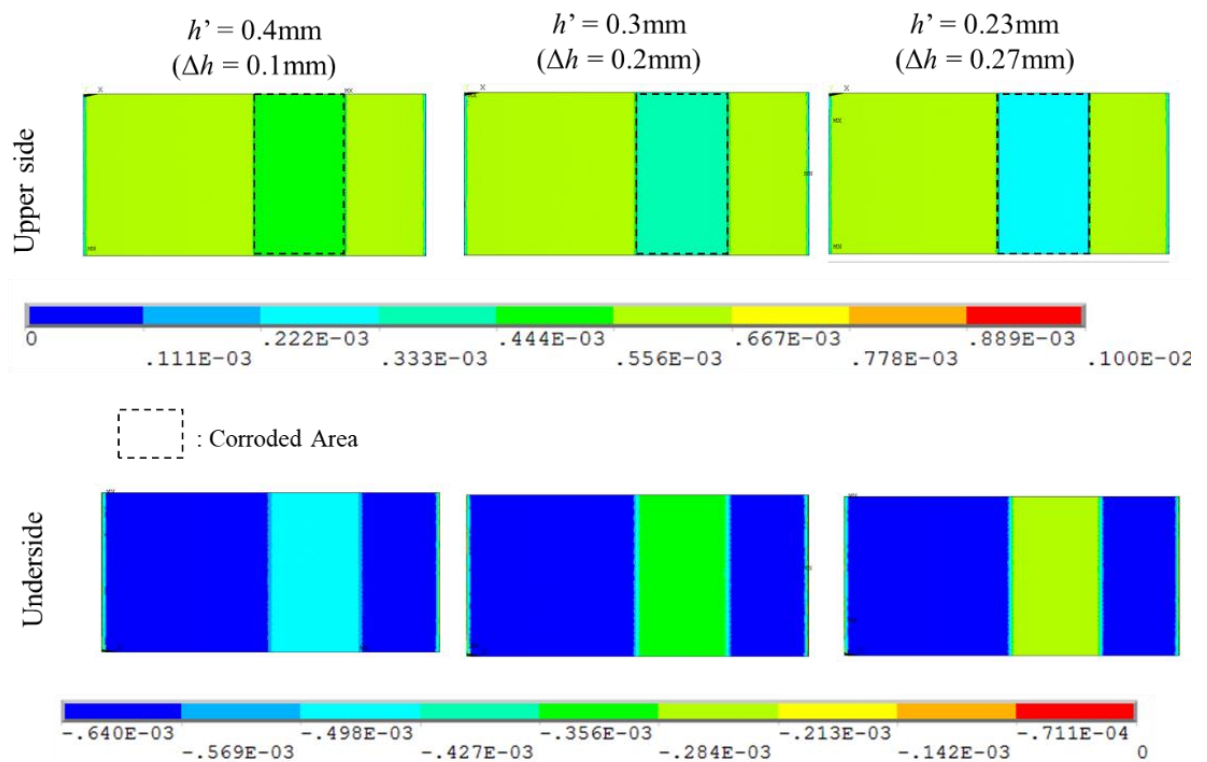
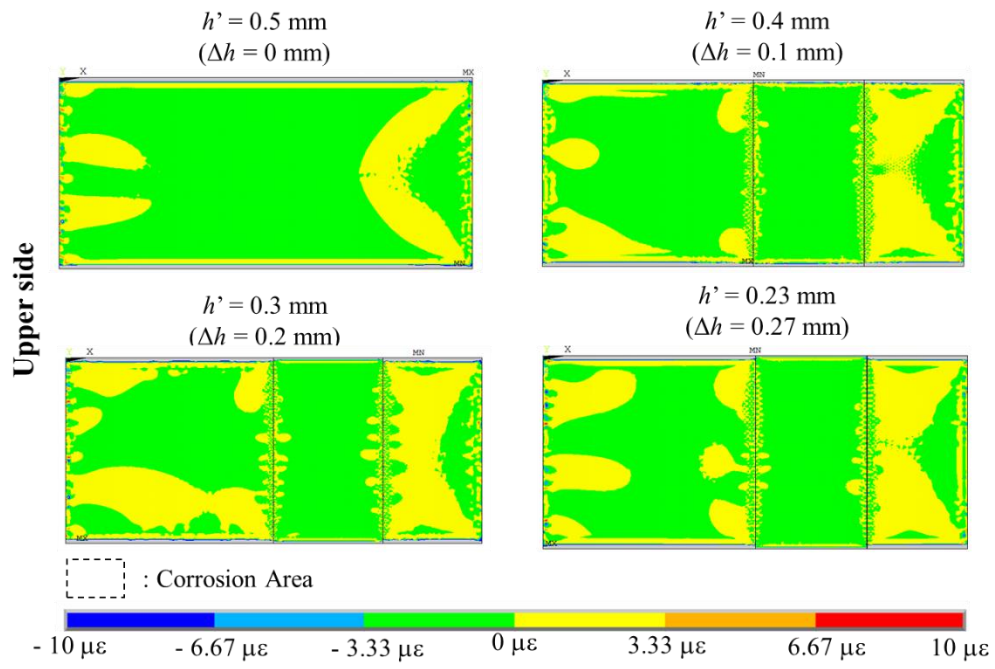
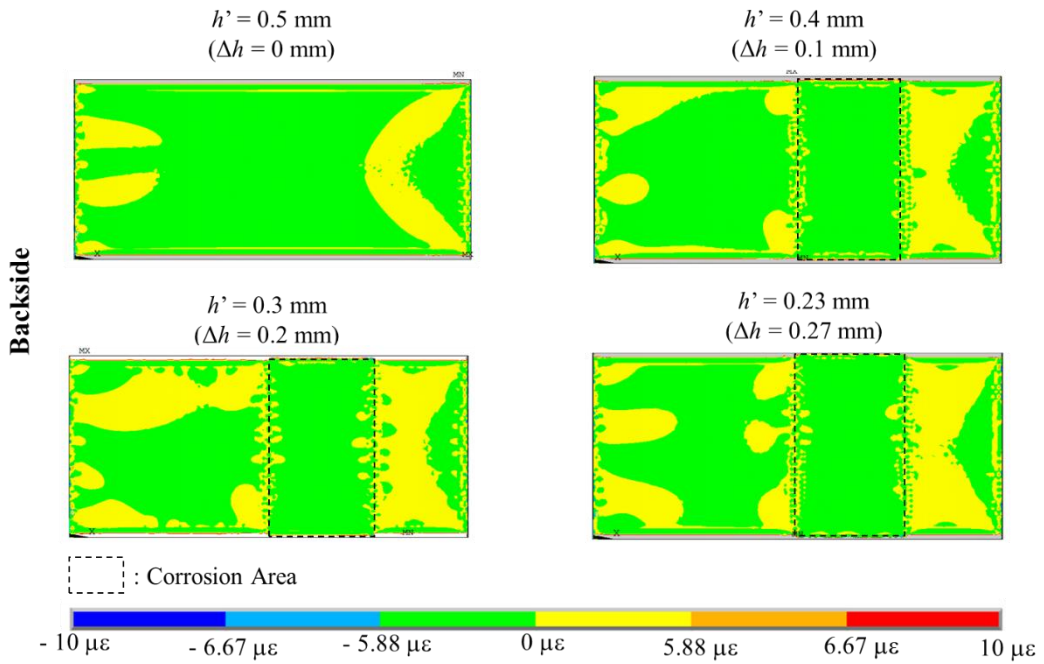


Figure 2.4 Strain distribution after corroded on (a) the upper side and (b) under back side of the test piece with a reduction in thickness in the x direction, simulated by FEM



(a)



(b)

Figure 2.5 Strain distribution after corroded on (a) the upper side and (b) under side of the test piece with a reduction in thickness in the z direction, simulated by FEM

The relationship between the longitudinal strain and the thickness reduction of the test piece is shown in Figure 2.6. Figure 2.6(a) shows the relationship between the strain and the thickness reduction of the test piece in the x direction. Figure 2.6(b) shows the relationship between $\Delta\varepsilon$ and Δh . The strain shows a linear relationship with the thickness reduction of the test piece. As shown in Figure 2.6, a good correlation was achieved between the analytical results determined using the mechanical of material parameters and the finite element simulation and indicated that the principle of atmospheric corrosion sensor is reasonable. Table 2.1 shows the FEM results in the x direction under the corroded area, where the active FBG was set up, and the strain in the x and y directions under the uncorroded area, where the dummy FBG was set up. When temperature changes were applied in FEM analysis with $\Delta T = 10$ K, the strain differed by $117 \mu\varepsilon$ in both the x and y direction. This indicates that the thermal expansion of the test piece was $11.7 \mu\varepsilon/\text{K}$. The results indicate that the dummy position is not affected by a thickness reduction of the test piece. Figure 2.7 shows a magnification of the strain distribution for the test piece with a thickness reduction of 0.27 mm. The scale of the uncorroded area was linear, but the corroded area had a scale that differed by $350 \mu\varepsilon$. The results indicated that the strain distribution was not the same in the x direction in the uncorroded area: a difference of approximately $12 \mu\varepsilon$ was observed. To avoid the effect of the thickness reduction on the strain, we set up the dummy FBG in the y direction with the same strain value. Thus, we defined the configuration of the active and dummy FBGs on the test piece as shown in Figure 2.7.

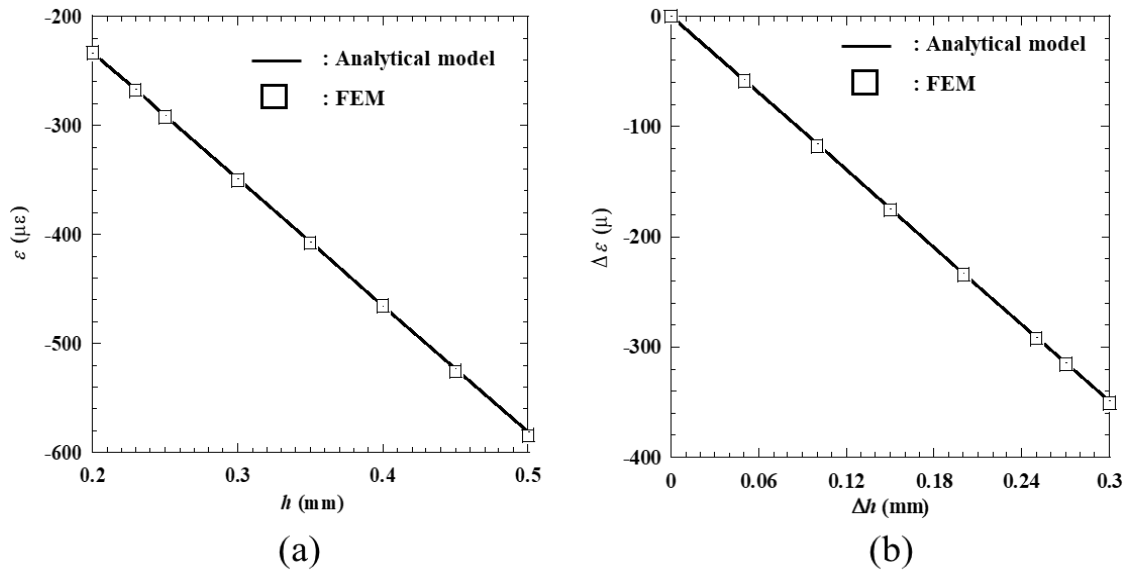


Figure 2.6 The validation of the analytical model and FEA in the x direction (a) between strain ε in $\mu\epsilon$ and h in mm and (b) between $\Delta\varepsilon$ in μ and Δh in mm.

Table 2.1 The calculated strain obtained using FEM

Thickness h [mm]	Strain ($\mu\epsilon$)								
	Corroded Area			Uncorroded Area					
	x direction		When ΔT is 10 K	x direction			y direction		
at 300 K	at 310 K	at 300 K		at 310 K	When ΔT is 10 K	at 300 K	at 310 K	When ΔT is 10 K	
0.5	-584	-467							
0.45	-525	-408							
0.4	-466	-349							
0.35	-408	-291							
0.3	-350	-233	117	-584	-467	117	0	117	117
0.25	-292	-175							
0.23	-268	-151							
0.2	-233	-116							

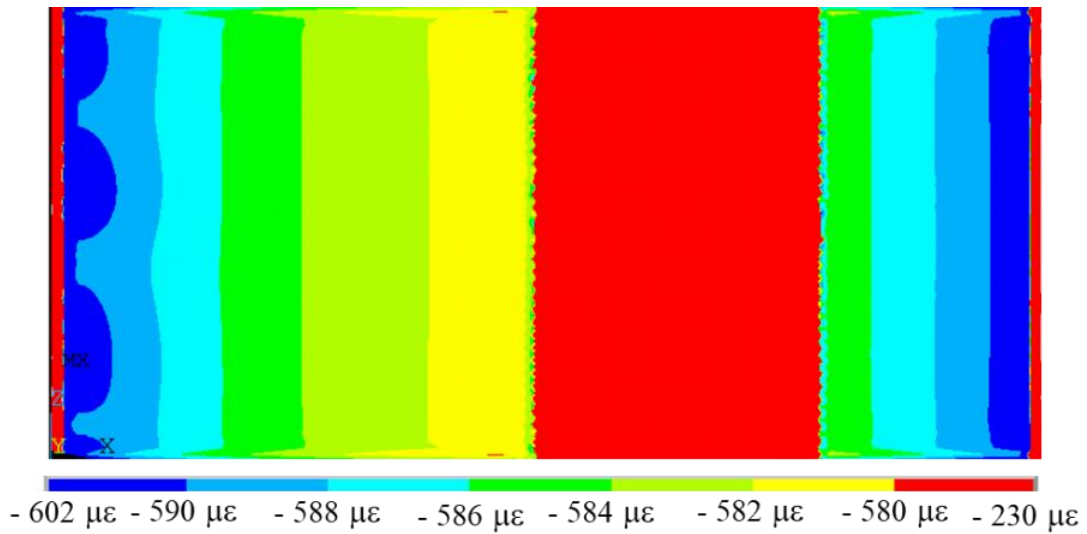


Figure 2.7 Magnification of the strain distribution on the back side of the test piece with a reduction of thickness of 0.27 mm simulated by FEM in the x direction.

2.4. Design of Test Piece and Apparatus

The test piece that used for ACSSM was made from low-carbon steel with 95 mm in length, 45 mm in width, 0.5 mm in thickness. Before setting it in the apparatus, the test piece was heat-treated at 450 °C for 1 hour for removing the residual stress. A corroded area was arranged in the middle of the test piece with 30 mm in length and 45 mm in width as shown in Figure 2.8. The corroded area has no plastic coating at the surface and the remaining was coated with plastic to prevent the corrosion. At the back side corroded area, the sensors were set up and monitored the thickness of the test piece in relationship with the strain. The test piece becomes thinner as a result of corrosion. To determine the radius curvature of apparatus (ρ), Equation (2.3) can be combined with Hooke's law, yielding the equation:

$$\rho = \frac{E h}{2\sigma_y} \dots\dots\dots (2.6)$$

where E is a Young's modulus of 210 GPa, h is thickness of the test piece and σ_y is using a yield stress of the test piece 240 MPa. Using the Equation (2.6), ρ was obtained in elastic deformation the range was 219 mm and $\rho = 430$ mm used to prevent local plastic deformation of the test piece, ρ should be twice larger. According to Equation (2.4), $\Delta h = 0.86 \times \Delta \varepsilon$. The unit of $\Delta \varepsilon$ is $\mu\varepsilon$, the unit of Δh are μm , and the unit of the coefficient 0.86 is m/ε .

The apparatus consists of a base and cover made of polyvinyl chloride. Figure 2.9 and Figure 2.10 show the dimension of the base and cover of the apparatus from the side and top view. Strain gauges, that was in contact with the back of the test piece installed in the middle of the apparatus.

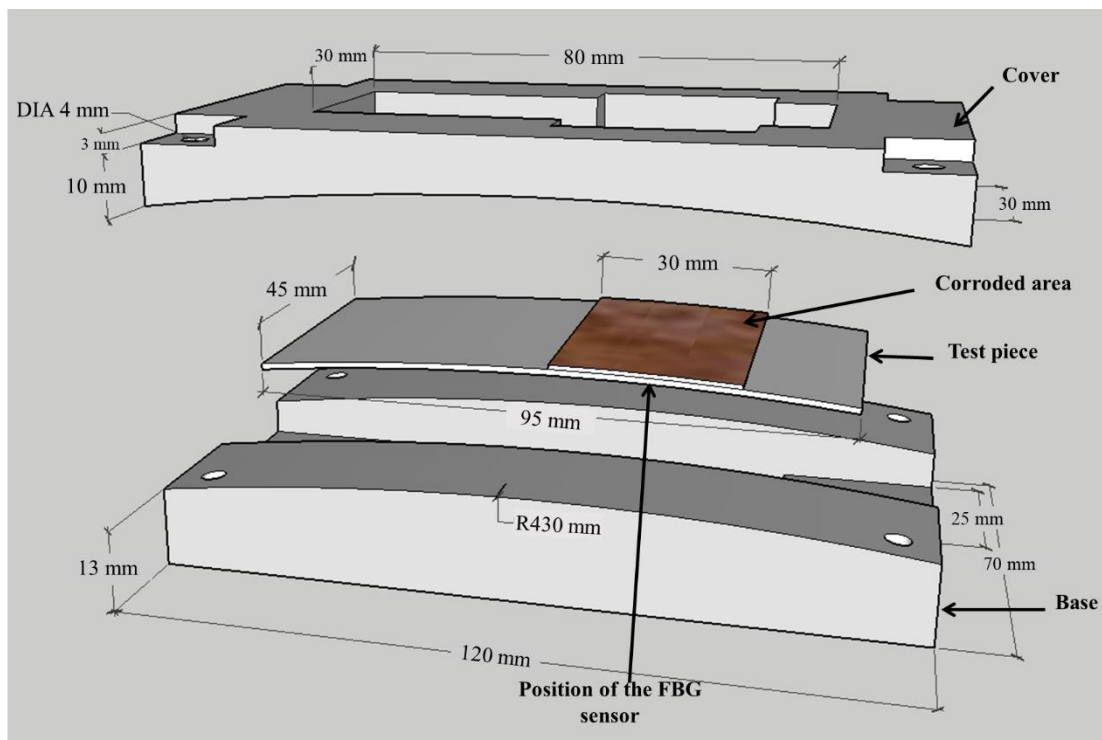
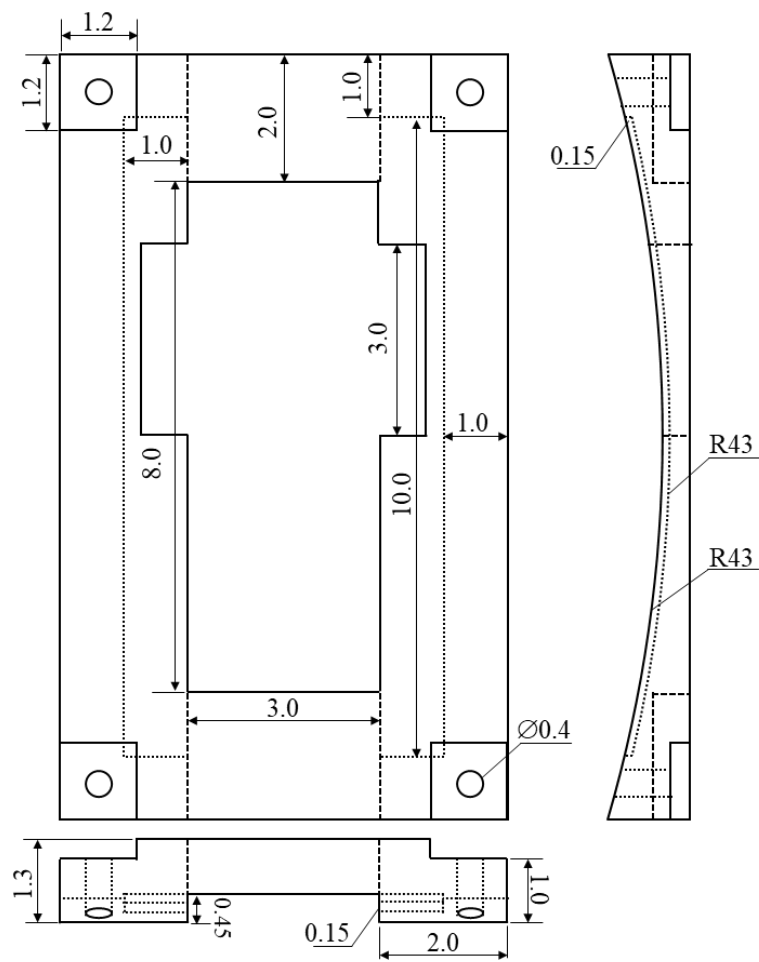


Figure 2.8 Test piece and apparatus for ACSSM sensor.

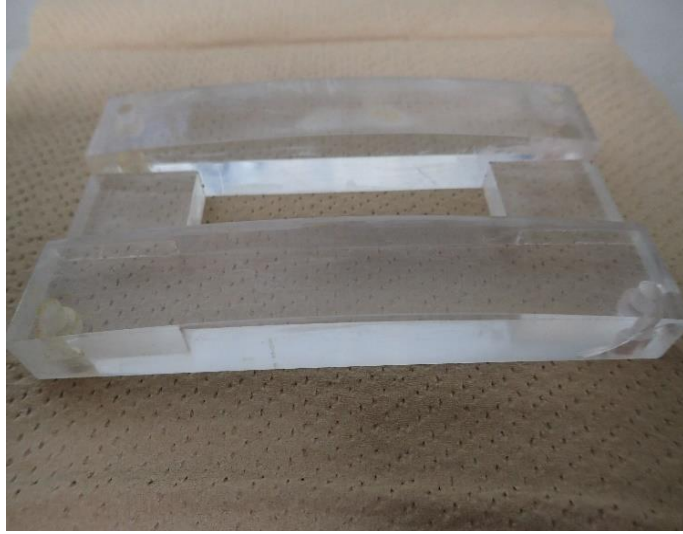


(a)

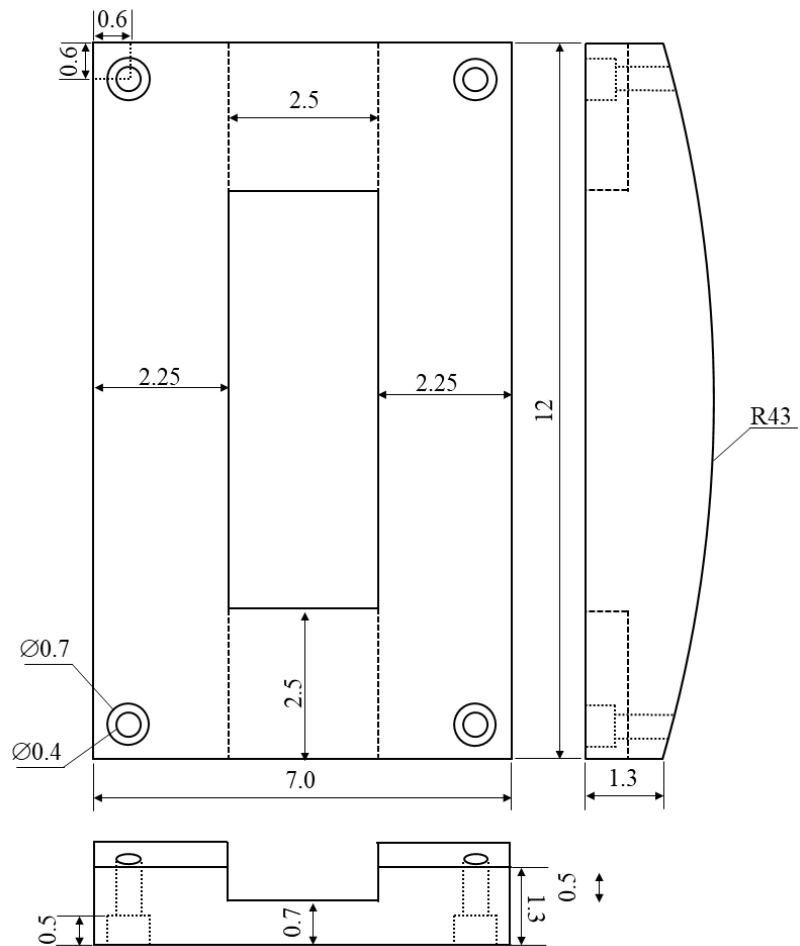


(b)

Figure 2.9 (a) The picture of cover (b) Dimension of the cover of the apparatus for ACSSM. Unit is in cm.



(a)



(b)

Figure 2.10 (a) The picture of base (b) Dimension of the base of the apparatus for ACSSM. Unit is in cm.

2.5. Concept of Active Dummy Circuit Method

The amplifier circuit fabricated by the active dummy method for atmospheric corrosion monitoring consists of bridge circuits with strain gauge sensors connected to the test piece, pre-amplifier circuits based on an instrumentation stage operational amplifier with a circuit identical to that used in the active dummy method, and a differential circuit that differs from the active dummy circuit. The design concept of the amplifier circuit used in the active dummy method to monitor atmospheric corrosion is illustrated in Figure 2.11. $\varepsilon_{m,t,o}$ is the strain with input from the signal and environmental factor (-). ε_m is the strain from the thinning of the test piece due to corrosion stress. $\varepsilon_{t,o}$ is the strain due to environmental effects, such as temperature and humidity. The active circuit has not only ε_m but also $\varepsilon_{t,o}$ as inputs, whereas, in the case of the dummy circuit, the only input is $\varepsilon_{t,o}$. The differential circuit subtracts the output from the active circuit from the output from the dummy circuit. Since the dummy circuit compensates for the effects of environmental or atmospheric conditions on the active circuit, an accurate value is obtained for ε_m .

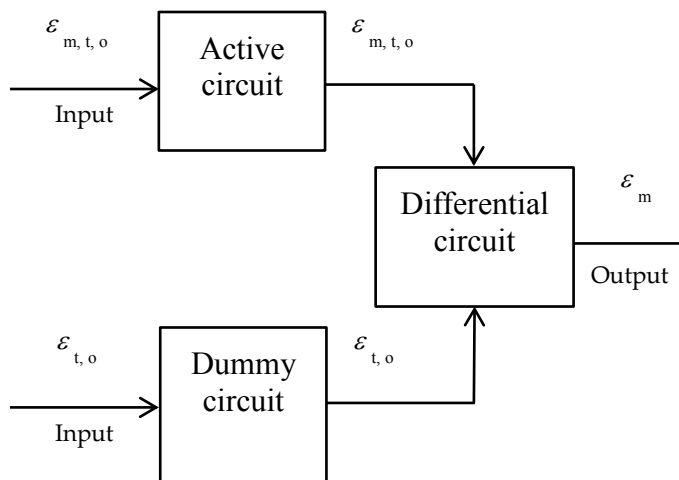


Figure 2.11 Design concept of active dummy method.

2.6. Design of Amplifier Circuit

2.6.1. Strain Measurement Circuit

ACSSM using strain gauge sensors which attached at the test piece and connected to the amplifier circuit. The strain measurement circuit consist of wheat stone bridge and instrumentation stage amplifier circuit. The wheat stone bridge is appropriate for small change measurement of a resistance in a strain gauge. The changing of strain gauge resistance is applied to determine the strain. The relationship between the strain ε and the change of resistance in a strain gauge is followed the equation:

$$\varepsilon = \frac{\Delta L}{L_o} = \frac{\Delta R}{k R_o} \quad \dots\dots\dots (2.7)$$

ΔL is change in length of gauge element (m), L is original length of gauge element (m), ΔR is change in resistance (Ω), R is initial resistance (Ω) and k is gauge factor, is a characteristic of the strain gauge. The exact value is specified on each strain gauge package. The wheat stone bridge that built in design of amplifier circuit using four strain gauges as shown in Figure 2.12 below:

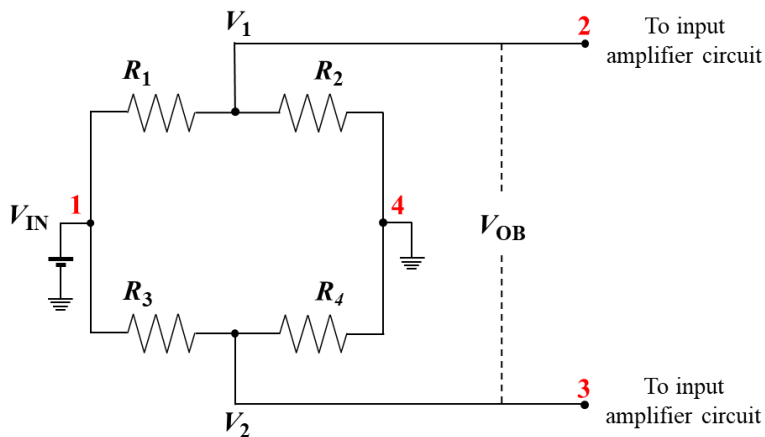


Figure 2.12 Wheat stone bridge circuit with four strain gauges

In wheat stone bridge, commonly the equation

$$\frac{V_{OB}}{V_{IN}} = \frac{R_1}{R_1 + R_3} - \frac{R_2}{R_2 + R_4} \dots\dots\dots (2.8)$$

V_{IN} is input voltage of bridge circuit (V), V_{OB} is output of bridge voltage (V), $R_1 = R_2 = R_3 = R_4$ are resistance of strain gauges (Ω).

In case of balanced bridge, $V_{OB} = 0$, if:

$$R_1 = R_2 = R_3 = R_4 \quad \text{or} \quad R_1:R_3 = R_2:R_4 \quad \text{or} \quad R_1R_4 = R_2R_3 \dots\dots\dots (2.9)$$

When the resistor R_1 to R_4 vary due to the environmental factor or proposed signal, the output voltage V_{OB} will appear. The additional assumption that the resistance variation ΔR_i is much smaller than the resistance R_i itself, second order factor can be ignored.

Now, we have the following relationship:

$$\frac{V_{OB}}{V_{IN}} = \frac{R_1 + \Delta R_1}{(R_1 + \Delta R_1) + (R_3 + \Delta R_3)} - \frac{(R_2 + \Delta R_2)}{(R_2 + \Delta R_2) + (R_4 + \Delta R_4)}$$

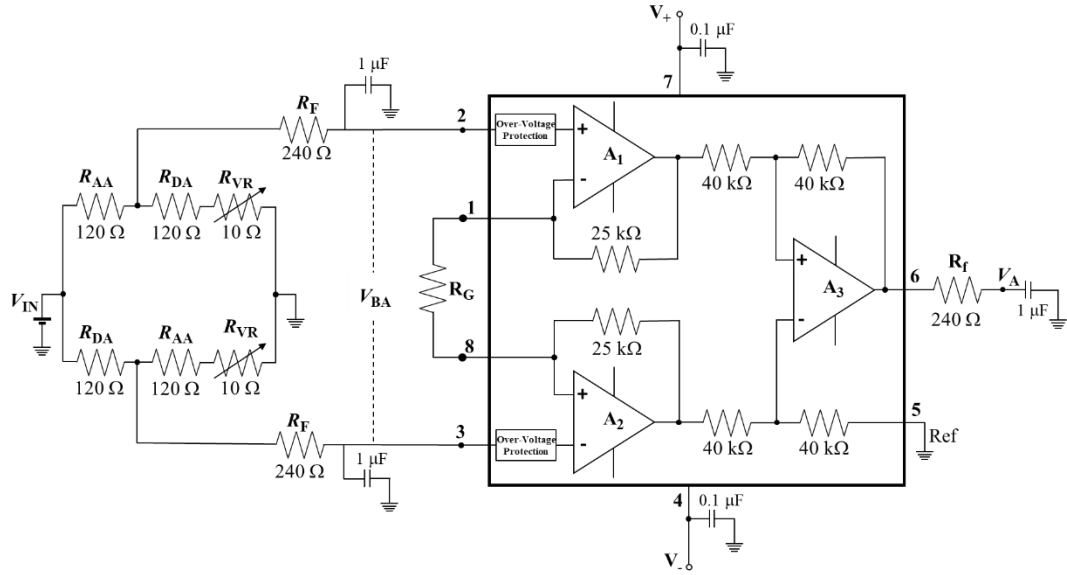
$$\frac{V_{OB}}{V_{IN}} = \frac{1}{4} \left(\frac{\Delta R_1}{R_1} - \frac{\Delta R_2}{R_2} + \frac{\Delta R_4}{R_4} - \frac{\Delta R_3}{R_3} \right) \dots\dots\dots (2.10)$$

From Equation (2.7) and (2.10), we obtained:

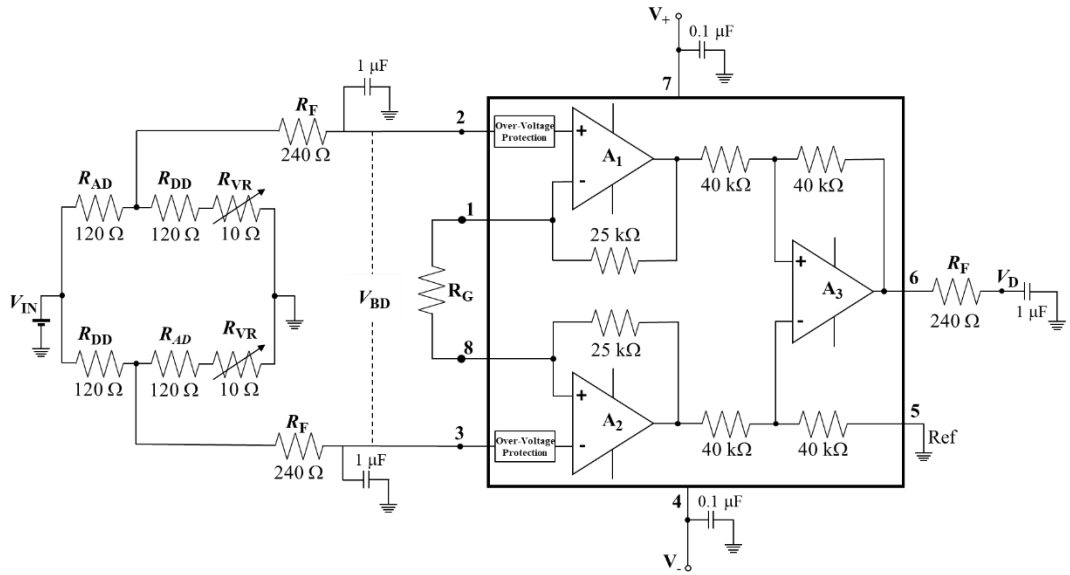
$$\frac{V_{OB}}{V_{IN}} = \frac{k}{4} (\varepsilon_1 - \varepsilon_2 + \varepsilon_4 - \varepsilon_3) \dots\dots\dots (2.11)$$

ε_1 , ε_2 , ε_3 and ε_4 are strain in each gauge. V_{OB} is the output voltage of the bridge circuit which has very small voltage. To read the very small signal, we need the amplification operational amplifier base on the instrumentation stage.

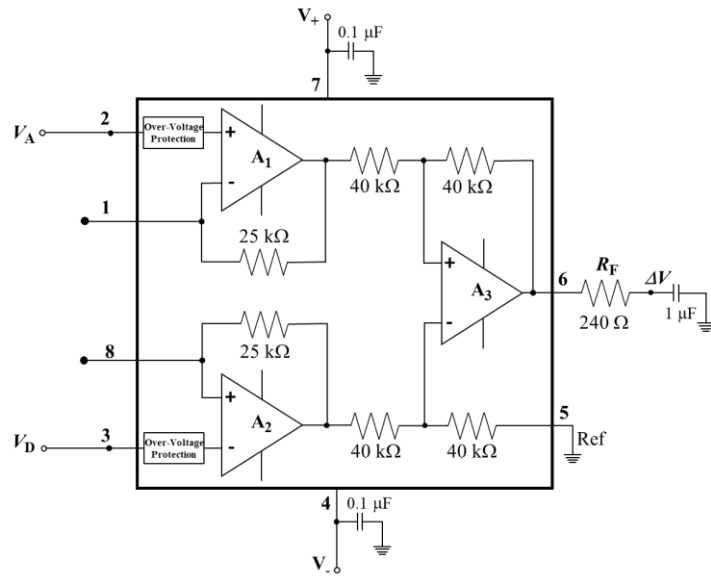
The design of amplifier circuit using active dummy method that used in ACSSM comprises of active circuit, dummy circuit and differential circuit as shown in Figure 2.13.



(a)



(b)

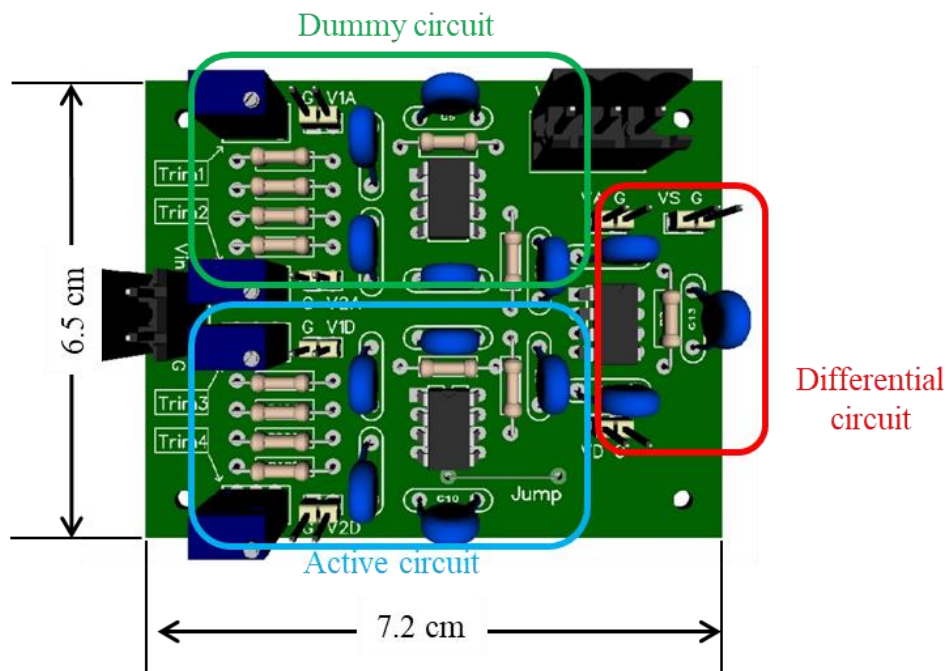


(c)

Figure 2.13 Electronic design of the strain measurement circuit by active dummy method (a) active circuit (b) dummy circuit and (c) differential circuit

The strain measurement circuit that used in the active dummy method, with R_G is gain resistance to determine the signal amplification, was designed to measure very small strains of Tokyo Sokki FLA-5-11 strain gauges where it was placed in a bridge circuit. R_{AA} , R_{DA} , R_{AD} , and R_{DD} have a same resistance of 120Ω . R_{VR} is 10Ω variable resistor that used for making balance in the starting point of experiment. Using a voltage input (V_{IN}) of 3 V to adjust the current through the strain gauges, the output voltages of (i) the active bridge circuit, V_{BA} ; (ii) the dummy bridge circuit, V_{BD} ; (iii) the active circuit, V_A ; (iv) the dummy circuit, V_D ; and (v) the differential circuit, ΔV , should all be zero under balanced conditions. When a variation in the strain gauge resistance appeared in the signal, V_{BA} appeared and, when amplified, became V_A , in addition to ΔV also appearing. The input for the operational V_+ and V_- is 10 V and became the maximum voltage of the circuit. To reduce the noise, capacitors were used

as a filter in the input area, as well as a filter consisting of capacitors and resistors in the output area. INA128 op-amplifiers (Burr-Brown Corp.), which are largely unaffected by temperature variations were used. The other components had low coefficients of thermal expansion and low tolerance. Figure 2.14 show computer-aided drawing and the photograph of strain measurement circuit with an active dummy method using strain gauges.



(a)

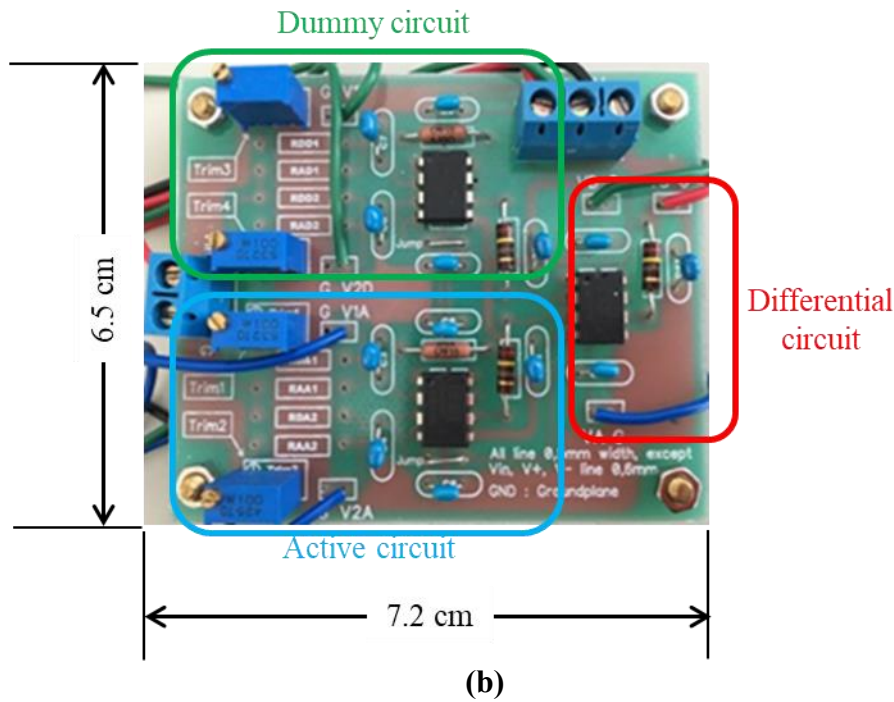


Figure 2.14 (a) CAD of electronic circuit and (b) photograph of the strain measurement circuit with an active dummy method.

2.6.2. Temperature Drift Compensation

The design of ACSSM considered the environmental factor such as temperature, humidity, hydrostatic pressure, radiation and the other factor that affected to the strain measurement in compensation system. The simple principle of compensation can be illustrated by temperature effect as temperature drift compensation.

Karl Hoffmann revealed in the bridge circuit theory, if strain gauges have similar signs, the changes of absolute values of neighboring strain gauges are subtracted. They are added if they have different signs. This condition can be used for some combination or compensation methods. If we arrange the position of strain gauge on the test piece in such a way that interferences will influence neighboring strain gauge in the same way, they compensate one another. We installed the strain gauge as mechanical stress

(ε_M) and the strain gauge as temperature drift compensation (ε_T). In this design, strain gauges as mechanical stress is active gauges and the strain gauges as temperature drift gauges is dummy gauges. If the temperature variation occurs during the mechanical stress, then there is a composite strain signal. If one component is from the mechanical stress and the other component is from temperature drift. The Equation (2.12) can be expressed:

$$\frac{\Delta R}{R_o} = k(\varepsilon_M + \varepsilon_T) \dots\dots\dots (2.12)$$

In case of four strain gauges that attached to the test piece, they connect to the bridge circuit fully, and applied the temperature drift. The following situation is shown in Table 2.2.

Table 2.2 Sign for strain gauge component

Strain Gauge No.	ε_M	ε_T
1	+	+
2	-	+
3	+	+
4	-	+

The Equation (2.13) can be expressed by:

$$\frac{V_{OB}}{V_{IN}} = \frac{k}{4} [(\varepsilon_M + \varepsilon_T)_1 - (-\varepsilon_M + \varepsilon_T)_2 + (\varepsilon_M + \varepsilon_T)_4 - (-\varepsilon_M + \varepsilon_T)_3]$$

$$\frac{V_{OB}}{V_{IN}} = \frac{k}{4} [4\varepsilon_M] = k\varepsilon_M \dots\dots\dots (2.13)$$

We can see that all thermal component in the total strain ε_T has the same sign for all strain gauges, provided they are all subjected to the same change in temperature.

The Equation (2.13) shows the effect of the temperature has been compensated.

2.6.3. Voltage vs Strain Test

Converting the output voltage of the strain measurement circuit to the strain value, we conduct the experiment voltage vs strain test. This experiment used the data logger Graphtec GL7000 to monitor the voltage from the strain measurement circuit and the temperature of the measurement environment, and a tensile machine to apply the various force to the active strain gauges.

To induce a strain on test piece that attached the active strain gauges, the edges of the test piece was fixed, and the tensile machine apply force to the test piece. The center of the test piece exhibited the active strain due to the deformation. Within the elastic strain region of the test piece, the relationship between strain and force was linear. Meanwhile, the dummy strain did not detect the variations in strain, only the behavior of the environment. The experiment set up can be shown in Figure 2.15.

The output voltages of the active circuit, dummy circuit and amplifier circuit were measured by taking data at a rate of 1 sample/second. The force from the tensile machine and the voltage (V) from the amplifier circuit were monitored. Figure 2.16 plots the results of the experiment as the master curve for the strain versus voltage. Using the different value of R_G (1 to 5 Ω), the graph shows that the amplifier circuit had a linear relationship with the strain.

The present amplifier circuit, successfully designed by the active dummy method for the ACSSM sensor, has a high sensitivity. This master curve is used in the following sections to convert the output voltage of the amplifier circuit to strain.

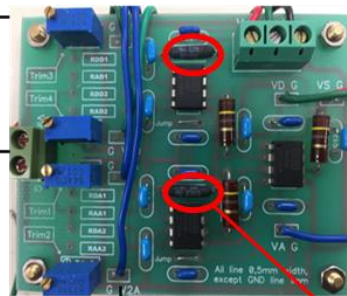
DC Power Supply



Graphtec/Oscilloscope



Amplifier Circuit



Tensilon Machine



- $V_{IN} = 3.0$ Volt
- $V_{+} = 10$ Volt
- $V_{-} = 10$ Volt
- $R_{AG} = 120$ Ohm
- $R_{DG} = 120$ Ohm
- $R_G = 1.1, 1.2, 3.1, 4$ and 5Ω

Figure 2.15 The experiment set up for voltage vs strain test.

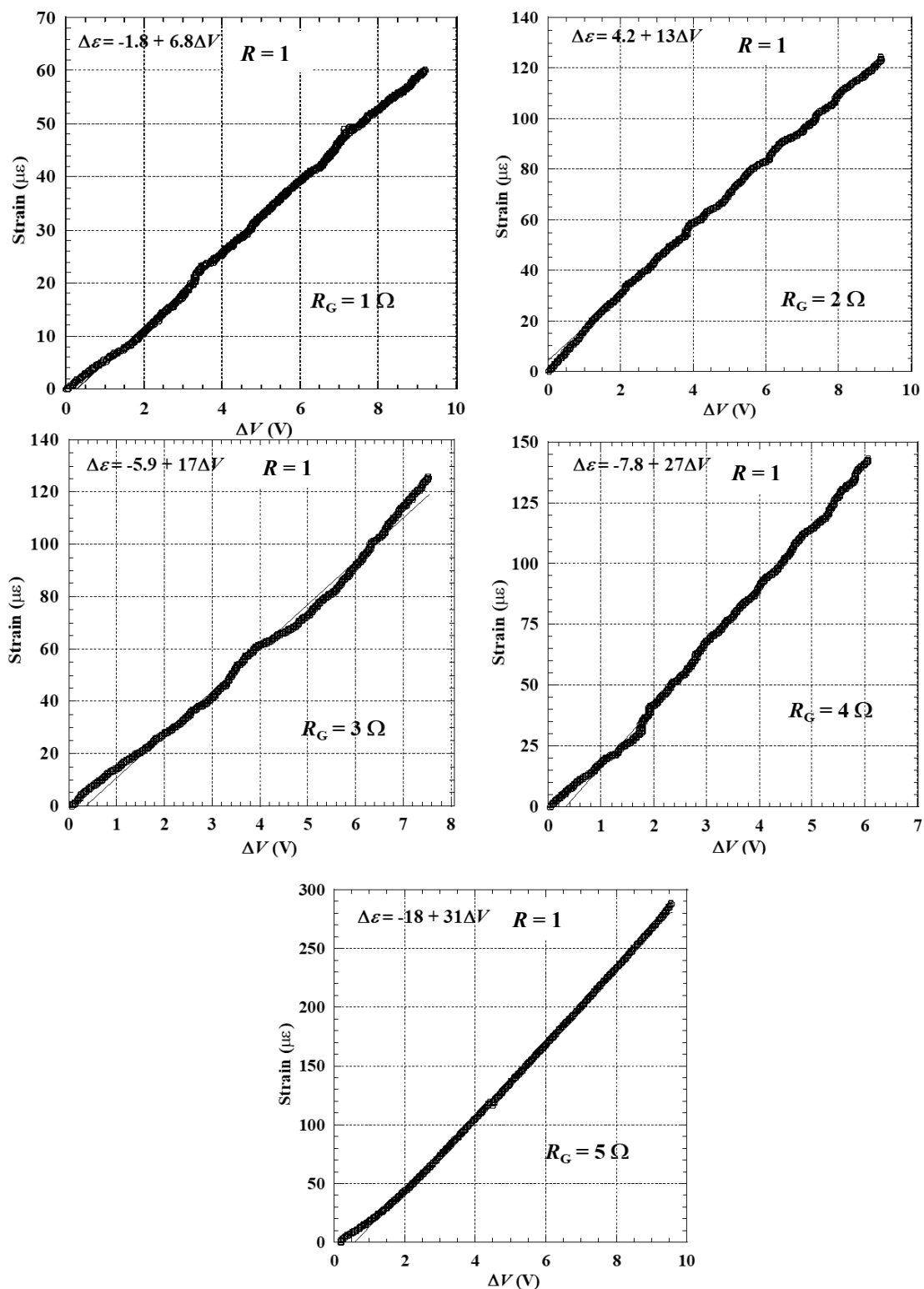


Figure 2.16 The result of experiment voltage vs strain with different R_G

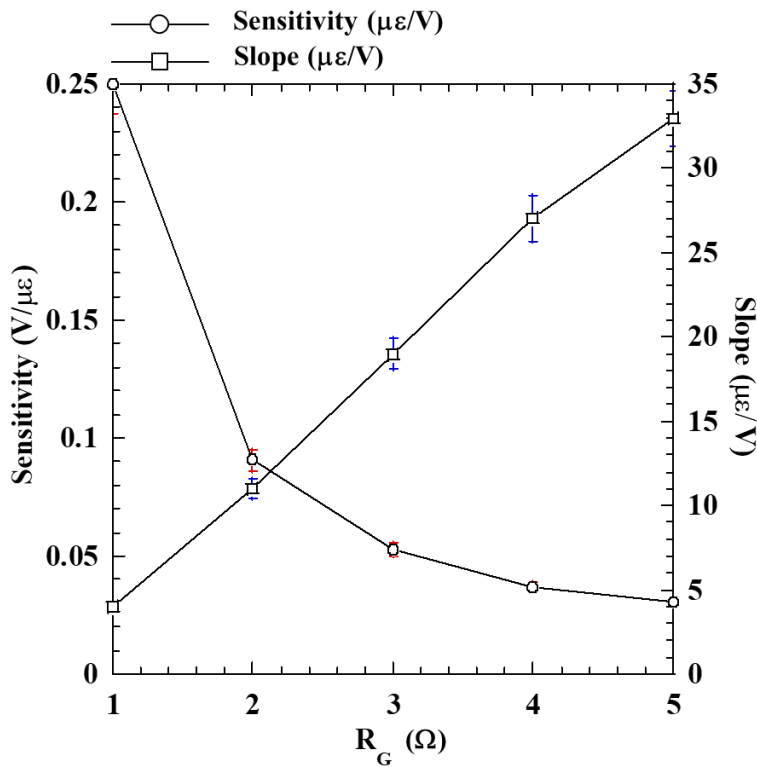


Figure 2.17 The sensitivity of amplifier circuit with different R_G

2.6.4. Thermography Test

Thermo FLEX F50 series is a completely "New-Style" infrared thermal imaging camera can be easily rotated and separated camera-head and controller. Using the infrared thermograph "Thermo FLEX F50 series" from Nippon Avionic Japan, the temperature of test piece and amplifier circuit was conduct. The purpose of this test is for indicating the component of the circuit that has a maximum temperature. Figure 2.18 is visual of the temperature distribution of the circuit and the circuit itself. The component which has higher temperature is operational amplifier. The operational

amplifier for the active circuit has a higher temperature than the dummy and differential circuit. That is because the active has a higher voltage than the other circuit.

Figure 2.19 show the distribution of temperature on the test piece. The corroded area with the corrosion product has a higher temperature than uncorroded area.

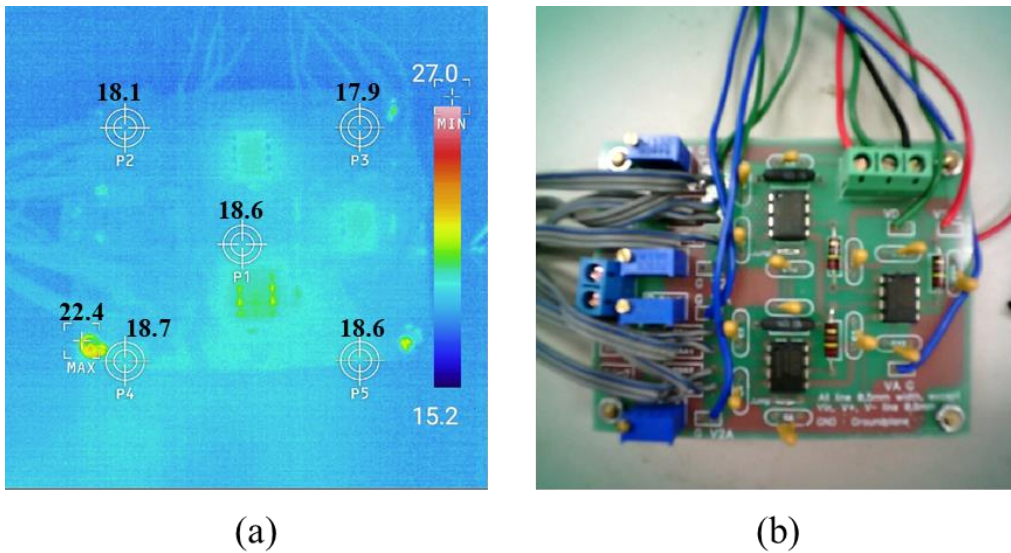


Figure 2.18 (a) Thermograph result of circuit (b) photograph of amplifier circuit that took in the same time

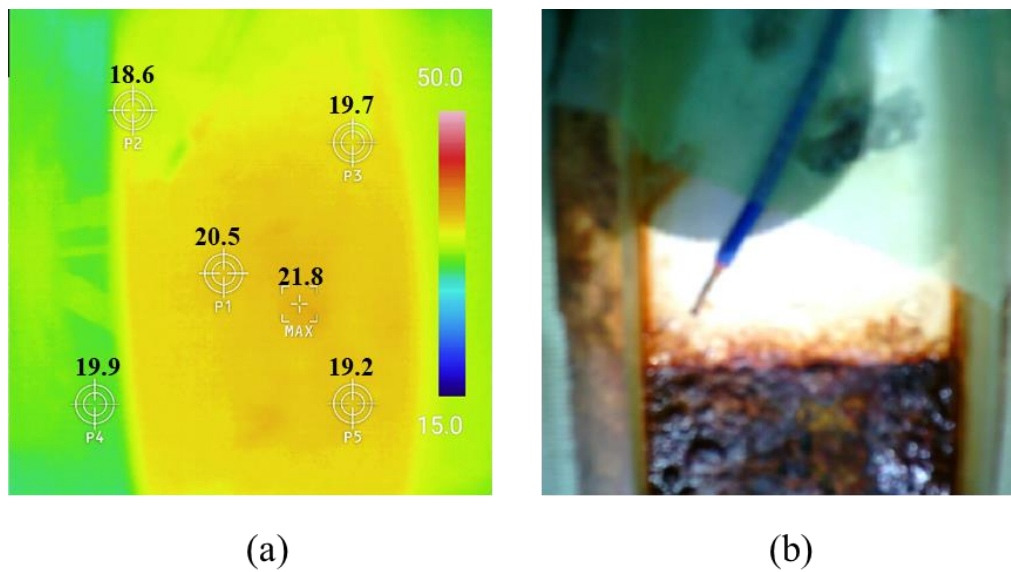


Figure 2.19 (a) Thermograph result of test piece (b) photograph of test piece that took in the same time

2.7. FBG Sensor Measurement

2.7.1. Principle of FBG Sensor Measurement

The basic principle of the FBG strain sensor is based on the measurement of the shift in the peak reflected wavelength as shown in Figure 2.20. The shift in the peak reflected wavelength caused by the application of strain, temperature changes and other external influences. The peak reflected Bragg wavelength (λ_B) in unstrained conditions is given by:

$$\lambda_B = 2 n \Lambda \quad \dots\dots\dots (2.14)$$

where n is the refractive index and Λ is the spacing between the gratings. When there is force from external influences, both of n and Λ are changed as shown in Figure 2.21, λ_B shifted to λ_B' according to the Equation (2.14):

$$\lambda_B' = 2 n' \Lambda' \quad \dots\dots\dots (2.15)$$

where Λ' is spacing between the grating after getting force the external influences and n' is refractive index after getting force the external influences. The change of λ_B can be expressed by:

$$\Delta\lambda_B = \lambda_B' - \lambda_B \quad \dots\dots\dots (2.16)$$

The changes in Bragg wavelength temperature and strain can be determined by using Equation below:

$$\Delta\lambda_B = [(1 - p_e)\varepsilon + \alpha_n\Delta T]\lambda_B \quad \dots\dots\dots (2.17)$$

where p_e is the strain optic coefficient, ε is strain, α_n is coefficient thermal expansion and ΔT is the change in temperature. This means that Bragg wavelength is changed by increased of strain or temperature.

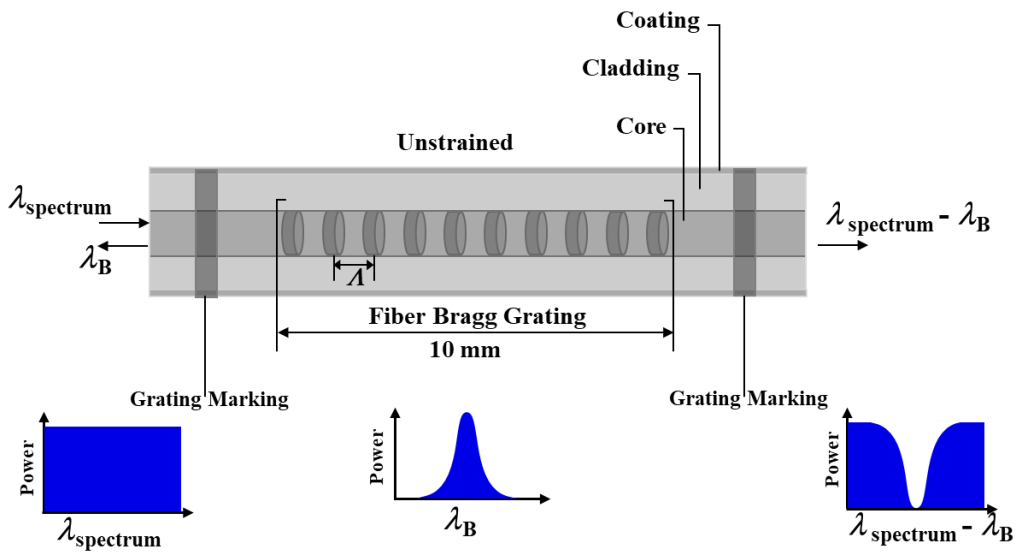


Figure 2.20 The principle of FBG sensor operation in unstrained condition

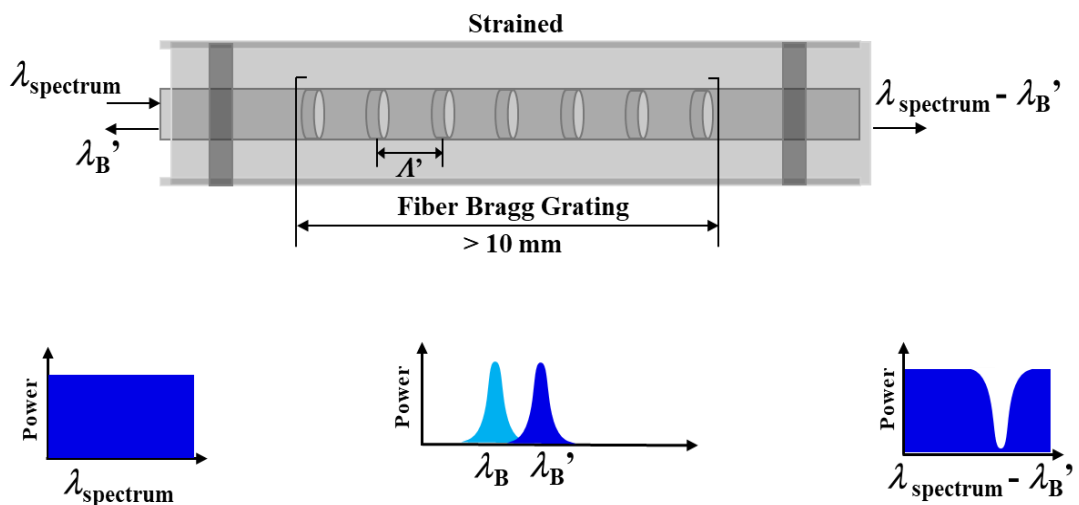


Figure 2.21 The principle of FBG sensor operation in strained condition

2.7.2. Temperature and Strain Sensitivity

Equation (2.17) can be expressed by:

$$\frac{\Delta\lambda_B}{\lambda_B} = k \cdot \varepsilon + \alpha_n \Delta T \quad \dots\dots\dots (2.18)$$

Where $k = 1 - p_e$, is gauge factor ($k = 0.78$ for fiber). In Equation (2.19), the first expression ($k \cdot \varepsilon$) is the strain caused by mechanical strain (ε_m) and temperature (ε_T). In ACSSM, it is a strain from active FBG sensor. The second part is the change of the refraction index and spacing of grating caused by temperature. It is a strain from dummy FBG sensor.

Therefore,

$$\varepsilon = \varepsilon_m + \varepsilon_T \quad \dots\dots\dots (2.19)$$

$$\varepsilon_T = \alpha_{tp} \times \Delta T \quad \dots\dots\dots (2.20)$$

α_{tp} is expansion coefficient of the test piece. Inserting the Equation (2.19) and (2.20) to Equation (2.18) which exhibits the behavior of FBG caused by the both of strain and temperature can be express below:

$$\frac{\Delta\lambda_B}{\lambda_B} = k \cdot (\varepsilon_m + \varepsilon_T) + \Delta T$$

$$\frac{\Delta\lambda_B}{\lambda_B} = k \cdot (\varepsilon_m + \alpha_{TP}\Delta T) + \alpha_n\Delta T$$

$$\frac{\Delta\lambda_B}{\lambda_B} = k \cdot \varepsilon_m + k \cdot \alpha_{TP}\Delta T + \alpha_n\Delta T$$

$$\frac{\Delta\lambda_B}{\lambda_B} = k \cdot \varepsilon_m + (k \cdot \alpha_{TP} + \alpha_n)\Delta T \quad \dots\dots\dots (2.20)$$

In this case, the test piece material is steel which has $\alpha_{tp} = 11, \dots, 13 \cdot 10^{-6}/K$ and $\alpha_n = 5, \dots, 8 \cdot 10^{-6}/K$. From the Equation (2.20), we can determine the ε_m according to Equation below:

$$\varepsilon_m = \frac{\Delta\lambda_B}{k\lambda_B} - \left(\alpha_{TP} + \frac{\alpha_n}{k} \right) \Delta T \quad \dots\dots\dots (2.21)$$

Equation (2.21) is used for measuring the strain of FBG sensor. When the FBG is fixed to the test piece in the uncorroded area as dummy DBG sensor, it means without

the mechanical strain, it works for the temperature compensation FBG. It can be expressed by:

$$\frac{\Delta\lambda_B}{\lambda_B} = (k \cdot \alpha_{TP} + \alpha_n) \Delta T \quad \dots\dots\dots (2.22)$$

And

$$\Delta T = \frac{1}{k \cdot \alpha_{TP} + \alpha_n} \cdot \frac{\Delta\lambda_B}{\lambda_B} \quad \dots\dots\dots (2.23)$$

Equation (2.23) is used for measuring the temperature of FBG sensor.

2.7.3. Temperature Compensation

Temperature has a high impact in FBG strain measurement system. The accurate strain measurement result can be achieved with proper temperature compensation. Usually the normally temperature measuring FBG is used for measuring temperature. But, we also can use the strain FBG for compensation FBG sensor which named dummy FBG. In this research, we used both for calibration of the result. The simple calculation for this method is when the active FBG as mechanical strain has the same type with the dummy FBG and has the period and location in the same test piece. By subtracting the active signal of FBG with the dummy signal FBG, from the equation (2.19 and 2.20) can be determined the mechanical FBG signal:

$$\frac{\Delta\lambda_B}{\lambda_B} - \frac{\Delta\lambda_D}{\lambda_D} = k \cdot \varepsilon_m \quad \dots\dots\dots (2.24)$$

$$\varepsilon_m = \frac{1}{k} \cdot \left(\frac{\Delta\lambda_B}{\lambda_B} - \frac{\Delta\lambda_D}{\lambda_D} \right) \quad \dots\dots\dots (2.25)$$

where

$\Delta\lambda_B$ = wavelength change of active strain FBG

λ_B = initial wavelength of active strain FBG

$\Delta\lambda_D$ = wavelength change of dummy strain FBG

λ_D = initial wavelength of dummy strain FBG

Refer to ACSSM using strain gauges, Equation (2.25) is identical with $\Delta\varepsilon$ in micro strain.

2.8. Summary

The conclusions of the present study are as follows:

1. The fundamental measurement for atmospheric corrosion sensor based on strain measurement with an active dummy method was proposed.
2. The relation between strain and thickness reduction of test piece was obtained by mechanical concept of strain in bending.
3. The distribution of strain in test piece before and after bending, and with and without thickness reduction was simulated by FEM. The configuration of sensor on the test piece and the position of strain gauges and FBG sensors should be fixed based on the result of FEM simulation.
4. Design of apparatus and test piece based on the mechanical concept was proposed for the ACSSM. The design of strain measurement circuit for ACSSM with an active dummy method involved the concept of active dummy method using strain gauges, the bridge circuit concept, the instrumentation stage amplifier circuit for amplification of active and dummy signal and the differential circuit concept was developed with the output of the circuit is the voltage.
5. The experiment for Voltage vs Strain was conducted to convert the voltage to the strain using the R_G is 1 to 5 Ω . The principle of ACSSM with an active dummy method using strain gauges and FBG sensors was designed.

Chapter 3

ACSSM with an Active Dummy Method Using Strain Gauges by Galvanostatic Electrolysis

3.1. Introduction

Corrosion damages the steel that is used for many types of infrastructure. It causes major damage to steel that can lead to catastrophic structural failure. Based on that, corrosion detection on steel structures is necessary. Atmospheric corrosion monitoring is also important in predicting the corrosion damage of steel structures. The factors governing atmospheric corrosion are temperature, dew, precipitation, relative humidity, and nitrate, chloride and sulfate ions. At high temperatures, some electrolytes become highly reactive. Dew, precipitation and relative humidity also have a large effect on the corrosion process. Nitrate, chloride and sulfate ions can increase the corrosiveness of the environment. All these factors require further elaboration in order to clearly describe the phenomenon of atmospheric corrosion.

Several conventional methods for atmospheric corrosion monitoring, such as weight and thickness loss [Mansfel et al, 1976], polarization resistance [Mansfeld et

al, 1986], the corrosion behavior of steels with different nickel content [Nishikata, 2005], stainless steels [Cruz et al, 1996], galvanized steel [Yadav et al, 2005], zinc [Yadav, 2004] and electrochemical impedance spectroscopy [El-Mahdy et al, 2000 and Dong et al, 2016] have been extensively used to monitor atmospheric corrosion. Recent developments for monitoring atmospheric corrosion include using electric resistance sensors [Cai et al, 2005 and Li et al, 2007], pulsed Eddy current testing (ECT) [Yunze et al, 2012] and passive wireless sensors [Yasri et al, 2014]. In addition to new methods, in order to develop the ACSSM, many researchers also investigated various characteristics of corrosion. These included metal loss, material characteristics of corrosion layers [Lin et al, 2013], which were analyzed using different analysis methods such as finite element analysis (FEA) models that used two layers of the corrosion layer and test piece [Khalil et al, 2016], microscopic analysis [Wenbin et al, 2011] and X-ray diffraction [Ning et al, 2015 and Thee et al, 2015]. In addition to these techniques, electrochemical methods are useful because they allow in situ corrosion monitoring [Kasai et al, 2009]. However, precise monitoring is difficult because electrochemical methods are very sensitive to corrosion reactions. Once an electrode begins to corrode, the redox reactions of the corrosion products affect the current density signals. In the case of steel, ferrous and ferric ions coexist in the corrosion product. These factors ultimately prevent precise evaluation of atmospheric corrosion. Thus, a highly accurate in situ sensor capable of monitoring atmospheric corrosion is needed.

Against this background, we have developed a new principle for measuring corrosion rates in real time. A highly accurate in situ sensor, capable of atmospheric corrosion monitoring by measuring the thickness of carbon steel, is proposed. Previous

research on in situ monitoring of thinning of test pieces by Galvano static electrolysis [Kasai et al, 2009] has shown that strain can provide a measure of the reduction in thickness due to corrosion. However, in actual applications, there is significant noise due to variations in temperature and other factors during field measurements.

Therefore, the purpose of this study is to develop an amplifier circuit for atmospheric corrosion monitoring based on strain measurement by using the active dummy method, which has high sensitivity and can reduce the effect of temperature on the measurement environment. A dummy circuit that compensated for the temperature drift in the signal with an active circuit was successfully designed, and experiments involving Galvano static electrolysis were conducted by using the amplifier circuits to determine the thinning of test pieces through strain measurements. In addition, the effect of the temperature on the measurement environment and, therefore, the signals were investigated.

3.2. Experimental Setup

3.2.1. Strain Gauges and Their Configuration on the Test Piece

The test piece for the active circuit is TPA, and the test piece for the dummy circuit is TPD. TPA has active and dummy strain gauges at positions 1 and 3, and a strain gauge for the commercial strain measurement device at position 1. TPD has active and dummy strain gauges at positions 2 and 3. TPA has a 900 mm² corroded area at the center of the test piece; the remaining area is uncorroded. TPD only has a corroded area. The configuration of the strain gauges on the test piece is shown in Figure 3.1. Position 1 is at the center of the active test piece with curvature ρ and has active gauges (R_{AA}) on the back of the corrosion area. Position 2 is at the center of the dummy test piece with curvature ρ , and has active gauges (R_{AD}) on the back of the

uncorroded area. Position 3 is at the edge of both test pieces on the back of the uncorroded area and has dummy strain gauges (R_{DA} and R_{DD}). The first letter in the subscript denotes whether the gauge is active or dummy, while the second letter denotes whether the circuit is active or dummy. R_{AA} is placed at the center of TPA with curvature ρ to exert a stress on the strain gauges, as well as on the back of the corroded area, in order to receive signals from the corrosion-induced thinning of the test piece. R_{DA} is placed at the edge of TPA and on the back of the corroded area without stress to compensate for the effects of atmospheric conditions on the active gauge. R_{AD} and R_{DD} , as identical gauges of the active circuit, compensate for the active circuit and are placed in the uncorroded area on TPD. S_G is the strain gauge for measuring the strain in the corroded area with a commercial strain meter and is placed at the center of the corroded area without bending. The strain gauges and their functions are shown in Table 3.1.

Table 3.1 Position and purpose of strain gauges in Figure 3.1.

	Active Circuit	Dummy Circuit
Active Strain Gauge	R_{AA} : Corroded area with bending. Detects signals due to corrosion-induced thinning of test piece.	R_{AD} : Uncorroded without bending. Detects signals without thinning of test piece.
Dummy Strain Gauge	R_{DA} : Uncorroded area without bending. Compensates for effects of environmental conditions on R_{AA} .	R_{DD} : Uncorroded area without bending. Compensates for effects of environmental conditions on R_{AD} .
Strain Gauge	S_G : At the center of corroded area without bending. Measures the strain in the corroded area with commercial strain measurement device.	

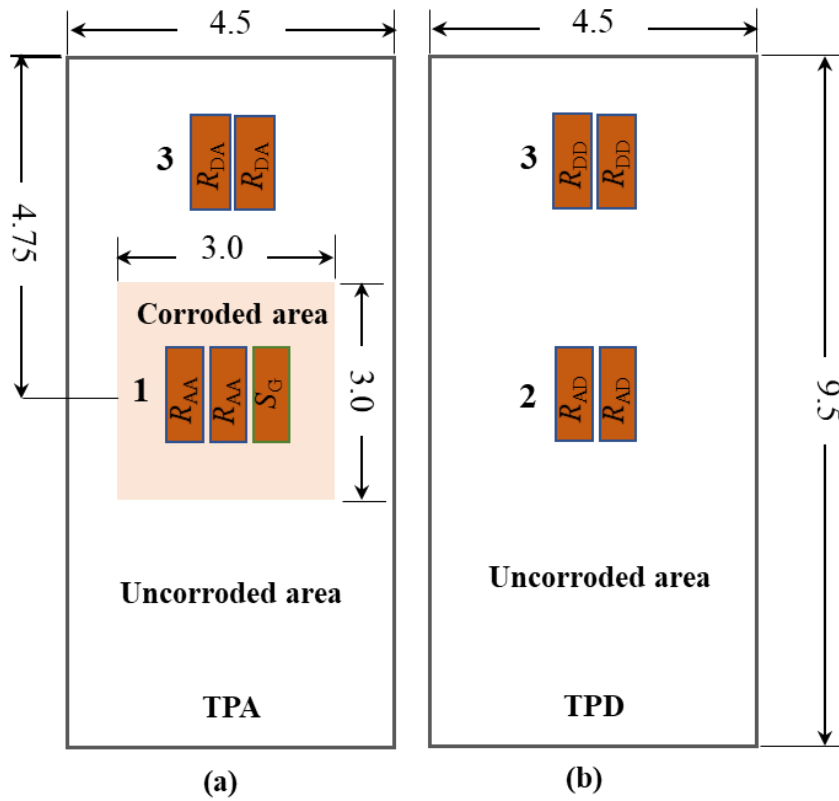


Figure 3.1 Configuration of strain gauges on test piece for ACSSM sensor. (a) TPA with 900 mm² corroded area at the center and the remaining area uncorroded. (b) TPD, with the entire test piece uncorroded. Unit is in cm.

This experiment used Tokyo Sokki FLA-5-11 strain gauges that bonded to the low carbon steel. When we bonded the strain gauges on the test piece, some procedures required to make successfully installation. The procedures are shown below:

1. Preparation supplies

Required supplies are eight Tokyo Sokki FLA-5-11 strain gauges, a low carbon steel, extra fine sand paper, acetone, cottons, pen, tape, CN adhesive, SB type, araldite and plastic coatings.

2. Surface of test piece preparation

The surface of test piece should be flat and free from defects, free of rust, scale, oxides, loose paint, or other coatings from the bonding area to provide a shiny

metallic surface. Before bonding, brush with fine abrasive paper and cleaning by acetone using the cotton/tissue. Continue cleaning until a new tissue or cloth comes away completely free of contamination. Following the surface preparation, be sure to attach the gauge before the surface becomes covered with an oxidizing membrane or becomes newly contaminated. Fine cleaning

3. Pre-Position FBG sensor

Roughly determine a location on the test specimen where the strain gauge is to be bonded. Using a drafting pen, mark the position of active and dummy strain gauges in the back side of the test piece at the properly position as shown in Figure 3.1. Attach the strain gauges using the tape to ensure the position of gauges.

4. Applying bonding adhesive

Remove the mark under the gauges using acetone. Drop a proper amount of adhesive CN onto the back of the gauge base. Use the adhesive nozzle to spread the adhesive over the back surface thinly and uniformly.

5. Curing and pressing

Place the gauge on the position, place a polyethylene sheet onto it and press down on the gauge constantly using your thumb or a gauge clamp. This should be done quickly as the curing process is completed very fast. The curing time varies depending on the gauge, test specimen, temperature, humidity and pressing force. The curing time under normal conditions is 20-60 seconds. Remove the tape

6. Raising gauge leads

After the adhesive beneath the polyethylene sheet has been perfectly cured, raise the gauge leads. Raise the leads up to a bit inside the gauge base. Put the SB type under the gauge lead and arrange the gauge lead until no connection each other.

Bonding connecting lead wires to the test piece using the adhesive CN.

Cover the strain gauges using araldite to protect the gauges from the external environment.

7. Coating the test piece

Cover the corroded area (4.5 cm × 9.5 cm) on the backside of the test piece using the tape. Spray the plastic coating to cover the all uncorroded area. Let it dry.

8. Install the test piece in the apparatus and fix it.

3.2.2. In Situ Monitoring of Thinning of Test Piece by Galvano Static Electrolysis

This experiment was carried out to investigate the accuracy of the amplifier circuit using the active dummy method, as described in Section 2.4. Figure 3.2 shows the experimental setup used to measure the change in strain due to the thinning of the TPA of the ACSSM sensor through Galvano static electrolysis. The electrolytic solution in the reservoir was 1 mol·L⁻¹ hydrochloric acid solution. The working electrode was TPA, and the counter electrode consisted of the same material as TPA. The thickness of the working electrode was reduced using Galvano static electrolysis with a current of 1 A, and the strain of the test piece was measured to assess the change in thickness. The corroded area was 900 mm². The difference in weight (ΔW) and thickness (Δh_A) of the test piece of the working electrode before and after the experiment were also measured. The data sampling interval was 30 s. TPD was set in the apparatus, near the reservoir.

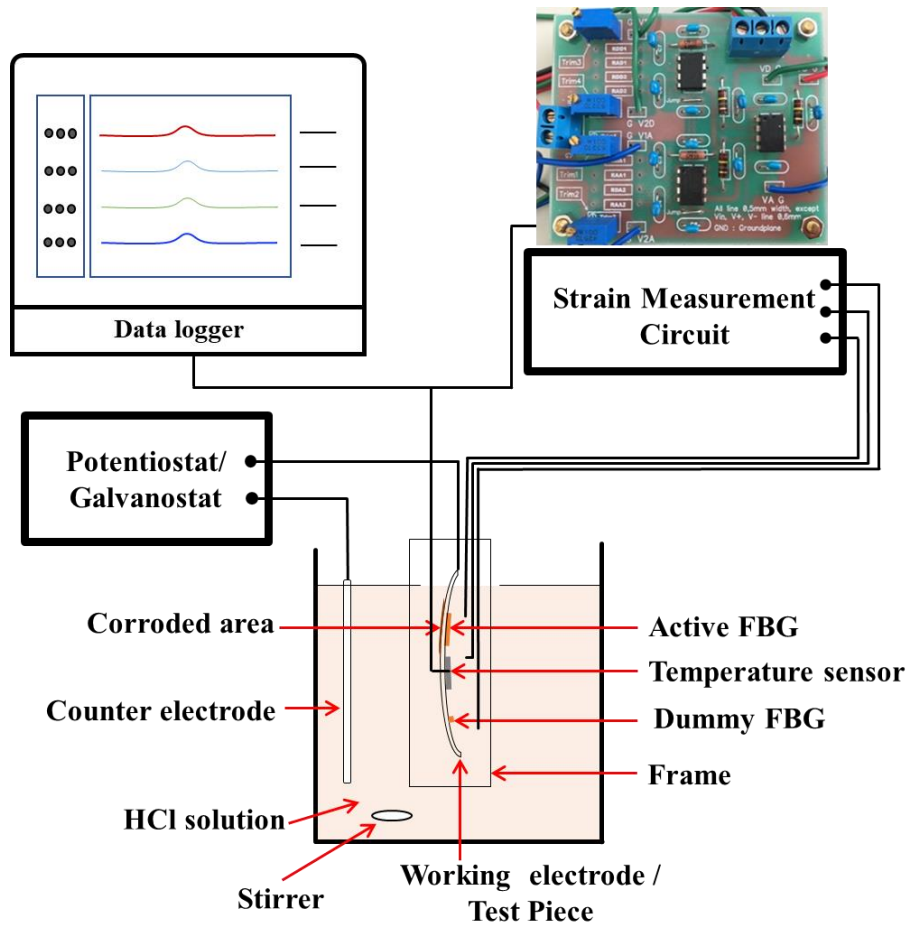


Figure 3.2 Experimental setup for measuring the thinning of a test piece by Galvanostatic electrolysis.

3.2.3. Experiment for the Compensation of Thermal Strain

To investigate the effect of environmental temperature drift on the amplifier circuit, the voltage and temperature were measured using the amplifier circuit with an active dummy before any corrosion occurred. TP_A and TP_D , with attached Tokyo Sokki FLA-5-11 strain gauges R_{AA} , R_{DA} , R_{AD} and R_{DD} , were placed in the bending position using the same configuration as in Figure 4. Both TP_A and TP_D were placed

under the same ambient conditions. The signal and temperature were monitored for 166 hours prior to corrosion, with a data sampling interval of 20 min. The ambient temperature was measured by a thermocouple set near the circuit. Figure 3.3 show the experimental set up for experiment for the compensation of thermal strain.

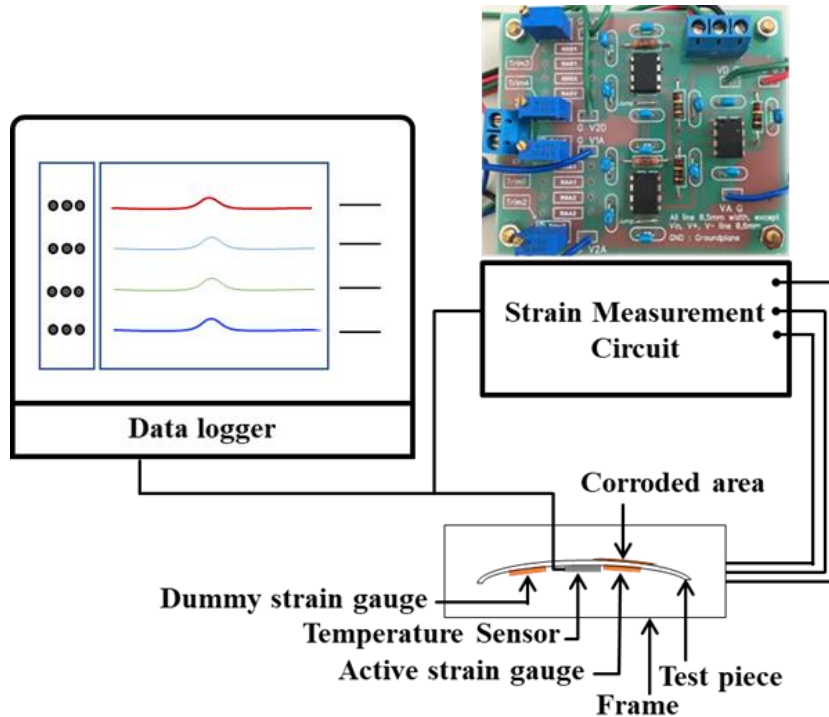


Figure 3.3 Experimental setup for experiment for the compensation of thermal strain

3.3. Results and Discussion

3.3.1. In Situ Monitoring of Thinning of Test Piece by Galvano Static Electrolysis

The results obtained by the strain gauge of the amplifier circuit for the ACSSM sensor during Galvano static electrolysis are shown in Figure 3.4. Each voltage reading of the amplifier circuit is converted to strain in advance. The figure shows the time evolution of the strain due to the change in thickness of the test piece. When the

ACSSM sensor was immersed in the reservoir, and the surface of the test piece was placed longitudinally, it was easy for the corrosion products to fall from the surface during the experiment.

The strain of the active circuit (ϵ_A) had a linear signal in terms of elapsed time during electrolysis. The strain value of the dummy circuit (ϵ_D) was constant throughout the electrolysis process. $\Delta\epsilon$ is the difference between ϵ_A and ϵ_D , which were obtained by measurements of the amplifier circuit through the active dummy method for the ACSSM sensor. $\Delta\epsilon$ increased linearly with time because, given the constant current during the experiment, Galvano static electrolysis depended on elapsed time. After electrolysis began ϵ_A linearly increased, this indicated the compressive strain on the test piece, which became smaller with the decreasing of the thickness of test piece, according to Equation (2.4).

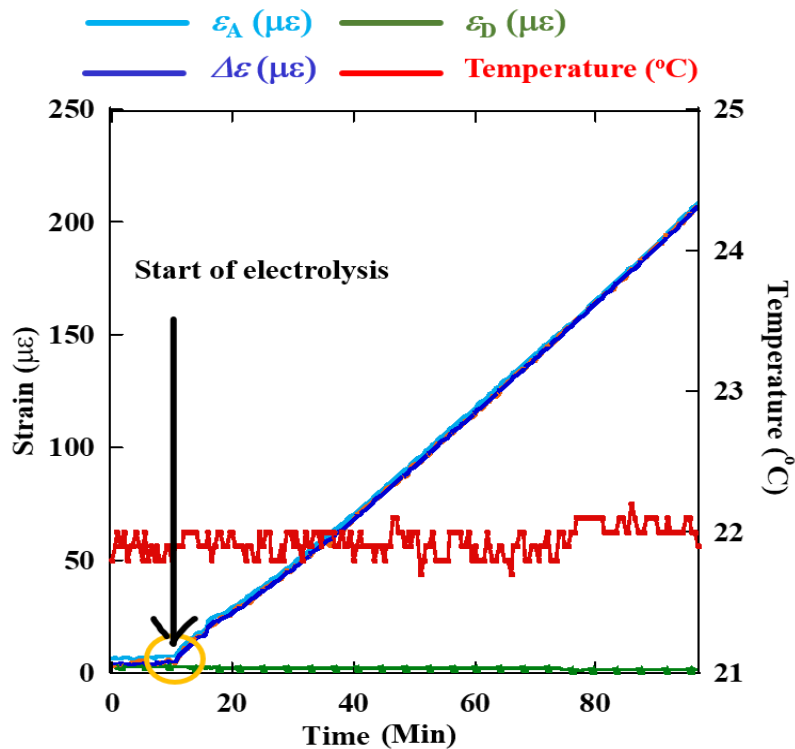


Figure 3.4 Strain signal pattern as function of elapsed time during electrolysis process.

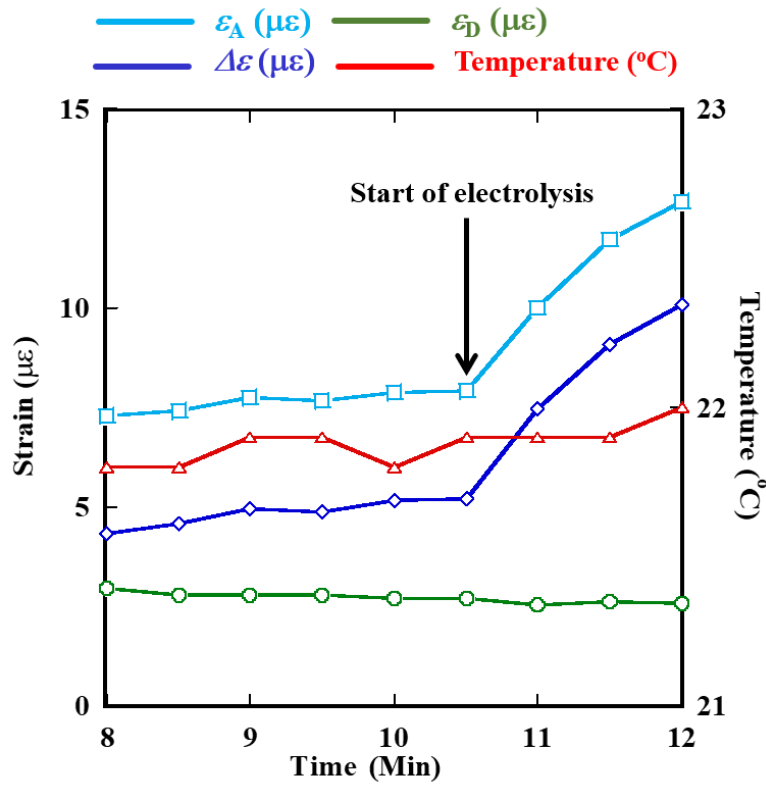


Figure 3.5 Close-up of Figure 3.4 around the start of the electrolysis process.

Figure 3.5 shows a close-up of the results around 10.5 min, when electrolysis began. Before 10.5 min, ε_A is constant. After 10.5 min, it is smaller owing to the thinning of the test piece. ε_D is completely unaffected by the signal. It can be concluded that under the active dummy method, the amplifier circuit for an ACSSM sensor can measure small values in $\mu\varepsilon$, this corresponds to the resolution of the amplifier circuit.

To investigate the accuracy of the amplifier circuit under the active dummy method, the actual thickness reduction of the test piece was measured. Δy_A is the change in thickness of the test piece, as determined by measuring the actual thickness at five different points on the corroded area of the test piece with a micrometer before and after the experiment. The measurements of the actual thickness were 0.29, 0.28,

0.28, 0.27 and 0.28 mm. The average thickness of the test piece after corrosion was 0.28 mm. Since the initial thickness was 0.48 mm, Δy_A was 0.20 mm.

ΔW is the change in weight of the test piece, as determined from the actual weights measured before and after the experiment and by using the relationship:

$$\Delta y_W = \frac{\Delta W}{S d} \quad (3.1)$$

where ΔW is the change in weight, S is the corroded area of the test piece, and d is the density of the test piece. In this study, $\Delta W = 1.42$ g, $S = 900$ mm², and $d = 0.0078$ g·mm⁻³. Furthermore, Δy was obtained via the relationship between Δy and $\Delta \epsilon$, as described in Section 2.1. The measurement results obtained through calculations of actual thickness and actual weight of the test piece are arranged in Table 3.2. Δy was well aligned with Δy_A and Δy_W , since the errors in the errors in these two latter measurements were at approximately 12 %.

Table 3.2 Determination of thickness reduction from measured strain, thickness, and weight.

	Δy	Δy_A	Δy_W
Thickness (μm)	177	200	202
Error (%)	-	11	12

3.3.2 Strain Due to Temperature Change of Measurement Environment

Fig. 10 shows the original experimental results of the thermal strain experiment which lasted 88 hours before corrosion, as described in Section 3.4. T_{TP} is the temperature signal of the test piece in °C, ϵ_A is the strain from the active FBG sensor in $\mu\epsilon$, ϵ_D is the strain from the dummy FBG sensor in $\mu\epsilon$ and $\Delta \epsilon$ is the difference in strain between ϵ_A and ϵ_D in $\mu\epsilon$. ϵ_A and ϵ_D had a similar response to temperature

variations. If only the active FBG sensor was used, the variation in ε_A would be high, approximately 52 $\mu\varepsilon$ at 2.8°C. $\Delta\varepsilon$ as the proposed signal has a more accurate and constant signal in the range of 10 $\mu\varepsilon$ and was obtained during experiment. This result showed that $\Delta\varepsilon$ can be used for strain measurement to determine the atmospheric corrosion rate, which requires high resolution and long-term data monitoring in the field

Figure 3.6 shows the original experiment results starting 166 hours before corrosion, as described in Section 3.2.3. It is seen that ε_A and ε_D have a similar response to temperature variation. When only the active circuit is used, the variation in ε_A is high, at about 30 $\mu\varepsilon$. The dummy circuit can compensate for the variation by subtracting the same response signal as $\Delta\varepsilon$. The variation in $\Delta\varepsilon$ with temperature is small, at less than 10 $\mu\varepsilon$. To get a more accurate and constant value for $\Delta\varepsilon$, the relationship between temperature and $\Delta\varepsilon$, (see Figure 13) was adjusted.

In Figure 3.7, the effect of temperature on $\Delta\varepsilon$ follows the equation of the master curve $\Delta\varepsilon = 4.68 - 0.68T$. This means that temperature shifts $\Delta\varepsilon$ by about 0.68 $\mu\varepsilon$ per °C. By using this equation, $\Delta\varepsilon$ was corrected to reduce the effect of the temperature of the measurement environment.

$\Delta\varepsilon_T$ is the signal of $\Delta\varepsilon$ obtained after the equation for the relationship between temperature and $\Delta\varepsilon$ was applied. The value of $\Delta\varepsilon_T$ is more constant than $\Delta\varepsilon$.

Furthermore, a moving average analysis was conducted. Corrosion is not a rapid process rather it occurs over longtime spans. A moving average analysis, which enables long-time-span analysis of signals, serves to distribute the data. Indeed, as the results in Figure 3.8 show, the signal obtained is smoother and more constant than the original results.

Figure 3.8 shows the moving average analysis of the signal pattern of strain using 100 interval data. ϵ_{AM} is the strain of the active circuit after the moving average analysis, and ϵ_{DM} is the strain of the dummy circuit after moving average analysis. $\Delta\epsilon_M$ is the strain of the amplifier circuit after moving average analysis, which is obtained from the difference between ϵ_{DM} and ϵ_{AM} . From Figure 3.8, $\Delta\epsilon_M$ is significantly more constant than $\Delta\epsilon_T$. This indicates that the moving average is needed in this experiment for accurate measurement without the effect of the temperature variation of the measurement environment.

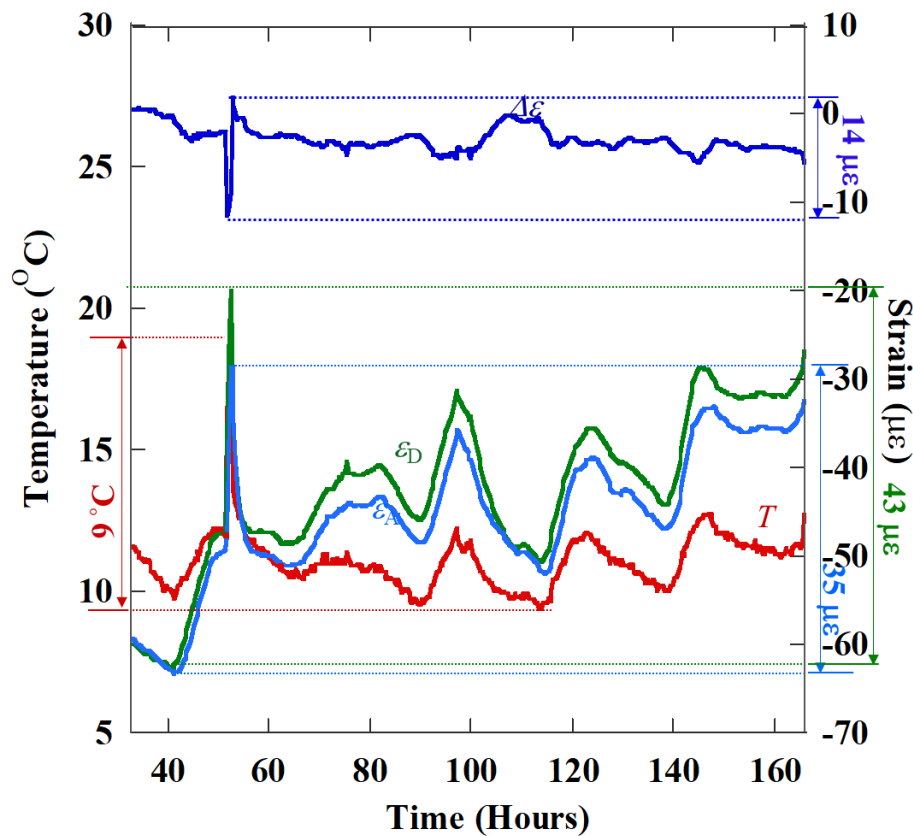


Figure 3.6 Signal pattern before corrosion is applied.

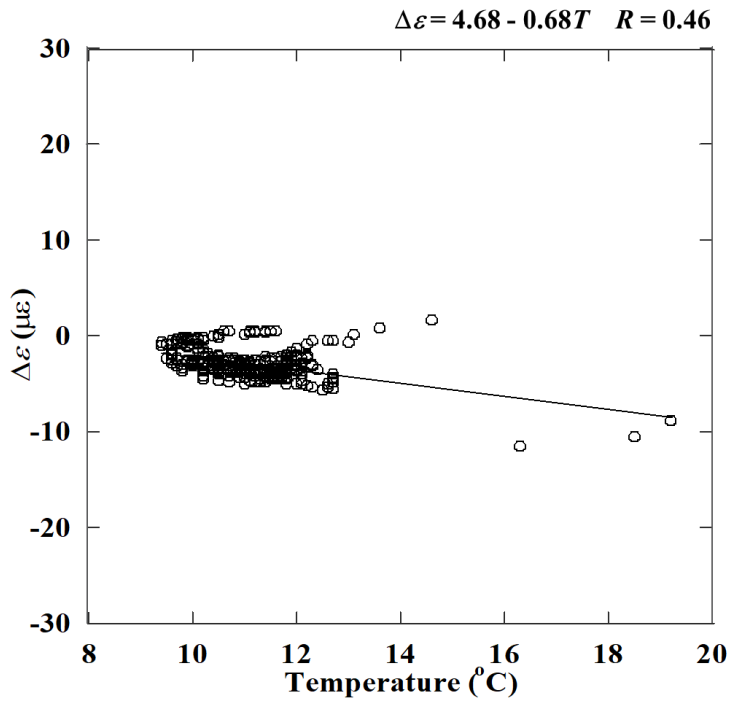


Figure 3.7 Relationship between voltage temperature.

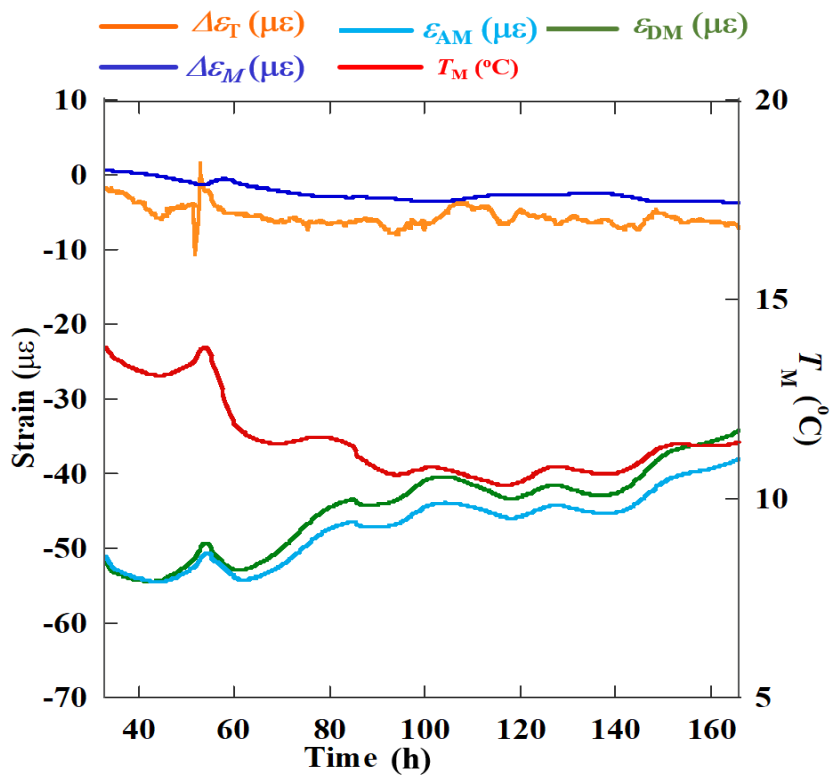


Figure 3.8 Signal pattern of voltage before corrosion is applied with the moving average.

3.4. Summary

The conclusions of the present study are as follows:

1. The performance of ACSSM with an active dummy method using strain gauges for measuring the thickness of low-carbon steel was presented.
2. An amplifier circuit using the active dummy method for an ACSSM sensor based on strain measurement was developed. It successfully overcomes the noise from the environment by compensating from the dummy circuit to the active circuit.
3. The master curve of strain versus voltage for the newly developed amplifier circuit indicated high sensitivity with a slope of $39 \mu\epsilon/V$.
4. The experiment on the thickness reduction of the test piece by Galvano static electrolysis revealed strong alignment between the calculated results and the strain measurements made with the amplifier circuit by using the active dummy method. The error rate was approximately 12%.
5. The strain due to temperature variation was obtained via $\Delta\epsilon = 4.68 - 0.68T$. The effect of temperature on $\Delta\epsilon$ was around $0.68 \mu\epsilon$ per $^{\circ}C$.
6. $\Delta\epsilon_T$ remained slightly more constant than $\Delta\epsilon$ with temperature variations in the measurement environment.
7. $\Delta\epsilon_M$ was significantly more constant than $\Delta\epsilon_T$, which indicated that the moving average should be used in experiments to obtain more accurate measurements.
8. In the field measurement, the corrosion layers of the test piece of the ACSSM sensor might affect the signals, and its effect would benefit from further study. After developing the ACSSM sensor system including an amplifier circuit using the active dummy method and unveiling the effect of corrosion layers on the signal, atmospheric corrosion of steel structures can be estimated with an ACSSM sensor

system. The ACSSM sensor can be installed on different surfaces of the structure. The relationship of corrosion progression and strain measurement need to be further verified in the future.

Chapter 4

ACSSM with an Active Dummy Method FBG Sensor by Galvanostatic Electrolysis

4.1. Introduction

In the last decade, optic fibers, including FBG have been widely used in many measurement applications for structural health monitoring (SHM), such as monitoring a metal bridge [Rodrigues et al, 2012], monitoring the corrosion process in concrete [Omar et al, 2017], monitoring the stretching of cables in a gymnasium structure [Li et al, 2013], monitoring the displacement of a landslide [Lin et al, 2018], and detecting the welding joints in a structure [Murayama et la, 2011]. Atmospheric corrosion sensors that can predict the corrosion rate in steel structures are very important for evaluating safety levels in structural health monitoring. Several FBG-based methods of atmospheric corrosion monitoring in steel structures have been proposed.

FBGs have been used to monitor the progress of corrosion in reinforced concrete [Grattan et al, 2009], composite specimens for aircraft [Tan et al, 2017] and steel [Emmons et al, 2010]. FBG sensors have been used for corrosion monitoring in

advance materials; sensors were embedded in a chemical coating using a metal film [Hu et al, 2011 and 2017], and the cladding of an FBG sensor was etched [Hassan et al, 2012] to increase the sensitivity of the sensor. Since the accuracy of measurements by atmospheric corrosion sensors with FBG sensors depends on the thermal strain that generated by the effects of temperature drift, the accurate strain measurements using FBG are needed. ACSSM using strain gauges [Purwasih et al, 2018] have presented good agreement in measurement of strain from the thickness reduction of a test piece due to corrosion by galvanostatic electrolysis [Kasai et al, 2009].

Based on this background, we have developed a method for the measurement of corrosion rates in real time using an active dummy FBG sensor. This study uses an ACSSM based on an active dummy method with FBG sensors, which have high sensitivity and accuracy. The mechanical parameters of elastic strain, reduction in thickness and thermal expansion in the test piece were determined by FEM to determine a good configuration of the active and dummy FBG sensors. The effect of temperature on the measurement environment was investigated by FEA and experimentally. In addition, the accuracy of the thickness reduction of the test piece due to corrosion was calibrated with laboratory experiments using galvanostatic electrolysis.

4.2. Experimental Setup

4.2.1. FBG Sensors and their Configuration on the Test Piece

This experiment used two os3200 FBG strain sensors and one os4210 FBG temperature sensor with configuration on the test piece as shown in Figure 4.1. The corroded area was 14 cm² on the surface of the test piece, as shown in Figure 4.1 (a),

and the FBG was placed on the backside of the test piece in the compressed curvature, as shown in Figure 4.1 (b). Figure 4.1 (c) is the real picture of FBGs in the test piece. The position of the active FBG was longitudinal under the corroded area, and the dummy FBG was transversal. Based on the FEM simulation, this FBG configuration is the best position because the strain distribution after thickness reduction occurred in corroded area, it did not affect the strain at dummy position.

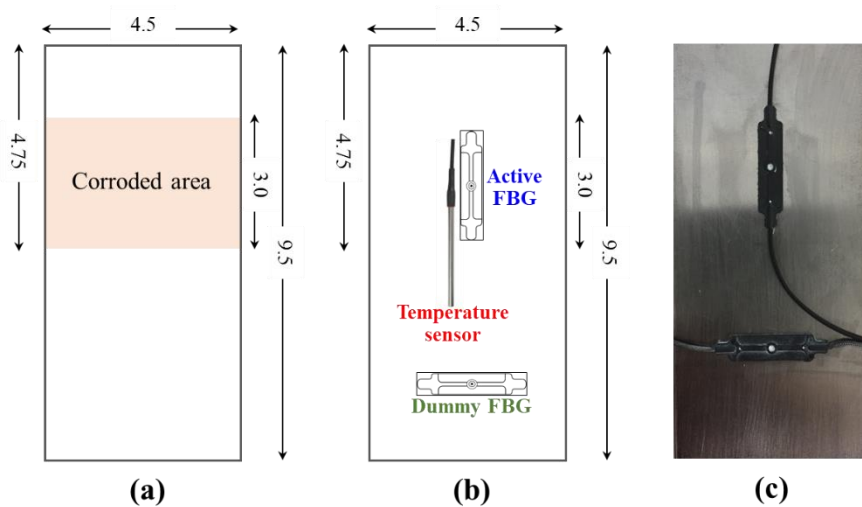


Figure 4.1. Configuration of active and dummy FBG sensor on the (a) front side (b) backside of the test piece (c) the real picture of FBG sensors attached in the test piece

The os3200 is based on fiber Bragg grating (FBG) technology for measuring the strain of the test piece. Figure 4.2 shows the diagram of os3200 FBG sensor and its dimension. When an os3200 FBG bonded to the test piece, we need pay attention for the successful FBG sensor installation. Surface preparation and cleaning are extremely important in obtaining a secure bond. The procedure os3200 FBG sensors installation outlined below:

1. Preparation supplies

Required supplies are os3200 Strain FBG, a low carbon steel, extra fine sand paper, acetone, cottons, pen, tape, Loctite® Hysol® 1C-LV, 50ml EPS Cartridge (Loctite 83208), Dual Cartridge Manual Applicator, 2:1 (Loctite 98472), Mix Nozzle (Loctite 98455), 3ml Syringe with Luer-Lok™ Tip (BD 309585), Dispenser Tip (EFD 5120TT-B).

2. FBG sensor preparation

The os3200 FBG sensor has an adhesive pre-applied to the bottom surface of the sensor. The adhesive is covered with a protective backing. When the sensors are ready to install at properly position, the protective backing can be removed from the backside surface.

3. Surface of test piece preparation

The surface of test piece should be flat and free from defects, free of rust, scale, oxides, loose paint, or other coatings. Start by brushing with fine sandpaper and cleaning by acetone using the cotton. Abrade the surface as necessary to remove surface irregularities and contamination.

4. Pre-Position FBG sensor

Using a drafting pen, mark the position of active FBG sensor and dummy FBG sensor in the back side of the test piece at the properly position as shown in Figure

4.1. Attach the FBGs using the tape to ensure the position of sensor

5. Apply FBG sensor

Remove the mark under the sensor using acetone. Remove protective backing from bottom surface of FBG. Carefully position FBG sensor over test piece and press firmly into place. Remove the tape.

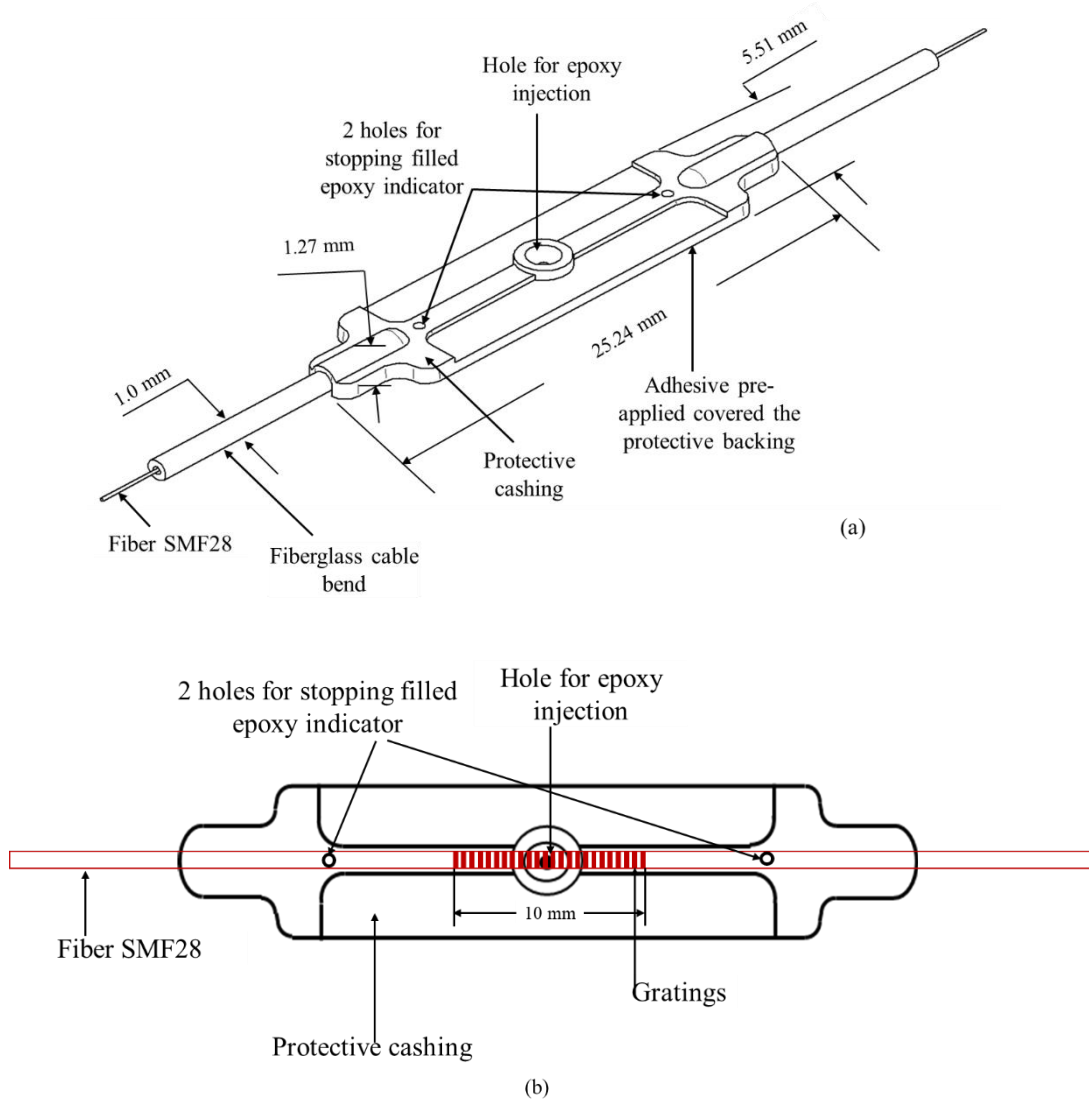


Figure 4.2. The diagram of os3200 FBG sensor (a) Dimension of os3200 FBG sensor and its protection (b) Position of gratings in FBG sensor

6. Inject Epoxy

Place epoxy cartridge in proper dispenser. To begin using new cartridge, remove cap and dispense a small amount of adhesive, making sure both Part A and B are extruding. Attach nozzle and dispense approximately 1-2" to ensure that the mixing tip is filled with both resin and hardener. Remove plunger from 3ml Syringe and install dispenser tip on end of syringe. Insert tip of dispensing nozzle into the back of the syringe and inject epoxy into the syringe. Try to lay a bead of epoxy on the

sidewall of the syringe. This will allow the air to be purged from the syringe. Insert plunger into syringe and press plunger to force air out of syringe. 1ml of epoxy is more than enough to install a handful of gages. Wipe excess epoxy off of syringe dispenser tip. Insert dispenser tip into hole located in the center of the os3200 gage. Hold dispenser tip against gage with gentle pressure. It is not necessary to press hard. Excessive pressure may damage fiber Bragg grating. Press syringe plunger down to force epoxy into sensor. Continue to apply pressure to plunger until epoxy is visible at the two vent holes located at each end of sensor. Measurements can be taken after the epoxy cures in 24 hours at room temperature [20°C to 30°C].

7. Coating the test piece

Cover the corroded area (4.5 cm × 9.5 cm) on the backside of the test piece using the tape. Spray the plastic coating to cover the all uncorroded area. Let it dry.

8. Install the test piece in the apparatus and fix it.

4.2.2. Experiment for the Compensation of Thermal

The experimental setup for the thermal strain experiment is shown in Figure. 4.3. This experiment aims to investigate the strain of FBG sensor that affected by the environmental temperature drift. Strain and temperature reflection spectra were measured with a commercial optical interrogation unit from Micron Optics (optical sensing interrogator, model sm125) and displayed by ENLIGHT Software for 88 hours with a data sampling interval of 1 min. The two os3200 FBGs from Micron Optics were used as active and dummy strain sensors. The os4210 FBG was used as the temperature sensor. This experiment provided the initial data for further experiments, including an accelerated test using a galvanostatic electrolysis.

os3200 FBG sensors was used to monitor strain in the active and dummy sensors. The active and dummy sensors used identical parameters to produce the same signal trends. Based on Equation 2.17, we determined strain as equations below:

$$\Delta\lambda_B = [k\varepsilon + (\alpha_A + \alpha_n)\Delta T]\lambda_B \quad \dots\dots\dots (4.1)$$

$$\varepsilon = \frac{\Delta\lambda_B}{k\lambda_B} - \frac{1}{k}(\alpha_A + \alpha_n)\Delta T \quad \dots\dots\dots (4.2)$$

From the concept of active dummy method in 2.5, we measured the ε_A , and ε_D $\alpha\rho\varepsilon$ using

$$\varepsilon_A = \left(\frac{\Delta\lambda_{BA}}{k\lambda_{BA}}\right) - \frac{1}{k}(\alpha_A + \alpha_n)\Delta T \quad \dots\dots\dots (4.3)$$

$$\varepsilon_D = \left(\frac{\Delta\lambda_{BD}}{k\lambda_{BD}}\right) - \frac{1}{k}(\alpha_A + \alpha_n)\Delta T \quad \dots\dots\dots (4.4)$$

And calculate the $\Delta\varepsilon$ as below

$$\Delta\varepsilon = \varepsilon_A - \varepsilon_D \quad \dots\dots\dots (4.5)$$

$$\Delta\varepsilon = \left(\frac{\Delta\lambda_{BA}}{k\lambda_{BA}}\right) - \left(\frac{\Delta\lambda_{BD}}{k\lambda_{BD}}\right) \quad \dots\dots\dots (4.6)$$

Where ε_A is the output of active FBG in $\mu\varepsilon$, ε_D is the output of dummy FBG in $\mu\varepsilon$, and $\Delta\varepsilon$ is the difference between active strain and dummy strain in $\mu\varepsilon$, $\Delta\lambda_{BA}$ is change of wavelength of active FBG in nm, $\Delta\lambda_{BD}$ is change of wavelength of dummy FBG in nm, λ_{BA} is initial wavelength of active FBG in nm, λ_{BD} is initial wavelength of dummy FBG in nm k is gage factor. This experiment used os3200 FBG sensor from Micron Optic to monitor strain in the active and dummy sensors with the initial wavelength 1548 nm for both gage and $k = 0.796$.

For monitoring the temperature, an os4210 FBG temperature probe from Micron Optic was attached on the test piece using the special yellow tape. Figure 4.4 show the photograph of os4210 FBG sensor and its dimension. The os4210 temperature probe

that it is based on FBG technology is sealed by 302 stainless steel tube that is designed to make handling easy and sensor installation fast and repeatable. Stainless steel tube has high conductivity and there is no epoxy holding the fiber to the tube. For attachment only using the special yellow tape. The long term stability is ensured by design. The sensor has initial wavelength λ 1556 nm. Based on the data sheet of os4210 FBG, the temperature can be determined by Equation (4.7) below:

$$T_{TP} = C_3(\lambda + \lambda_{OS})^3 + C_2(\lambda + \lambda_{OS})^2 + C_1(\lambda + \lambda_{OS}) + C_0 \quad \dots\dots\dots (4.7)$$

T_{TP} is temperature that the FBG probe attached on the test piece in °C. The other variable can be shown in Table 4.1 below:

Table 4.1 Variable Description for FBG Temperature Probe

Variable	Description	Value	Units
λ_{OS}	Wavelength Offset	-12.0792	nm
C_3	Calibration Coeff. 3	3.752985285687830	°C/nm ³
C_2	Calibration Coeff. 2	-17397.5339327845	°C/nm ²
C_1	Calibration Coeff. 1	26883058.03622590	°C/nm
C_0	Calibration Coeff. 0	-13846811800.8607	°C

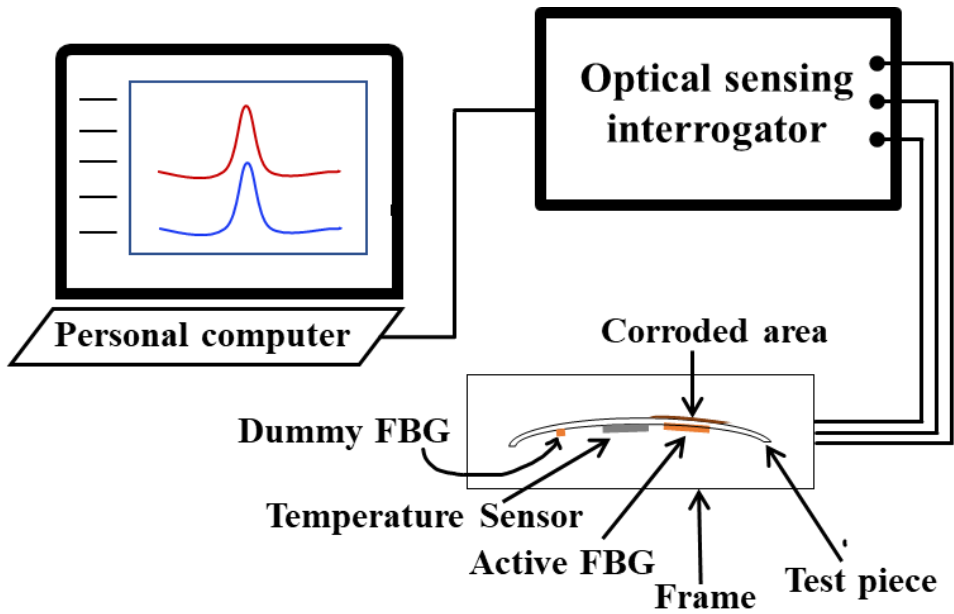


Figure 4.3 The experimental set-up for the compensation of thermal strain

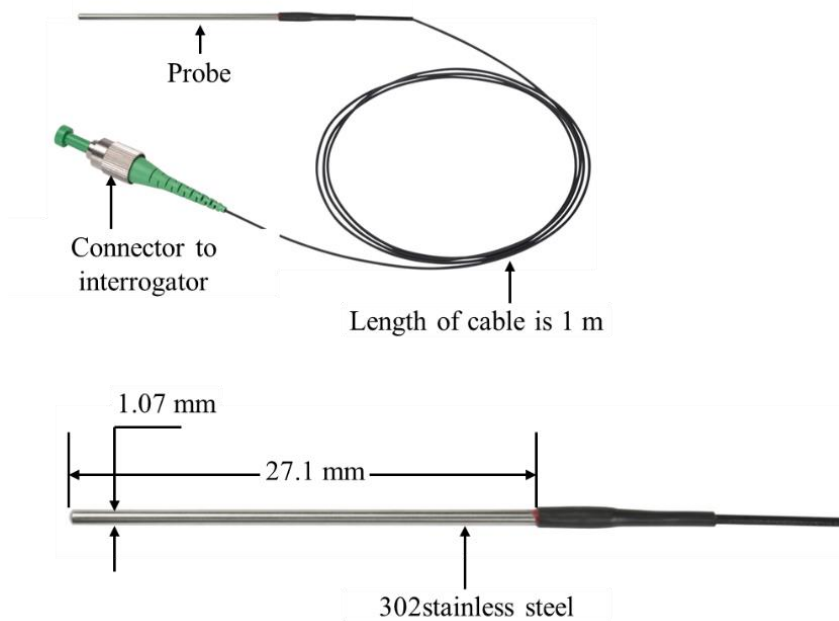


Figure 4.4 The photograph of os4200 FBG temperature probe and its dimension

4.2.3. Accelerated laboratory test using galvanostatic electrolysis

This experiment was carried out to investigate the accuracy of the FBG sensor in the test piece. Figure 4.5 shows the experimental setup used to measure the change in

strain due to the thickness reduction of the test piece using galvanostatic electrolysis. The electrolytic solution in the reservoir was $1 \text{ mol}\cdot\text{L}^{-1}$ hydrochloric acid solution. The working electrode was the test piece with the FBG sensor and the counter electrode consisted of the same material as the test piece. The thickness of the working electrode was reduced using galvanostatic electrolysis with a current of 0.3 A , and the strain of the test piece was measured to assess the change in thickness. Δh of the test piece in the working electrode before and after the experiment was also measured. The data sampling interval was 30 seconds.

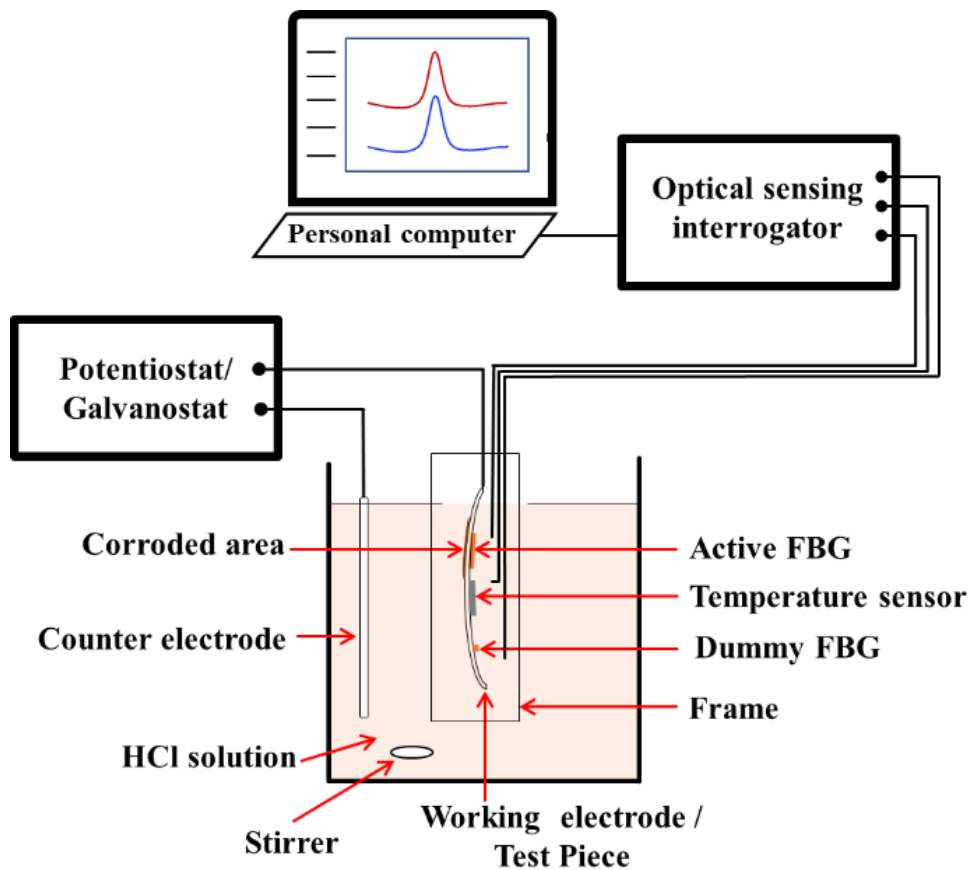


Figure 4.5 The experimental set up for the accelerated laboratory test using galvanostatic electrolysis

4.3 Results and Discussion

4.3.1 Experiment for the Compensation of Thermal Strain

Figure 4.6 shows the original experimental results of the thermal strain experiment which lasted 88 hours before corrosion, as described in Section 4.2.2 T_{TP} is the temperature signal of the test piece in $^{\circ}\text{C}$, ε_A is the strain from the active FBG in $\mu\varepsilon$, ε_D is the strain from the active FBG in $\mu\varepsilon$ and $\Delta\varepsilon$ is the difference in strain between ε_A and ε_D in $\mu\varepsilon$. ε_A and ε_D had a similar response to temperature variations. If only the active FBG was used, the variation in ε_A was high, approximately $52 \mu\varepsilon$ at 2.8°C . The dummy FBG could compensate for the variation by subtracting the response signal of the active FBG. Using $\Delta\varepsilon$ as the proposed signal, a more accurate and constant signal in the range $10 \mu\varepsilon$ was obtained at 2.8°C . This result showed that $\Delta\varepsilon$ can be used for strain measurement to determine the atmospheric corrosion rate, which requires high resolution and long-term data monitoring in the field.

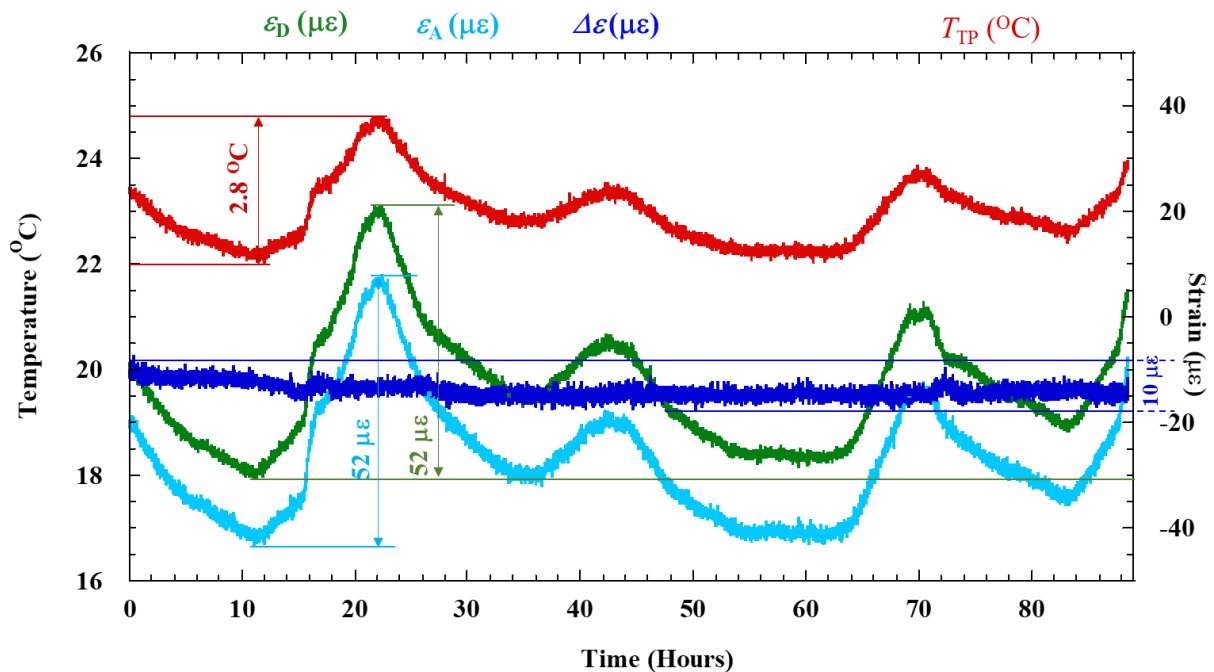


Figure 4.6 Variation in the strain signal pattern before corrosion occurs.

4.3.2. Galvano-static electrolysis experiment

Figure 4.7 shows the results of the galvanostatic electrolysis experiment. ε_A had a linear signal in terms of elapsed time during electrolysis. ε_D was constant throughout the electrolysis process and demonstrated the same tendency as the temperature signal. $\Delta\varepsilon$ is the difference between ε_A and ε_D .

To calibrate the accuracy of the FBG sensor with the active dummy method, the actual thickness and weight of the test piece were measured before and after the electrolysis process. Δh_T is the change in thickness of the test piece, as determined by measuring the actual thickness at several different points on the corroded area of the test piece with a micrometer. The average thickness of the test piece after corrosion was 0.36 mm. Since the initial thickness was 0.48 mm, Δh_T was 0.12 mm.

ΔW is the change in weight of the test piece, as determined from the actual weights measured before and after the experiment and by using the relationship:

$$\Delta h_W = \frac{\Delta W}{S d} \quad (4.8)$$

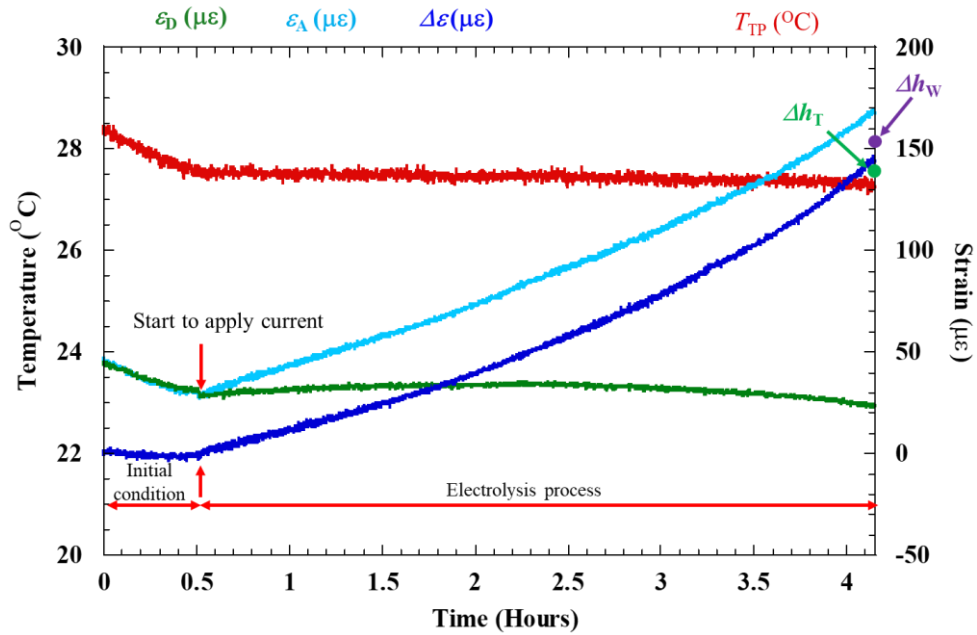
where ΔW is the change in weight, S is the corroded area of the test piece (1350 mm²), and d is the density of the test piece (0.0078 g·mm⁻³), Δh_W was 0.132 mm.

Δh was obtained via the relationship between Δh and $\Delta\varepsilon$, as described in Section 2.1. The final value of $\Delta\varepsilon$ from the experiment was 143 $\mu\varepsilon$, which corresponded to 120 μm . A comparison of the measurement results, actual thickness and thickness calculated from the actual weight of the test piece is given in Table 4.2. Δh agreed well with Δh_T and Δh_W .

Table 4.2 Comparison of thickness reduction with measured thickness and weight.

	Δh	Δh_T	Δh_W
Thickness (μm)	123	120	132
Error (%)	-	2.5	7.5

The results show that FBG sensor is better than experiment for ACSSM using strain gauge which has error 12%. As we predicted, the results with FBG were accurate, high resolution and stable because the FBG only has sensor temperature dependence. Meanwhile, ACSSM using strain gauge has temperature dependence of amplifier



circuit and sensor itself.

Figure 4.7 Strain signal pattern as function of elapsed time during the electrolysis process

4.3.3. Discussion

The ACSSM with an active dummy method can be performed by using strain gauges and FBG sensors. According to the accuracy characteristic, the experiment using strain gauges and FBG sensors can be compared in parameter accuracy such as temperature variation, error in measurement, stability of signal and percent of decreasing compensation of signal. From the experiment result of the ACSSM with an active dummy method using strain gauge as described in Chapter 3 and the using FBG sensor in this chapter, we obtained the comparison result between strain gauge and FBG sensor as shown in Table 4.3 below:

Table 4.3 Comparison of accuracy parameter for ACSSM using strain gauges and FBG sensors.

Parameter of accuracy	Sensor	
	Strain gauge	FBG sensor
Temperature variation of ε_A and ε_B	4.8 $\mu\varepsilon/^\circ\text{C}$	18.5 $\mu\varepsilon/^\circ\text{C}$
Temperature variation of $\Delta\varepsilon$	1.6 $\mu\varepsilon/^\circ\text{C}$	3.6 $\mu\varepsilon/^\circ\text{C}$
Error in electrolysis experiment	12 %	7.5%
Stability signal of $\Delta\varepsilon$	Fluctuating	Very constant signal
Percent of compensation	67%	80%

The temperature variation of FBG sensor came from the thermal expansion of material specimen, the thermal expansion and the thermo-optic of FBG sensor, totally is 18.5 $\mu\varepsilon/^\circ\text{C}$. The result shows that using strain gauges, temperature variation is smaller than using FBG sensor. This occurred because of in strain gauges measurement system, the temperature compensation not only compensates the strain gauge in bridge circuit

but also compensate the amplifier circuit by applying the dummy circuit. Meanwhile, using the FBG sensor only compensate the FBG sensor. But in this research, the constant signal of $\Delta\varepsilon$ is very important in strain measurement. In spite of FBG sensor has only sensor compensation, but it can compensate the temperature variation until 80%.

4.4. Summary

The conclusions of the present study are as follows:

1. The performance of ACSSM with an active dummy method using FBG sensors for measuring the thickness of low-carbon steel was presented.
2. A good correlation between analytical results determined using the mechanical properties of materials and FEA was obtained. This correlation indicates that the principle of atmospheric corrosion sensors is reasonable.
3. The thermal expansion and the thickness reduction in the test piece were applied in FEM analysis with the temperature change ΔT . We verified the proper configuration of the active dummy FBG on the test piece.
4. From the thermal strain experiment, the active FBG strain ε_A has high the variation strain caused by temperature, approximately $18.6 \mu\varepsilon/^\circ\text{C}$, similarly the dummy FBG strain ε_D . By subtracting the response signal of the active FBG, the dummy FBG strain can compensate the variation. It was the proposed signal $\Delta\varepsilon$.
5. Using $\Delta\varepsilon$ as the proposed signal, a more accurate and constant signal was obtained in the range of $3.6 \mu\varepsilon/^\circ\text{C}$, and this signal successfully overcame the noise from the environment by compensating between the dummy FBG and the active FBG.

Based on this method, $\Delta\varepsilon$ can be used for strain measurements to determine the atmospheric corrosion rate, which requires long term data monitoring in the field.

6. The experiment on the thickness reduction of the test piece by galvanostatic electrolysis exhibited strong alignment between the calculated results and the strain measurements obtained by the active dummy method using FBG sensors. The error was approximately 7.5 %.
7. Comparing the results with experiment for ACSSM using strain gauge which has error 12%. As we predicted, the results with FBG were accurate, high resolution and stable because the FBG only has sensor temperature dependence. Meanwhile, ACSSM using strain gauge has temperature dependence of amplifier circuit and sensor itself.

The atmospheric corrosion of steel structures can be estimated by ACSSM using FBG sensors installed on different surfaces of the structure. By modifying the material of the test piece to the actual material of structures, the ACSSM will contribute to effective decision making for the maintenance of steel structures.

Chapter 5

Dry-wet Method for ACSSM

5.1. Introduction

The dry-wet method had a widely used for investigating the behavior of corrosion product in metal. To give the detail information about the corrosion product behavior, many researchers conduct the dry wet method. Yadav et al, 2004, investigated the atmospheric corrosion of Zn using ac impedance and differential pressure meter. Gamal A. EL-Mahdy, 2004 studied atmospheric corrosion that monitored the corrosion rate of copper during cyclic wet/dry conditions and in a chloride containing environment together with the variations of surface orientation, temperature and pH of solution using an EIS impedance technique. The corrosion rate of copper increases rapidly during the initial stages of exposure then decreases slowly and eventually attains the steady state during the last stages of exposure. The corrosion products were analyzed using X-ray diffraction. The corrosion mechanism for copper studied under wet/dry cyclic conditions was found to proceed under the dissolution–precipitation mechanism. Ch. Thee et al, 2014, studied the atmospheric corrosion monitoring using EIS on a weathering steel under wet–dry cycles condition. There are five stages in

illustrating the corrosion evolution in wet-dry simulation. Stage I is the first wet-dry cycle, there is no corrosion product covering the surface. Next stage is the earlier stage, there is thin corrosion product with no ability in resisting corrosive ions. Maximum corrosion rate stage is stage when the protective effect of the corrosion product layer is in balance with the corrosion effect. The subsequent stage is when the corrosion product grows in thickness with improved ability in resisting corrosive ions. The last stage is later stage, the corrosion reaches a stable stage and corrosion rate proceeds. Chiavaria et al, 2015, investigated the atmospheric corrosion on fire-gilded bronze before and after artificial ageing by dry wet exposure. The electrochemical tests on gilded bronze during wet & dry exposure show a decrease of the corrosion rate with time. This is due to local accumulation of insoluble bronze corrosion products, which tend to obstruct the gold layer pores. Mei YU et al, 2017, studied to detect the stress corrosion behavior and mechanism of aluminum alloy under wet-dry cyclic condition with/without pre-immersion. A slow strain rate test (SSRT), an electrochemical test, a scanning electron microscope (SEM), and a transmission electron microscope (TEM) are employed to obtain useful information on the effects of these factors. Kiosidoua et al, 2018, presented the various models of finite length diffusion impedance in order to find the optimum description for dissolved oxygen diffusion, during corrosion of scribed coated steel in cyclic salt spray conditions in time week intervals.

In this research, the author conducts the dry wet method using the ACSSM with an active dummy method to investigate the behavior of corrosion product. The mechanism of corrosion during the dry wet condition by spraying 5% NaCl solution was applied to investigate the performance of the corrosion product to the strain using the ACSSM. The ACSSM using strain gauges and FBG sensors were conducted for

compensation thermal strain without spraying and during dry-wet condition. For calibrating the value of strain, the thickness and weight loss of coupons was carried out simultaneously with the strain measurement.

5.2. Experimental Setup for Dry-wet Method Using ACSSM

Experiment for informing the potential for monitoring corrosion in atmospheric conditions, a dry–wet cyclic exposure experiment was carried out by periodically with applying a 5.0 wt % NaCl solution to the test. The experiment used the of apparatus that comprises of base and cover which has $\rho = 430$ mm, referring to Section 2.3, and the test piece which has 95mm in length, 45mm in width and 0.5 mm in thickness and with the corroded area is 1350 mm². The experiment was conducted in two stages: Compensation of thermal strain experiment or initial experiment before spraying the salt solution and dry-wet experiment with spraying salt solution. To calibrate the strain measurement, we set several coupons which applied the same material and same spray with the test piece. These experiments used the ACSSM using strain gauges and FBGs. The experimental set-up for these two types of sensors will be explained below.

5.2.1. Dry-wet Method for ACSSM Using Strain Gauges

Using the amplifier circuit in Section 2.5 which has an active circuit, dummy circuit and differential circuit and consist of 8 FLA-5-11 strain gauges from Tokyo Sokki. Every two strain gauges has a different function in the amplifier circuit. The active circuit consist of two active gauges which attached under the corroded area and two dummy gauges under corroded area. The dummy circuit consist of four gauges which attached under the uncorroded area. All gauges attached in the one test piece with the configuration of gauges in the test piece was shown in Figure 5.1. $\Delta\varepsilon$ is the

proposed strain that determined the thickness reduction due to the corrosion. The test piece put in the apparatus and the edges of the test piece was fixed.

Figure 5.2 shows the experimental set-up of the dry-wet experiment using strain gauges. The data logger Graphtec GL7000 monitored the output voltage from the active circuit, dummy circuit and differential circuit every 10 minutes and measured the temperature simultaneously with a thermocouple. Using the relationship between strain and voltage in Section 2.5.3 with gain resistor is 4Ω , it has $\varepsilon = 27 V$, and the relationship between strain and thickness using the mechanical calculation in [15], $\Delta h = 0.86 \Delta \varepsilon \mu m$, the reduction thickness of the test piece (Δh) was obtained with Equation (2.4).

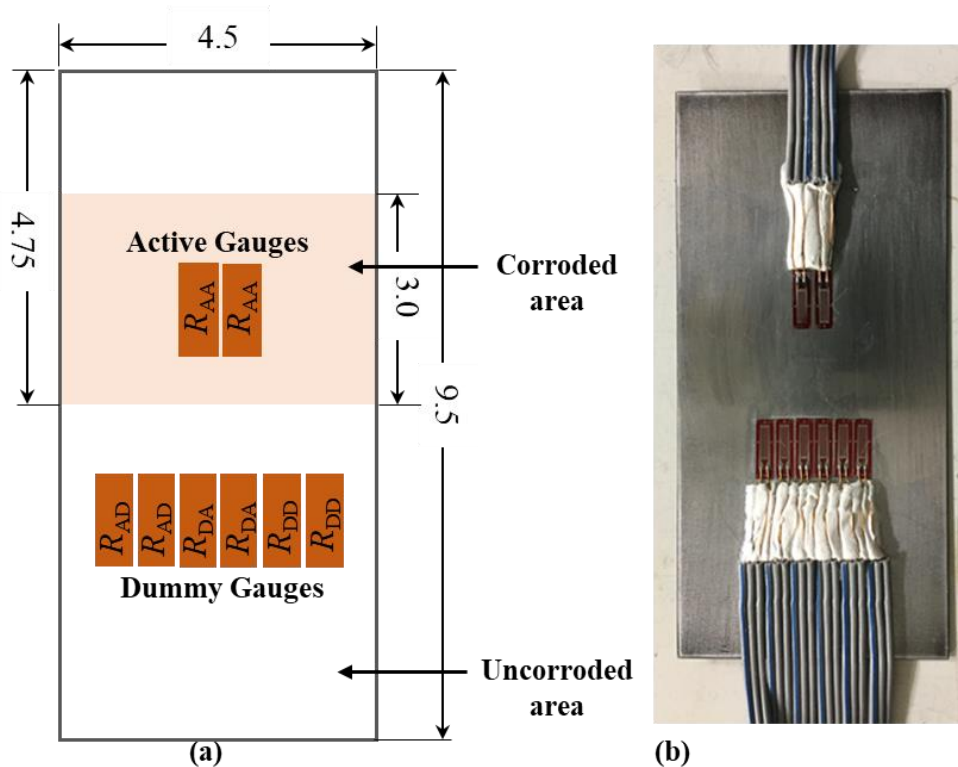


Figure 5.1 (a) Configuration of strain gauges in test piece with 1350 mm^2 corroded and the remaining area uncorroded. (b) the real picture of strain gauge attached in the test piece

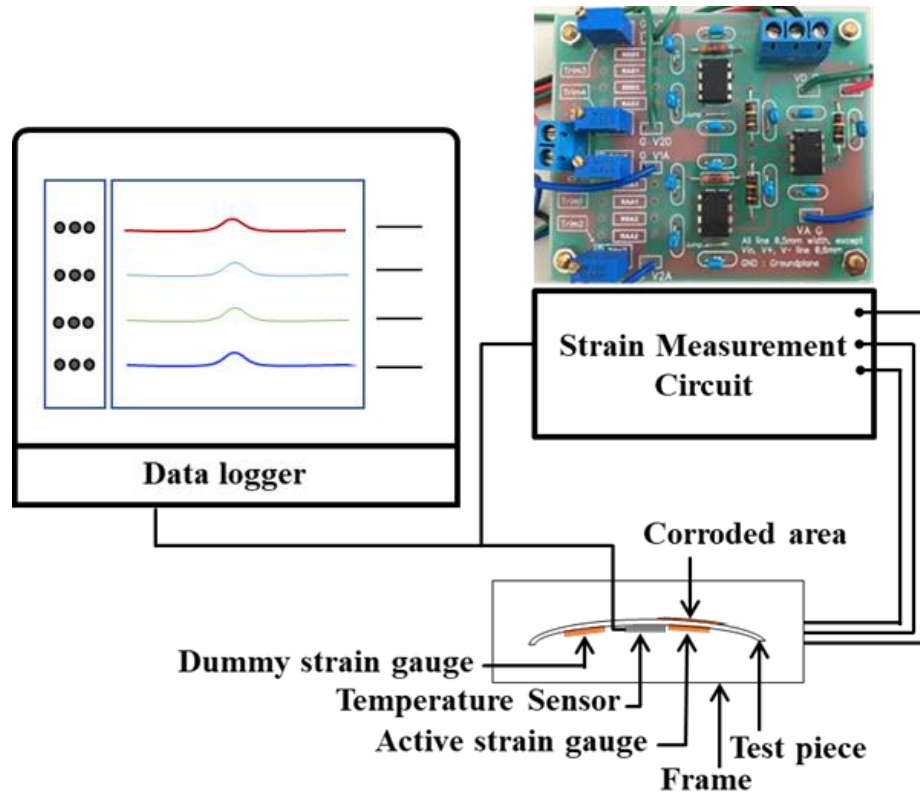


Figure 5.2 The experimental set-up of the dry-wet method for ACSSM using strain gauge

The experiment was periodically applied a 5.0 wt % NaCl solution to the test piece of the sensor under dry-wet condition. The experiment was conducted in two stages: experiment or initial experiment before spraying the salt solution to investigate the compensation of environmental factors and dry-wet condition with spraying salt solution. To discuss about thickness reduction of thickness based on the strain measurement, the several coupons of same material with test piece were prepared and they were periodically applied 5.0 wt % NaCl solution, which the same spray situation with the test piece.

5.2.2. Dry-wet Method for ACSSM Using FBG Sensor

The active FBG and dummy FBG strain sensor in this experiment used os3200 FBG sensors from Micron Optic to measure the strain. An os4200 FBG sensor was used to monitor temperature. The configuration FBGs in the test piece is shown in Figure 4. The position of the active FBG was longitudinal under the corroded area, and the dummy FBG was transversal under the uncorroded area. The corroded area was the 1350 mm² uncoating area at the surface of the test piece, the remain area was uncorroded area which covered by plastic coating and the FBGs attached in the back side of the test piece which covered by plastic coating.

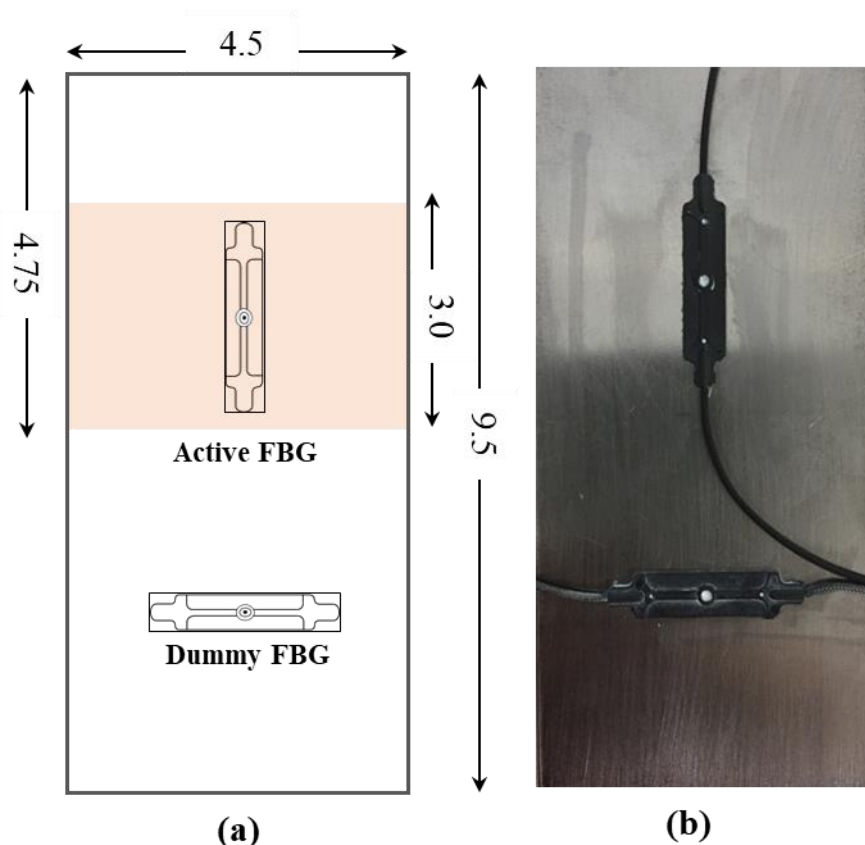


Figure 5.3 (a) Configuration of FBGs in test piece (b) the real picture of FBGs at the back side of the test piece

Figure 5.4 shows the experimental setup for dry-wet experiment using FBG sensors. This experiment proposed to investigate the effect of temperature drift to FBG strain sensor. Strain and temperature were measured with a sensing interrogator model sm125 from Micron Optics and displayed by ENLIGHT Software. The two FBGs were used as active and dummy strain sensors that obtained from Equation (9) as provided in data sheet of os3200 FBG sensor below:

$$\varepsilon = \left(\frac{\Delta\lambda}{\lambda_0 k} \right) \times 10^{-6} - \varepsilon_{T0} \quad (5.1)$$

where ε_T is the thermal output that thermally induced the apparent strain in $\mu\varepsilon$, as determined from Equation (10):

$$\varepsilon_T = \Delta T \left[\frac{C_1}{k} + CTE_S - C_2 \right] \quad (5.2)$$

From Equations (9) and (10), Equation (11) is obtained below:

$$\varepsilon = \left(\frac{\Delta\lambda}{\lambda_0 k} \right) \times 10^{-6} - \Delta T \left[\frac{C_1}{k} + CTE_S - C_2 \right] \quad (5.3)$$

where the constants $k = 0.796$, $C_1 = 6.156 \mu\text{m}/\text{m}.\text{°C}$, $C_2 = 0.7 \mu\text{m}/\text{m}.\text{°C}$ and CTE_S is thermal expansion coefficient of test piece. This experiment provided the data for dry-wet experiments for 89 days, 6 days is for initial experiment. The data sampling interval was 1 S/10 min.

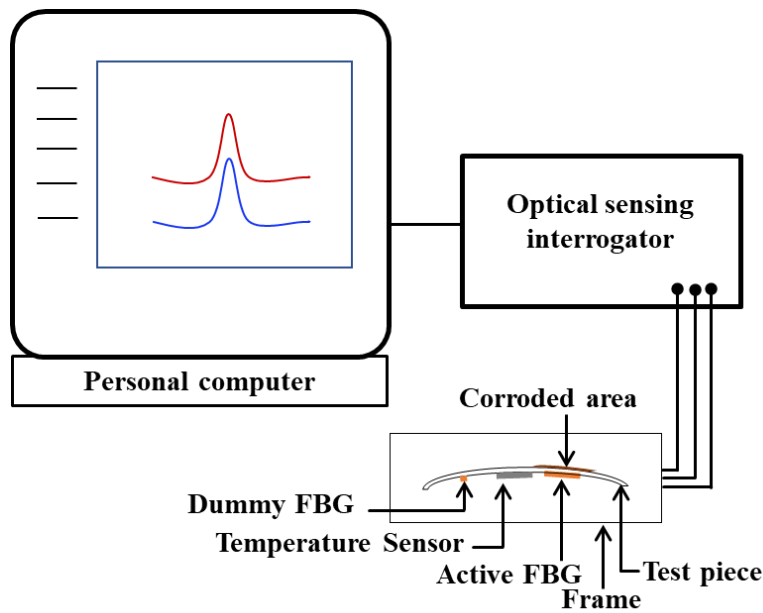


Figure 5.4 The experimental set-up of the dry-wet method for ACSSM using FBG

5.3 Result and Discussion

5.3.1 Dry-wet Experiment for ACSSM Using Strain Gauges

Figure 5.5 shows the experiment results under dry-wet condition using ACSSM for 15 days before applying salt solution. This result indicated the effect and the compensation method of environmental factors on the signal. The ε_A in the light blue line followed the temperature signal of the test piece (T_{TP}) in the red line and has a same tendency with the ε_D in the green line. T_{TP} has a range of 20°C for ε_A around $100 \mu\varepsilon$ and a drift was $5 \mu\varepsilon/^\circ\text{C}$. Although it used the active and dummy strain gauge method. Meanwhile, $\Delta\varepsilon$ in the blue line has a more constant strain in range of $25 \mu\varepsilon$, the drift of $\Delta\varepsilon$ was $1.25 \mu\varepsilon/^\circ\text{C}$. $\Delta\varepsilon$ is more constant and decreased 75% of drift of environmental factors. The ACSSM measurement system with active and dummy circuit method was

robust against environmental factors, such as temperature variation during measurement.

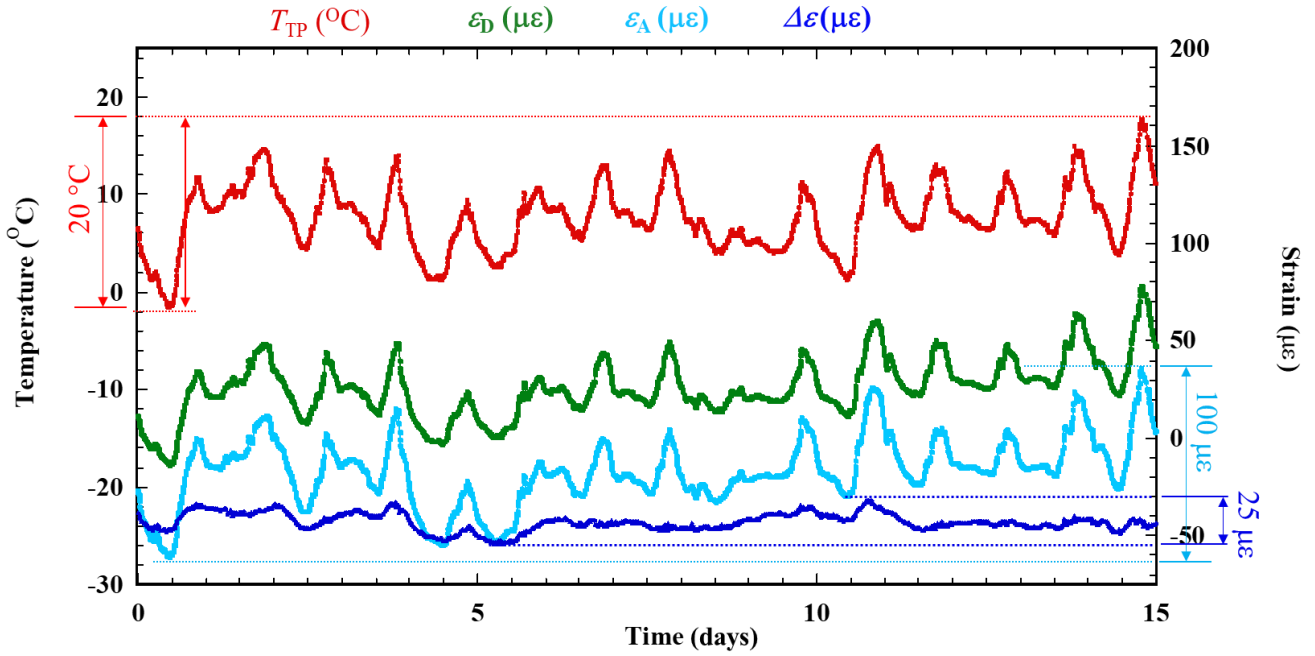


Figure. 5.5 Compensation of thermal strain experiment signal before under dry-wet condition

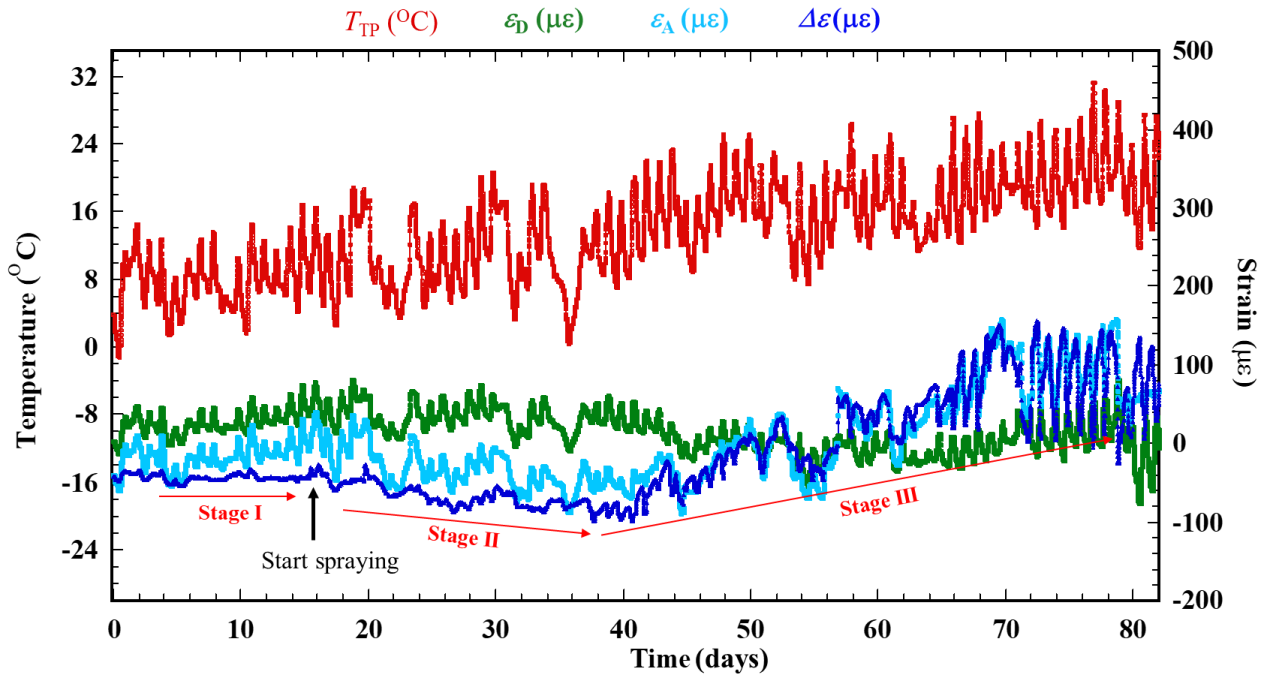


Figure 5.6 The result of a dry-wet cyclic exposure experiment with ACSSM.

Figure 5.6 shows the result of a dry–wet exposure experiment with ACSSM. There are three stages in this experiment result. Stage I is the initial condition for 15 days before spraying a salt water. This stage is the result in Figure 6. Stage II is the condition after spraying a salt water and corrosion products were generated. $\Delta\varepsilon$ shows the negative trend. It indicated that the thickness on the test piece increased due to corrosion products. Stage III is the condition of further progress of corrosion, resulting the thickness reduction due to the corrosion including corrosion product. $\Delta\varepsilon$ shows the positive trend. According to Eq. (2.4), it indicated that the thickness on the test piece decreased due to corrosion including corrosion product. As the corrosion of the test piece progressed after spraying salt solution, the variations of $\Delta\varepsilon$ became large. The reason is why as corrosion progress, two R_{AA} under corroded area and two R_{DD} under uncorroded area were different behavior, although two R_{AA} and two R_{DD} were same behavior in Stages I and II. Compared with R_{DD} , R_{AA} under corrosion product were reacted slow against temperature variation since corrosion product would have function of heat insulator. Therefore, the difference of balance of bridge circuit of the measurement system was large, resulting larger variation of $\Delta\varepsilon$.

$\Delta\varepsilon$ was converted to Δh , and Δh was applied moving average analysis using interval 200 data to get the signal more clearly without deleting tendency every stage. Moreover, Δh was moved to zero value. The result is shown in Figure 5.7. Simultaneously, the coupons test results were carried out, and the thickness reduction of the coupons calculated by the mass loss were indicated with black solid. The thickness reduction of the coupons exhibited the good correlation with the that measured with ACSSM. However, the evaluation errors between ACSSM and coupon using the average of last 4 data was 14.5 μm as shown in Table 5.1.

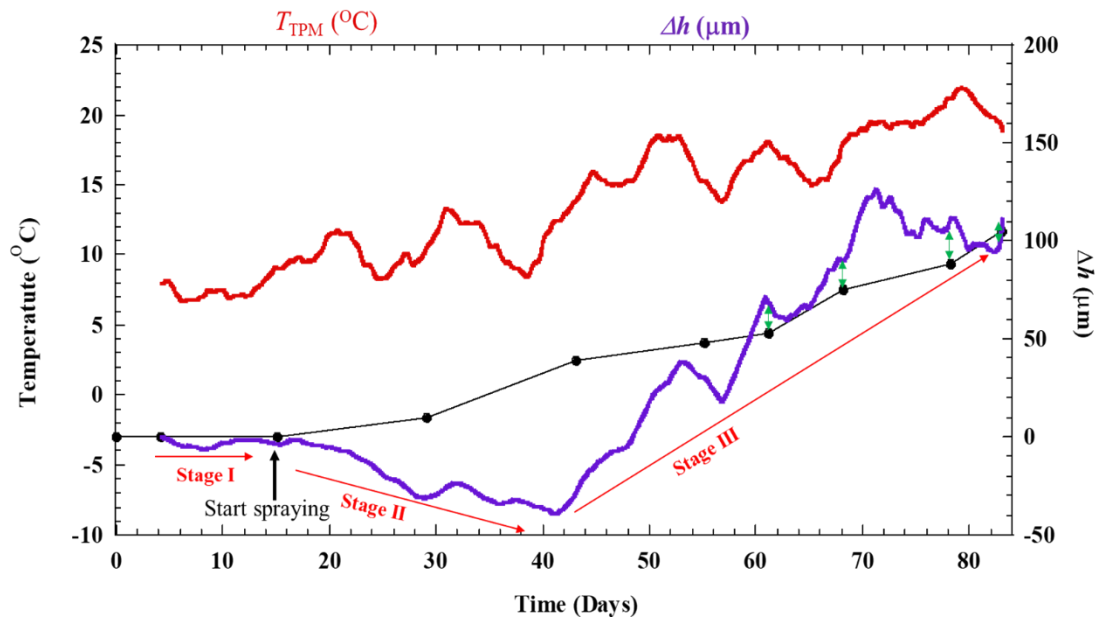


Figure 5.7 The result of under dry–wet cyclic condition with ACSSM in 83 days after moving average analysis and applied the offset value. The green line with double arrows shows the different of 4 last data between ACSSM and coupons

Table 5.1. Error calculation between ACSSM and coupon

Δh_w (μm)	Δh_{offset} (μm)	Error (μm)
54	68	14
75	90	15
88	111	23
105	111	6
Average		14.5

Figure 5.6 is the original result measurement using ACSSM with active dummy method under dry wet condition for 83 days. For getting the signal more clearly without deleting tendency every stage, the analysis using moving average is needed. Moving average method is calculation to analyze the average of any set of number. It is useful for analysis with which measuring long term trend. A moving average

calculation is based on the average value of the variable over a specific number of preceding periods. The simple calculation is using the formula as below:

$$m_{t+1} = \frac{\sum_{j=1}^n S_{t-j+1}}{n} \quad (5.4)$$

Where n is the number of periods to include in the moving average, S_j is the actual value at time j , m_j is the average value at time j . For the simple calculation,

$$\begin{aligned} m_{n+1} &= \frac{S_1 + S_2 + S_3 + \dots + S_n}{n} \\ m_{n+2} &= \frac{S_2 + S_3 + S_4 + \dots + S_n + S_{n+1}}{n} \\ m_{n+3} &= \frac{S_3 + S_4 + S_4 + \dots + S_n + S_{n+1} + S_{n+2}}{n} \\ &\vdots \\ m_k &= \frac{S_{k-n} + S_{k-n-1} + \dots + S_{k-3} + S_{k-2} + S_{k-1} + S_k}{n} \end{aligned} \quad (5.5)$$

k is the last number of set data. In this experiment result, the number of set data is 4096 data using the n is 200. The moving average value can be calculated as follow

$$\begin{aligned} m_{201} &= \frac{S_1 + S_2 + S_3 + \dots + S_{200}}{200} \\ m_{202} &= \frac{S_2 + S_3 + S_4 + \dots + S_{200} + S_{201}}{200} \\ &\vdots \\ m_{4096} &= \frac{S_{3997} + S_{3998} + \dots + S_{4091} + S_{4092} + S_{4095} + S_{4096}}{200} \end{aligned} \quad (5.6)$$

$m_{201}, m_{202}, m_{202}, \dots, m_{4095}, m_{4096}$ are the new values for representative of experiment result as shown at Figure 5.7.

Beside the moving average analysis, the FFT analysis using is presented. Figure 5.8 shows the result of $\Delta\varepsilon$ under dry–wet cyclic condition with ACSSM in 83 days after FFT analysis with removing the noise $f > 1$. The result shows the tendency is almost similar with moving average analysis without deleting the tendency each stage.

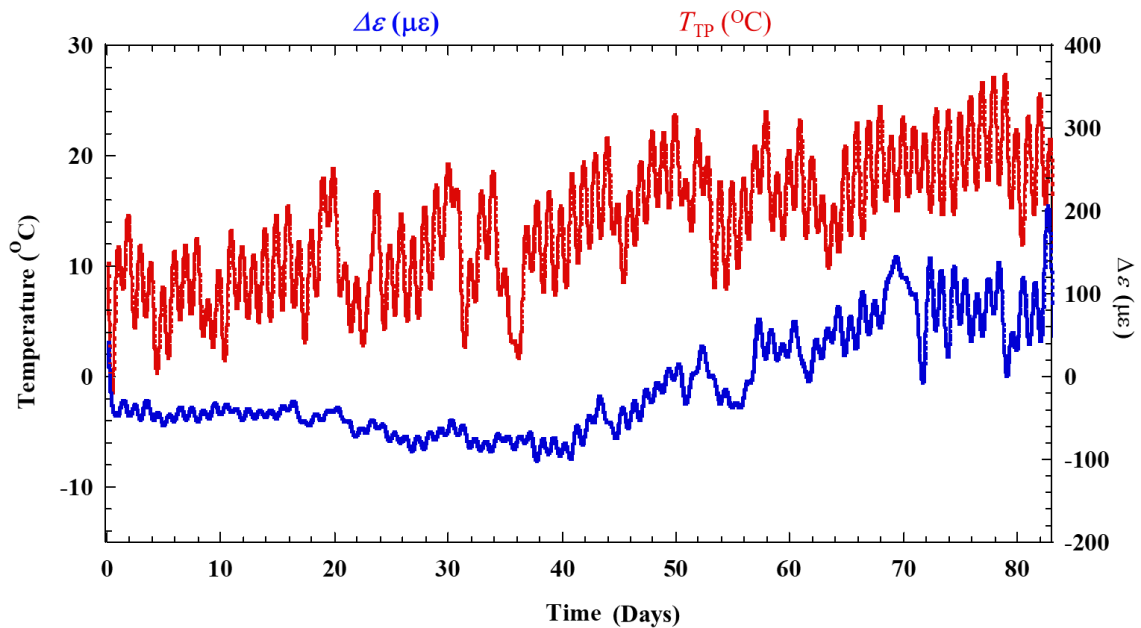


Figure 5.8 The result of under dry–wet cyclic condition with ACSSM in 83 days after FFT analysis

Figure 5.9 exhibits the pictures of evolution of the corrosion product on the test piece for 83 days. After spraying salt solution, the corrosion of the test piece progressed. These pictures were similar situation with the surface of coupon of same time. In the first day after spray, the stain from the salt water spray is shown. After 29 days, the black and brown corrosion product is appeared but not on the all surface. It happened along Stage II. In the stage III, the corrosion product was existed in all corroded area and make the porous of the test piece.

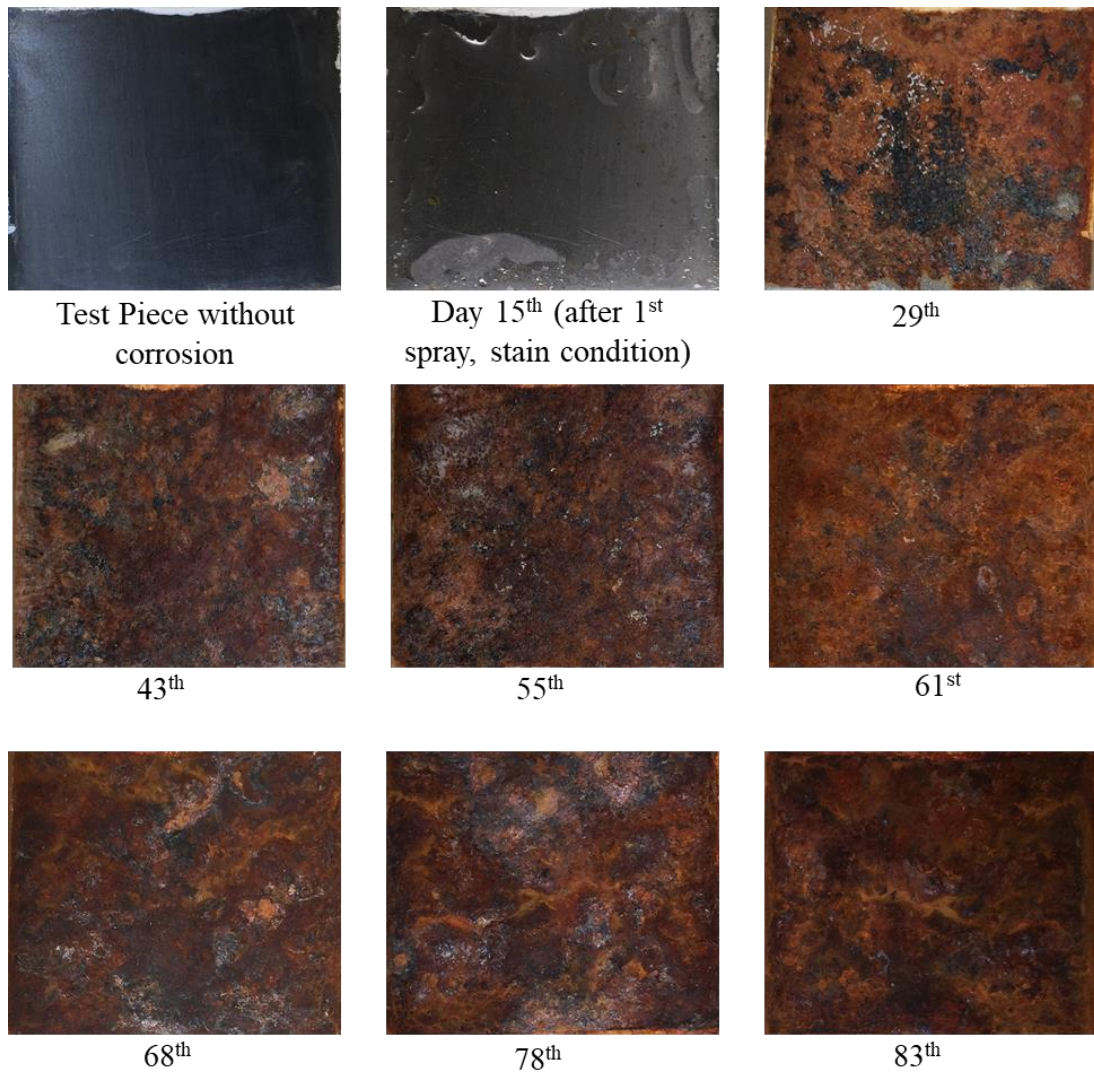


Figure 5.9 Picture of corrosion evolution for 83 days measurement. Note that there are stains due to the spray salt water in picture at Day 15th.

5.3.2 Dry-wet Experiment for ACSSM Using FBG Sensors

Figure 5.10 shows the signal pattern of compensation of thermal strain experiment using FBG sensor. Same with the experiment using strain gauges, ε_A has a same tendency with ε_D and followed T_{TP} signal. T_{TP} has a range of 4.5°C for ε_A around 60 $\mu\varepsilon$. The thermal expansion is 13 $\mu\varepsilon/^\circ\text{C}$. When it was applied $\Delta\varepsilon$ in range of 10 $\mu\varepsilon$, The

thermal expansion became $2.2 \mu\epsilon/^\circ\text{C}$. It indicated the experiment using FBG is more effective than using strain gauges, it decreased the thermal expansion until 83%.

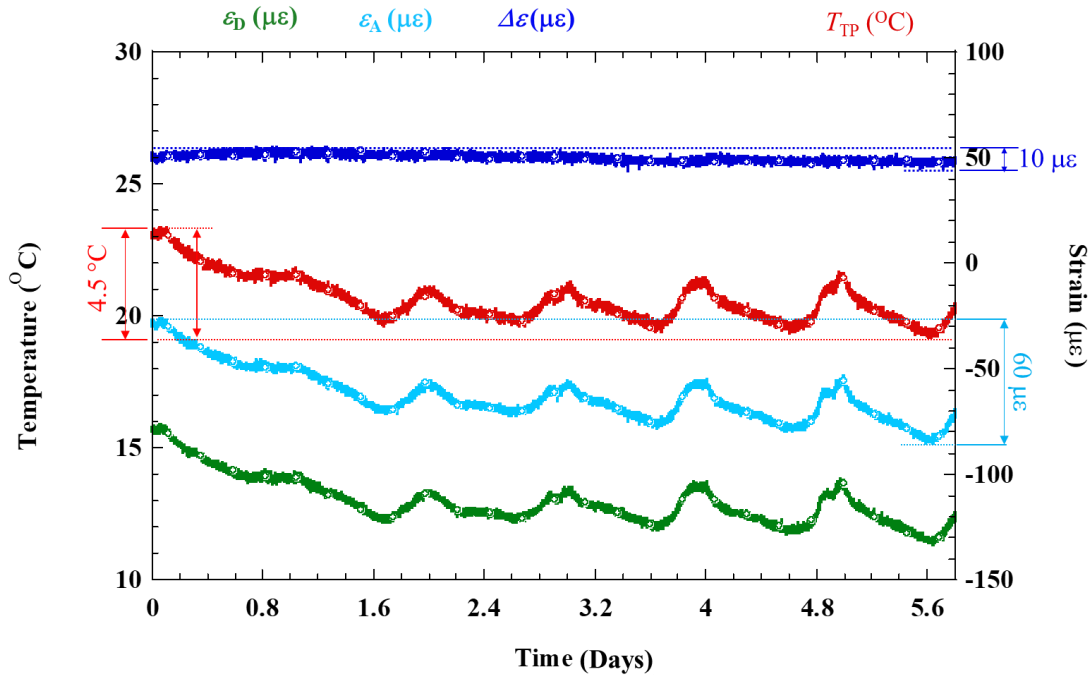


Figure 5.10. Compensation of thermal strain experiment signal before dry-wet experiment using FBG sensor

Figure 5.11 shows the variation of strain as a function of lapsed time during dry-wet experiment using FBG. Similar with experiment using strain gauges, there are three stages in this experiment result. Stage I is the initial condition around 6 days before spraying a salt water. This stage is the result in Figure 5.10. Stage II is the condition after spraying a salt water and it generated rust products. The rust thickness on the test piece increased. The graph shows the negative trend of strain. Stage III is the condition after the thickness reduction due to the corrosion including the rust product. It shows the positive trend of strain. According to Equation (2.4), the thickness reduction of the test piece due to the corrosion in compressive position of sensor, strain would be the positive trend.

Simultaneously, the coupons test results showed the strain by analyzing the mass loss and thickness loss of the coupons. The mass loss and thickness loss exhibit the good correlation with the measurement using strain gauges. The mass loss has less error than thickness loss to the experiment result.

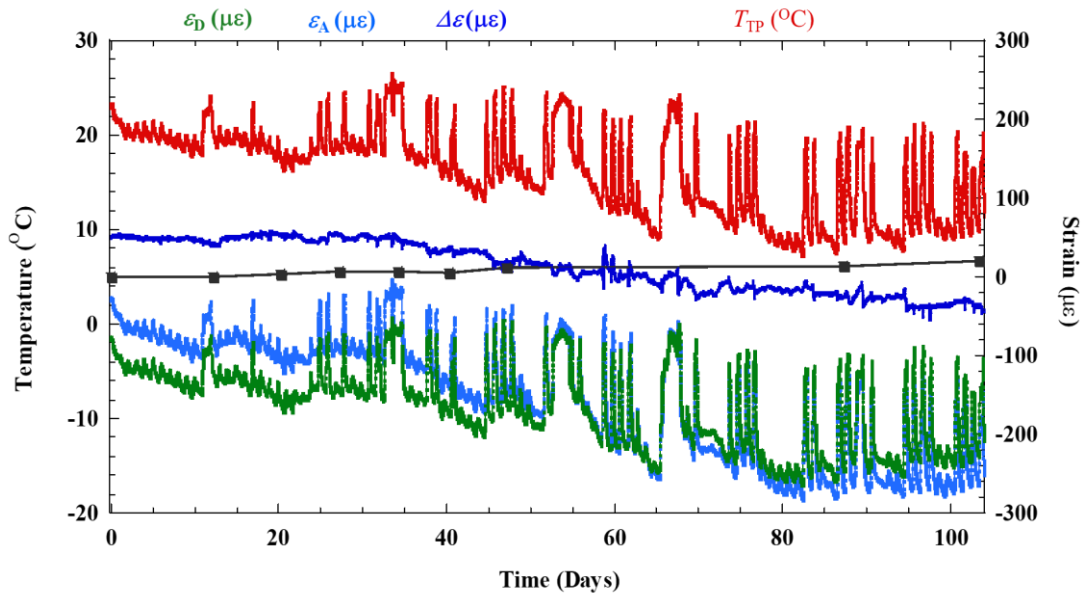


Figure 5.11 Strain signal pattern as function of elapsed time during the dry-wet experiment using FBG sensor

5.4. Mechanism of Corrosion Behavior Measured with ACSSM

Figure 5.11 shows a schematic illustration of the mechanism of corrosion behavior measured with ACSSM. Stage I is initial stage, where there is no corrosion product on the surface of the test piece, $\Delta\varepsilon$ showed the constant.

In Stage II, tight corrosion product was generated. $\Delta\varepsilon$ showed slightly decreasing tendency due to the tight corrosion product. It means thickness of the test piece would be regard as the increased thickness due to the tight corrosion product. The thickness increases of the test piece measured with ACSSM was around $50\mu\varepsilon$ for 25 days. In

stage III, corrosion of the test piece would be porous structure since corrosion progresses, and the thickness of the test piece was decreased since the porous structure of corrosion product would not receive bending moment. The thickness reduction of the test piece measured with ACSSM was around 111 μm in 43 days.

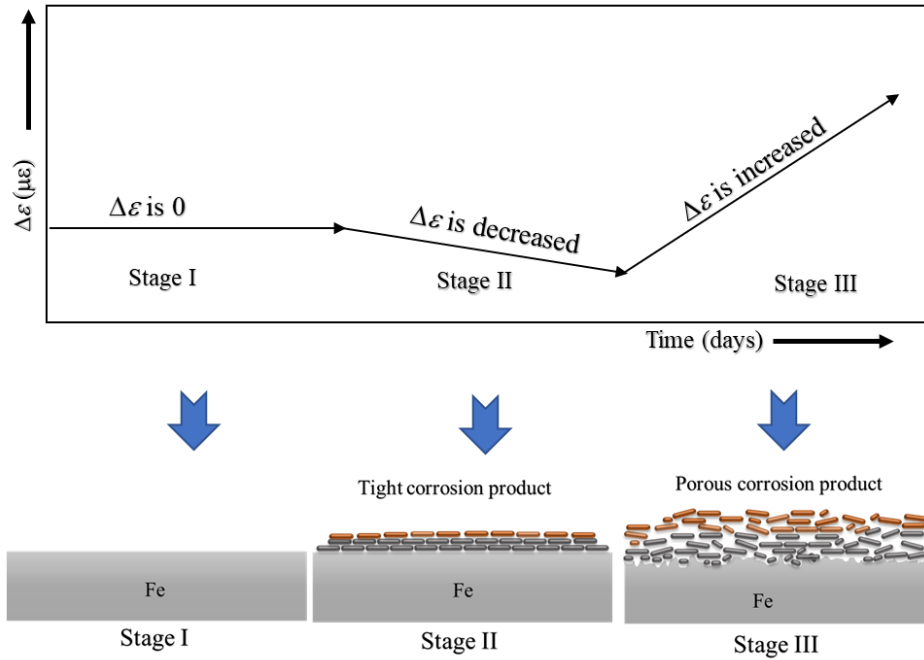


Figure 5.12 Mechanism of corrosion behavior based on strain measurement

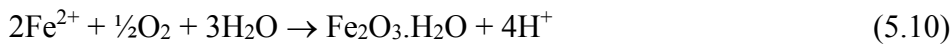
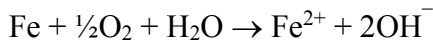
The mechanism of corrosion behavior of strain measurement by the dry wet experimental results (Figure 5.12) based on chemical reaction analysis is presented in following explanations. From the stage I as initial stage, is no rust in the surface, the strain showed the constant value even though the potential reaction between test piece (Fe) and air (O_2) appeared (Figure 5.12). The second stage, after spray the salt water ($\text{NaCl}+\text{H}_2\text{O}$), there is rust layer from the anodic reaction as following:



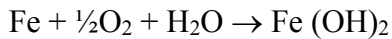
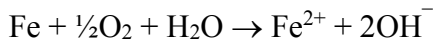
And the cathodic reaction also occurs as following:



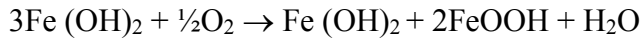
Based on these equations, generating rust layer on the surface of test piece were assumed the following reaction from Equation (5.6) and (5.8):



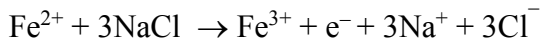
From Equation (5.6) and (5.8):



$\text{Fe}(\text{OH})_2$ reacted with the air,



The other reaction, from Equation (5.7) and (5.9)



According to Equation (5.10), (5.11) and (5.12), the thickness of rust such as Fe_2O_3 , Fe_3O_4 and FeCl_3 increased during the period of the dry-wet test and the strain shows decreased due to the rust layer without experiencing the thickness reduction of the test piece as shown in Stage II. It has a good relationship with the Equation (2.4).

The last stage, Stage III, is the further process of dry-wet experiment showed the thickness reduction due to the corrosion as result of the aging of rust because of the

concentration of chloride increased during the spray salt water periodically until 83 days. The strain increased that identified the thickness reduction occurred.

The other explanation to describe Δh behavior at a in Stage III, Figure 5.12 shows the magnification of Stage III of Figure 5.6. In addition, Figure 5.13 showed the position of active and dummy gauges in the bridge and Table 5.2 illustrated the behavior of $\Delta \varepsilon$ to indicate strain gauge behavior in Stage III.

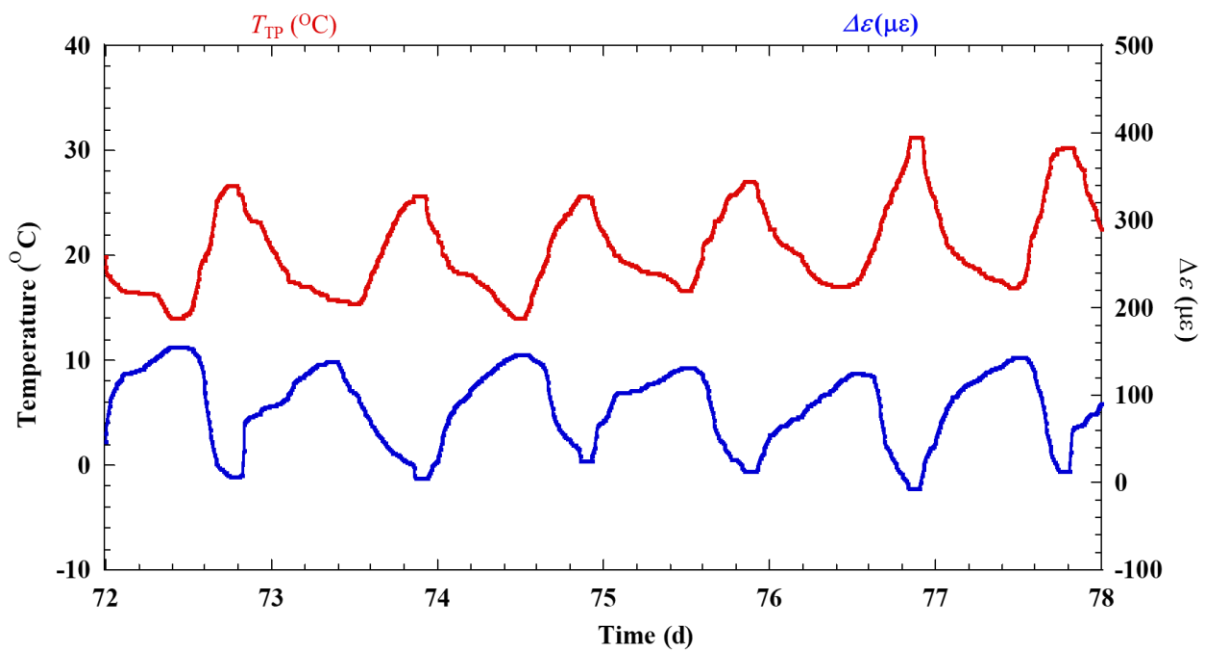


Figure 5.12 The magnification of Stage III of Figure 5.6

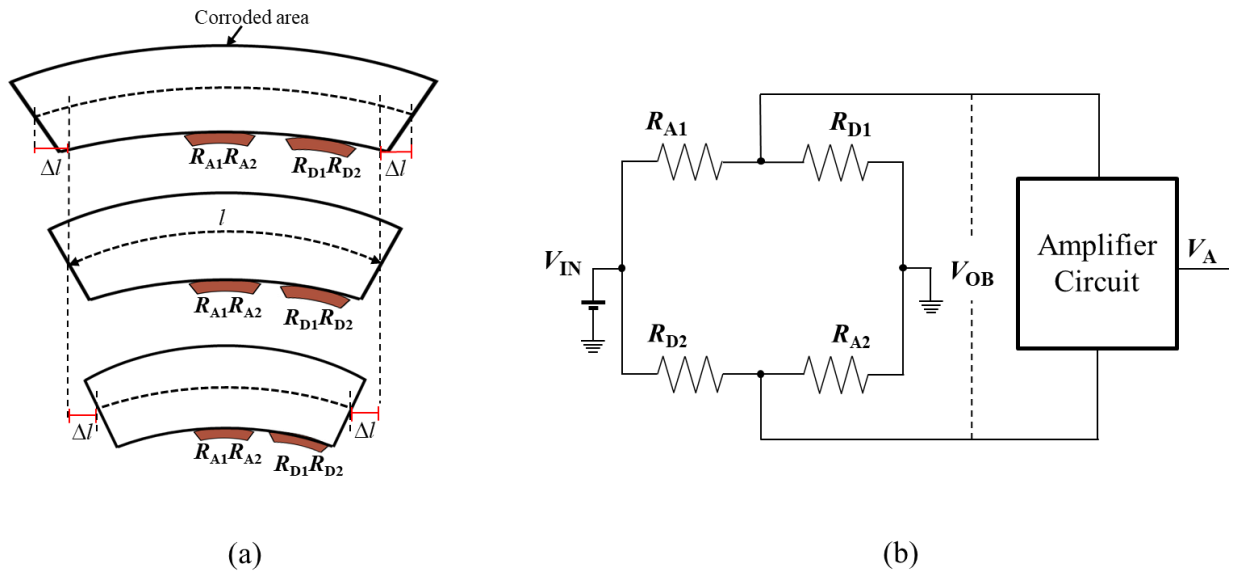


Figure 5.13 (a)The effect of active and dummy gauges position in active circuit to behavior of the test piece in strain measurement (b) position of strain gauges in the bridge circuit.

Table 5.2. Illustration of the signal behavior of $\Delta\varepsilon$ to indicate strain gauge behavior in Stage III.

Signal behavior without corrosion product			
	T_L	T_N	T_H
V_A	$R_{A1} R_{A2} < R_{D1} R_{D2}$	$R_{A1} R_{A2} = R_{D1} R_{D2}$	$R_{A1} R_{A2} > R_{D1} R_{D2}$
V_D	$R_{D1} R_{D2} = R_{D1} R_{D2}$	$R_{D1} R_{D2} = R_{D1} R_{D2}$	$R_{D1} R_{D2} = R_{D1} R_{D2}$
ΔV	$\Delta V_L < \Delta V_N$	$\Delta V_N, \text{Balance}$	$\Delta V_H > \Delta V_N$
$\Delta\varepsilon$	$\Delta\varepsilon_L < \Delta\varepsilon_N$	$\Delta\varepsilon_N, \text{Balance}$	$\Delta\varepsilon_H > \Delta\varepsilon_N$
Signal behavior with corrosion product			
	T_L	T_N	T_H
V_A	$R_{A1} R_{A2} > R_{D1} R_{D2}$	$R_{A1} R_{A2} = R_{D1} R_{D2}$	$R_{A1} R_{A2} < R_{D1} R_{D2}$
V_D	$R_{D1} R_{D2} = R_{D1} R_{D2}$	$R_{D1} R_{D2} = R_{D1} R_{D2}$	$R_{D1} R_{D2} = R_{D1} R_{D2}$
ΔV	$\Delta V_L > \Delta V_N$	$\Delta V_N, \text{Balance}$	$\Delta V_H < \Delta V_N$
$\Delta\varepsilon$	$\Delta\varepsilon_L > \Delta\varepsilon_N$	$\Delta\varepsilon_N, \text{Balance}$	$\Delta\varepsilon_H < \Delta\varepsilon_N$

In Table 5.2, $\Delta\epsilon_N$ at a temperature, which is defined as T_N in Stage III, is the value as the balance between R_{A1} and R_{A2} of the two active gauges and R_{D1} and R_{D2} of two dummy gauges at T_N . When the temperature increased from T_N , which is defined as T_H , $\Delta\epsilon$ of test piece without corrosion product, defined as $\Delta\epsilon_H$, the $\Delta\epsilon_H$ is larger than $\Delta\epsilon_N$. This tendency is same as that of Stages I and II. $\Delta\epsilon$ of test piece with corrosion product, defined as $\Delta\epsilon_H$, is smaller than $\Delta\epsilon_N$. The reason why as corrosion progress, R_{A1} and R_{A2} under corroded area and R_{D1} and R_{D2} under uncorroded area were different behavior, although two active strain gauges are under corroded area and two dummy strain gauges under uncorroded area were same behavior in Stages I and II. The thermal expansion of test piece was cancelled due to two active and two dummy gauges method. Compared with R_{D1} and R_{D2} of dummy gauges, R_{A1} and R_{A2} of active strain gauges under corrosion product were reacted slow against increased temperature since corrosion product would have function of heat insulator. Therefore, $\Delta\epsilon_H$ is increased as the opposite balance value between the two active gauges and two dummy gauges when the temperature increased.

When the temperature decreased from T_N , which is defined as T_L , $\Delta\epsilon$ of test piece without corrosion product, defined as $\Delta\epsilon_L$, the $\Delta\epsilon_L$ is smaller than $\Delta\epsilon_N$. This tendency is same as that of Stages I and II. $\Delta\epsilon$ of test piece with corrosion product, defined as $\Delta\epsilon_L$, is larger than $\Delta\epsilon_N$. The reason why as corrosion progress, R_{A1} and R_{A2} under corrosion product were reacted slow against decreased temperature since corrosion product would have function of heat insulator. The thermal expansion of test piece was cancelled due to two active and two dummy method. Therefore, $\Delta\epsilon_L$ is increased as the balance value between the R_{A1} and R_{A2} and R_{D1} and R_{D2} when the temperature increased.

5.4 Summary

An ACSSM with an active dummy method, which was proposed by authors, was used for experiment with dry-wet method in long term monitoring condition. The conclusions of this study are as follows,

1. The investigation of corrosion product behavior was conducted using strain gauges under dry-wet condition. The result consists of three stages.
2. In Stage I of the experiment using strain gauges, $\Delta\varepsilon$ was the relative constant signal, improving from $5\mu\varepsilon/^\circ\text{C}$ to $1.25\mu\varepsilon/^\circ\text{C}$ against temperature variation.
3. In Stage II, $\Delta\varepsilon$ showed negative trend, resulting the increased thickness of the test piece of ACSSM. It would be due to tight corrosion product on the test piece of ACSSM.
4. In Stage III, $\Delta\varepsilon$ showed positive trend since corrosion product would be porous. Accuracy of Δh was from the thickness reduction of the coupons. It can be used for ACSSM to determine the atmospheric corrosion monitoring in the actual field.
5. To explain the behavior in Stage III, mechanism corrosion is needed.
6. In Stage I of the experiment using FBG sensors, $\Delta\varepsilon$ was the relative constant signal, improving from $13\mu\varepsilon/^\circ\text{C}$ to $2.2\mu\varepsilon/^\circ\text{C}$ against temperature variation.
7. The experiment is still on going in Stage II.

Chapter 6

CONCLUSION

6.1. Conclusion

ACSSM with an active dummy method was designed for monitoring corrosion in galvanostatic electrolysis test and under dry-wet condition to investigate the corrosion product in long term monitoring condition. The conclusions of this study are:

1. By indicating the all elements content in this chapter, we can make the fundamental method for measuring the atmospheric corrosion based on strain measurement using strain gauge and FBG sensor
2. The design of the ACSSM using active dummy method can compensate the environmental effect especially the temperature effect which has a large effect on strain measurement. Several test and simulation were conducted in designing of ACSSM.
3. The achievement of accuracy of ACSSM using strain gauge and FBG sensors can be described by graph in Figure 6.1. The accuracy based on temperature effect of ACSSM using strain gauges can be achieved with active dummy circuit configuration, meanwhile using the FBG sensor can be achieve only using the FBG sensors configuration.

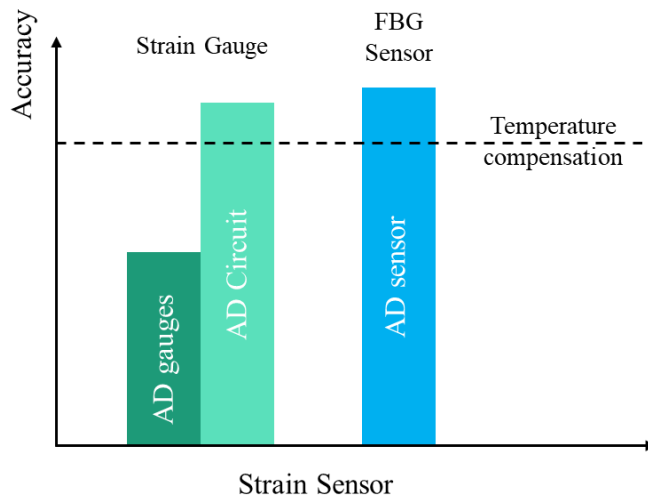


Figure 6.1 The achievement of accuracy of ACSSM using strain gauge and FBG sensors

4. In the accelerated laboratory test by Galvanostatic electrolysis using strain gauges and FBG sensors have good correlation between analytical results determined using the mechanical properties of materials and FEA. This correlation indicates that the principle of atmospheric corrosion sensors is reasonable. The signal showed positive trend of strain (tensile).
5. Comparing the results with experiment for ACSSM using strain gauge which has error 12% and using FBG sensor which has error 7.5%. As we predicted, the results with FBG were accurate, high resolution and stable because the FBG only has sensor temperature dependence. Meanwhile, ACSSM using strain gauge has temperature dependence of amplifier circuit and sensor itself. It meant the accuracy of using FBG sensor is higher than the using strain gauges.
6. The investigation of corrosion product behavior was conducted using strain gauges under dry-wet condition. The result consists of three stages. In Stage I of the experiment using strain gauges, $\Delta\epsilon$ was the relative constant signal. Stage II, $\Delta\epsilon$ showed negative trend, resulting the increased thickness of the test piece of

ACSSM. Stage III, $\Delta\varepsilon$ showed positive trend since corrosion product would be porous. Accuracy of Δh was from the thickness reduction of the coupons.

7. The investigation of corrosion product behavior by ACSSM using FBG sensors under dry-wet condition is conducting. The result for Stage I was conducted. It was similar with experiment using strain gauge, $\Delta\varepsilon$ was the relative constant signal. Stage II, $\Delta\varepsilon$ showed negative trend, and it is still conducting now.
8. From the result in Stage I, the experiment using FBG sensors has higher accuracy than using strain gauges. It is because of the basic parameter that measured the strain of FBG sensor for strain measurement is different from using strain gauge. FBG measures the wavelength to get the strain that not directly measure the amplitude of the signal, but the shifter of the wavelength. In this case the FBG wavelength always measure the peak of the signal. While the strain gauge measures the resistance that is directly measure the amplitude of the signal.

6.2. Future Research and Recommendation

Future studies are expected to explore the atmospheric corrosion in the field in the different place to determine the corrosion rate in the field. To develop the circuit of ACSSM using strain gauges for field application, the strengthen and durability test is needed.

References

- A. M. Monsada, T. Margarito, L. C. Milo, E. P. Casa, J. V. Zabala, A. S. Maglines, B. A. Basilia, S. Harada, T. Shinohara, Atmospheric corrosion exposure study of the Philippine historical all-steel Basilica, *Zair. Kankyo C-107* (2016) 267–270.
- Araceli M. Monsada, Marianito T. Margarito, Lumen C. milo, Edmar P. Casa, Juan V. Zabala, Angelito S. Maglines, Blessie A. Basilia, Shun-ichi Harada, Tadashi Shinohara, 2016, Atmospheric corrosion exposure study of The Philippine Historical all steel Basilica, *Zairyō to Kankyo* 2016, C-107, pp. 267-270.
- C. Chiavari, E. Bernardi, A. Balbo, C. Monticelli, S. Raffo, M.C. Bignozzi, C. Martini, Atmospheric corrosion of fire-gilded bronze: Corrosion and corrosion protection during accelerated ageing tests, *Corros. Sci.* 100 (2015) 435–447. doi:10.1016/j.corsci.2015.08.013.
- C. H. Tan, F. R. Mahamd Adikan, Y. G. Shee, and B. K. Yap, “Non-destructive fiber Bragg grating based sensing system: Early corrosion detection for structural health monitoring,” *Sensors Actuators, A Phys.*, vol. 268, pp. 61–67, 2017.
- C. Li, Y. Ma, Y. Li, F. Wang, EIS monitoring study of atmospheric corrosion under variable relative humidity, *Corros. Sci.* 52 (2010) 3677–3686. doi:10.1016/j.corsci.2010.07.018.
- C. Rodrigues, F. Cavadas, C. Félix, and J. Figueiras, “FBG based strain monitoring in the rehabilitation of a centenary metallic bridge,” *Eng. Struct.*, vol. 44, pp. 281–290, 2012.
- C. Thee, J. Dong, W. Ke, Corrosion monitoring of weathering steel in a simulated coastal-industrial environment, *Int. J. Environ. Chem. Ecol. Eng.* 9 (2015) 587–593.
- C.H. Tan, F.R. M. Adikan, Y.G. Shee, B.K. Yap, Non-destructive fiber Bragg grating based sensing system: Early corrosion detection for structural health monitoring, *Sensors Actuators, A Phys.* 268 (2017) 61–67. doi:10.1016/j.sna.2017.10.048.
- Cai J. P. and Lyon S. B., 2005, A mechanistic study of initial atmospheric corrosion kinetics using electrical resistance sensor, *Corrosion Science*, Vol. 47, pp. 2956–2973.

- Cruz R. P. V., Nishikata A. and Tsuru T., 1996, AC impedance monitoring of pitting corrosion of stainless steel under a wet–dry cyclic condition in chloride-containing environment, *Corrosion Science*, Vol. 38, pp. 1397–1406.
- E.D. Kiosidou, A. Karantonis, G.N. Sakalis, D.I. Pantelis, Electrochemical impedance spectroscopy of scribed coated steel after salt spray testing, *Corros. Sci.* 137 (2018) 127–150. doi:10.1016/j.corsci.2018.03.037.
- Ekkarut Viyanit, Wanida Pongsaksawad, Sikharin Sorachot, Hiroyuki Matsuyama, Nozomu Fukuda, 2016, Investigation of atmospheric corrosion behavior of austenitic and ferritic stain less steel welds under tropical climate of Thailand, *Zairyo to Kankyo* 2016, C-109, pp. 275-279.
- El-Mahdy G. A., Nishikata A. and Tsuru T., 2000, Electrochemical corrosion monitoring of galvanized steel under cyclic wet–dry conditions *Corrosion Science*, Vol. 42, pp. 183–194.
- El-Mahdy G.A., Nishikata A. and Tsuru T., 2000, AC impedance study on corrosion of 55% Al–Zn alloy-coated steel under thin electrolyte layers, *Corrosion Science*, Vol. 42, pp. 1509–1521.
- F. Mansfeld, S. L. Jeanjaquet, M. W. Kendig and Roe D. K., A new atmospheric corrosion rate monitor development and evaluation, *Atmos. Environ.* 20 (1986) 1179–1192. doi:10.1016/0004-6981(86)90152-6
- G.A. El-Mahdy, Atmospheric corrosion of copper under wet / dry cyclic conditions, *Corro.Sci.* 47 (2005) 1370–1383. doi:10.1016/j.corsci.2004.07.034.
- H. lin Liu, Z. wei Zhu, Y. Zheng, B. Liu, and F. Xiao, “Experimental study on an FBG strain sensor,” *Opt. Fiber Technol.*, vol. 40, no. April 2017, pp. 144–151, 2018.
- H. Murayama, K. Ohara, N. Kanata, K. Kageyama, and H. Igawa, “Strain Monitoring and Defect Detection in Welded Joints by Using Fiber-Optic Distributed Sensors with High Spatial Resolution,” *Society*, vol. 2, pp. 191–199, 2011.
- H. N. Li, L. Ren, D. S. Li, and T. H. Yi, “Design and applications of fiber Bragg grating sensors for structural health monitoring,” *Adv. Struct. Eng. Mech.*, pp. 2215–2221, 2013.

- H. Zhang, R. Yang, Y. He, G. Y. Tian, L. Xu. R. Wu, Identification and characterization of steel corrosion using passive high frequency RFID sensors, *Measurement*. 92 (2016) 421–427. doi:10.1016/j.measurement.2016.06.041
- H.W. Song, V. Saraswathy, Corrosion monitoring of reinforced concrete structures - A review, *Int. J. Electrochem. Sci.* 2 (2007) 1–28. doi:10.1504/Ijplm.2007.012871.
- Hong Zhang, Ruizhen Yang, Yunze He, Gui Yun Tian, Luxiong Xu, Ruikun Wu, 2016, Identification and characterization of steel corrosion using passive high frequency RFID sensors, *Measurement*, Vol 92, pp. 421–427.
- I. Shitanda, A. Okumura, M. Itagaki, K. Watanabe, Y. Asano, Screen printed atmospheric corrosion monitoring sensor based on electrochemical impedance spectroscopy, *Sensors Actuators, B Chem.* 139 (2009) 292–297. doi:10.1016/j.snb.2009.03.027.
- J. Luo, Corrosion of the galvanized steel bolts of overhead catenary system in the tunnel areas, *Proc. of JSCE Mater Environ.* 2016 (2016) 293–297.
- J. Zhang, G. Y. Tian, A. M. J. Marindra, A. I. Sunny, A. B. Zhao, A review of passive RFID tag antenna-based sensors and systems for structural health monitoring applications, *Sensors*. 17 (2017) 1–33. doi:10.3390/s17020265
- Jun Hua Dong, Wenjuan Chen, Wei Ke, 2016, Corrosion evolution of steel simulated of SO₂ polluted coastal atmospheres, *Zairyo to Kankyo* 2016, C-112, pp. 289-292.
- K. Al Handawi, N. Vahdati, P. Rostron, L. Lawand, O. Shiryayev, Strain based FBG sensor for real-time corrosion rate monitoring in pre-stressed structures, *Sensors Actuators, B Chem.* 236 (2016) 276–285. doi:10.1016/j.snb.2016.05.167.
- K. Hoffmann, *An Introduction to Stress Analysis and Transducer Design using Strain Gauges* The definitive work on strain gauge measurement, (2009). www.hbm.com.
- K. Hoffmann, *Applying the wheatstone bridge circuit*, W1569-1.0en, HBM
- K. Perveen, G.E. Bridges, S. Bhadra, D.J. Thomson, Corrosion potential sensor for remote monitoring of civil structure based on printed circuit board sensor, *IEEE Trans. Instrum. Meas.* 63 (2014) 2422–2431. doi:10.1109/TIM.2014.2310092.

- Khalil Al Handawi, Nader Vahdati, Paul Rostron, Lydia Lawand, Oleg Shirayayev, 2016, Strain based FBG sensor for real-time corrosion rate monitoring in pre-stressed structures, *Sensor and Actuator B* 236(2016), pp 276-285.
- Le Thi Hong Lien, Hoang Lam Hong, Pham Thi San, Nguyen Trung Hieu, Nguyen Thi Thanh Nga, 2016, Atmospheric corrosion of carbon steel and weathering steel - relation of corrosion and environmental factors, *Zairyo to Kankyo* 2016, C-110, pp. 280-284.
- Li C., Ma Y., Li Y. and Wang F., 2010, EIS monitoring study of atmospheric corrosion under variable relative, *Corrosion Science*, Vol. 52 3677–3386.
- Li S., Kim Y. G., Jung S., Song H. S. and Lee S. M., 2007, Application of steel thin film electrical resistance sensor for in situ corrosion monitoring, *Sensors Actuators*, Vol. B 120, pp. 368–377.
- Lin AN, Ryosuke Saito, Satoshi Takaya, Toyoaki Miyagawa, Determination of Young's Modulus of rust-layer by bending experiment, 2013, *JCI Annual Proceeding*, Vol. 35, No.1, pp 1117-1122.
- M. Alamin, G.Y. Tian, A. Andrews, P. Jackson, Corrosion detection using low-frequency RFID technology, *Insight-Non-Destructive Test. Cond. Monit.* 54 (2), 72-75. doi:10.1784/insi.2012.54.2.72
- M. C. Emmons, S. Karnani, S. Trono, K. P. Mohanchandra, W. L. Richards, and G. P. Carman, "Strain measurement validation of embedded fiber bragg gratings," *Int. J. Optomechatronics*, vol. 4, no. 1, pp. 22–33, 2010.
- M. Kreuzer, Strain measurement with fiber bragg grating sensors, HBM, Darmstadt, S2338-1.0 E. (2006). doi:10.1097/ACO.0b013e3282fe6e70
- M. Morcillo, D. De Fuente, I.Diaz., H. Cano, Atmospheric corrosion of mild steel, *Rev. Metal. (Madrid, Spain)* 47 (2011) 426–444. doi:10.3989/revmetalm.1125.
- M. R. A. Hassan, M. H. A. Bakar, K. Dambul, and F. R. M. Adikan, "Optical-based sensors for monitoring corrosion of reinforcement rebar via an etched Cladding Bragg grating," *Sensors (Switzerland)*, vol. 12, no. 11, pp. 15820–15826, 2012.
- M. Ridha, S. Fonna, S. Huzni, J. Supardi, A.K.A.M. Ihsan, Atmospheric corrosion of structural steels exposed in the 2004 tsunami-affected areas of Aceh, *Int. J. Automot. Mech. Eng.* 7 (2013) 1014–1022. doi:10.15282/ijame.7.2012.17.0082.

- M. Yasri, F. Gallee, B. Lescop, E. Diler, D. Thierry, S. Rioual, Passive Wireless Sensor for atmospheric corrosion monitoring, (2014) 2945–2949. The 8th European Conference on Antennas and Propagation (EuCAP 2014).
- M. Yu, H. Zu, K. Zhao, J. Liu, S. Li, Effects of dry / wet ratio and pre-immersion on stress corrosion cracking of 7050-T7451 aluminum alloy under wet-dry cyclic conditions, Chinese J. Aeronaut. 31 (2018) 2176–2184. doi:10.1016/j.cja.2018.01.008
- M.F. Stroosnijder, C. Brugnoli, G. Laguzzi, L. Luvidi, N. De Cristofaro, Atmospheric corrosion evaluation of galvanised steel by thin layer activation, Corros. Sci. 46 (2004) 2355–2359. doi:10.1016/j.corsci.2004.01.014.
- M.O.G. Portella, K.F. Portella, P.A.M. Pereira, P.C. Inone, K.J.C. Brambilla, M.S. Cabussú, D.P. Cerqueira, R.N. Salles, Atmospheric corrosion rates of copper, galvanized steel, carbon steel and aluminum in the metropolitan region of Salvador, BA, Northeast Brazil, Proc. Eng. 42 (2012) 171–185. doi:10.1016/j.proeng.2012.07.408.
- M.R.A. Hassan, M.H.A. Bakar, K. Dambul, F.R.M. Adikan, Optical-based sensors for monitoring corrosion of reinforcement rebar via an etched cladding Bragg grating, Sensors (Basel). 12 (2012) 15820–15826. doi:10.3390/s121115820.
- Mansfeld F. and Kenkel J. V., 1976, Electrochemical monitoring of atmospheric corrosion phenomena, Corrosion Science, Vol 16, pp. 111–112.
- Mansfeld F. and Tsai S., 1980, Laboratory studies of atmospheric corrosion—I. Weight loss and electrochemical measurements, Corrosion Science, Vol 20, pp. 853–872.
- Mansfeld F., Jeanjaquet S. L., Kendig M. W. and Roe D. K., 1986, A new atmospheric corrosion rate monitor development and evaluation, Atmos. Environ., Vol. 20, pp. 1179–1192.
- Maria Yasri, Francois Gallee, Benoit Lescop, Erwan Diler, Dominique Thierry, Stephane Rioual, 2014, Passive wireless sensor for atmospheric corrosion monitoring, The 8th European Conference on Antennas and Propagation (EuCAP 2014), IEEE, pp 2945-2949.

- N. Kasai, K. Utatsu, S. Park, S. Kitsukawa, K. Sekine, Correlation between corrosion rate and AE signal in an acidic environment for mild steel, *Corros. Sci.* 51 (2009) 1679–1684. doi:10.1016/j.corsci.2009.04.021.
- N. Kasai, M. Hiroki, T. Yamada, H. Kihira, K. Matsuoka, Y. Kuriyama, S. Okazaki, Atmospheric corrosion sensor based on strain measurement, *Meas. Sci. Technol.* 28 (2016) 015106. doi:10.1088/1361-6501/aa4f20
- N. Palsson, P. Khamsuk, S. Sorachot, W. Khonraeng, K. Wongpinkaw, Atmospheric corrosion of structural steels in Thailand tropical climate, *Zair. Kankyo C-108* (2016) 271–274.
- N. Purwasih, N. Kasai, S. Okazaki, H. Kihira, Development of amplifier circuit by active dummy method for atmospheric corrosion monitoring on steel, *Metals* 8 (2018) 1–12. doi:10.3390/met8010005
- N. Zhang, W. Chen, X. Zheng, W. Hu, M. Gao, Optical sensor for steel corrosion monitoring based on etched fiber Bragg grating sputtered with iron film, *IEEE Sens. J.* 15 (2015) 3551–3556. doi:10.1109/JSEN.2015.2393559.
- Naoya Kasai, Kentaro Utatsu, Sosoon Park, Shigeo Kitsukawa, Kazuyoshi Sekine (Japan), 2009, Correlation between corrosion rate and AE signal in an acidic environment for mild steel, *Corrosion Science*, Vol. 51, pp 1679-1684.
- Nishikata A., Suzuki F. and Tsuru T., 2005, Corrosion monitoring of nickel-containing steels in marine atmospheric environment, *Corrosion Science*, Vol. 47, pp. 2578–2588.
- Nishikata A., Yamashita Y., Katayama H., Tsuru T., Usami A., Tanabe K. and Mabuchi H., 1995, An electrochemical impedance study on atmospheric corrosion of steels in a cyclic wet–dry condition, *Corrosion Science*, Vol. 37, pp. 2059–2069.
- O. Almubaied, H.K. Chai, M.R. Islam, K.S. Lim, C.G. Tan, Monitoring Corrosion Process of Reinforced concrete structure using FBG strain sensor, *IEEE Trans. Instrum. Meas.* 66 (2017) 2148–2155. doi:10.1109/TIM.2017.2676218.
- P. Dillmann, F. Mazaudier, S. Hoerle, Advances in understanding atmospheric corrosion of iron . I . Rust characterisation of ancient ferrous artefacts exposed to indoor atmospheric corrosion, *Corros. Sci.* 46 (2004) 1401–1429. doi:10.1016/j.corsci.2003.09.027.

- S. Ahmad, Reinforcement corrosion in concrete structures, its monitoring and service life prediction - A review, *Cem. Concr. Compos.* 25 (2003) 459–471. doi:10.1016/S0958-9465(02)00086-0.
- S. K. T. Grattan, S. E. Taylor, P. A. M. Basheer, T. Sun, and K. T. V. Grattan, “Monitoring of Corrosion in Structural Reinforcing Bars: Performance Comparison Using In Situ Fiber-Optic and Electric Wire Strain Gauge Systems,” *IEEE Sens. J.*, vol. 9, no. 11, pp. 1494–1502, 2009.
- Shitanda I., Okumura A., Itagaki M., Watanabe K. and Asano Y., 2009, Screen-printed atmospheric corrosion monitoring sensor based on electrochemical impedance spectroscopy, *Sensors Actuators, Vol. B* 139, pp. 292–297.
- T. Shinohara, A. Tahara and T. Dara, Atmospheric corrosion behaviours of steels in Japan, *Zair. Kankyo. C-111* (2016) 285–288.
- To Dara, T. Shinohara, O. Umezawa, 2016, The Behavior of corrosion of low carbon steel affected by corrosion product and Na₂SO₄ concentration under artificial rainfall test, *Zairyo to Kankyo* 2016, C-114, pp. 298-302.
- W. Chen, X. Dong, Modification of the wavelength-strain coefficient of FBG for the prediction of steel bar corrosion embedded in concrete, *Opt. Fiber Technol.* 18 (2012) 47–50. doi:10.1016/j.yofte.2011.11.004.
- W. Hu, H. Cai, M. Yang, X. Tong, C. Zhou, W. Chen, Fe-C-coated fibre Bragg grating sensor for steel corrosion monitoring, *Corros. Sci.* 53 (2011) 1933–1938. doi:10.1016/j.corsci.2011.02.012.
- W. Hu, L. Ding, C. Zhu, D. Guo, Y. Yuan, N. Ma, W. Chen, Optical fiber polarizer with Fe-C film for corrosion monitoring, *IEEE Sens. J.* 17 (2017) 6904–6910. doi:10.1109/JSEN.2017.2743245.
- W. Ke, J. H. Dong, W. Chen, Corrosion evolution of steel simulated of SO₂ polluted coastal atmospheres, *Zair. Kankyo. C-112* (2016) 289–292.
- Wenbin Hu, Hanli Cai, Minghong Yang, Xinglin Tong, Ciming Zhou, Wei Chen, 2011, Fe–C-coated fibre Bragg grating sensor for steel corrosion monitoring, *Corrosion Science* 53 (2011), pp 1933-1938.
- X. Wen, P. Bai, B. Luo, S. Zheng, C. Chen, Review of recent progress in the study of corrosion products of steels in a hydrogen sulphide environment, *Corros. Sci.* 139 (2018) 124–140. doi:10.1016/j.corsci.2018.05.002.

- Y. Abbas, J.S. Nutma, W. Olthuis, A. Van Den Berg, Corrosion monitoring of reinforcement steel using galvanostatically induced potential transients, *IEEE Sens. J.* 16 (2016) 693–698. doi:10.1109/JSEN.2015.2485667.
- Yadav A.P., F. Suzuki, A. Nishikata, T. Tsuru, Investigation of atmospheric corrosion of Zn using ac impedance and differential pressure meter, *Electrochim. Acta.* 49 (2004) 2725–2729. doi:10.1016/j.electacta.2004.01.033.
- Yadav A. P., Nishikata A. and Tsuru T., 2004, Electrochemical impedance study on galvanized steel corrosion under cyclic wet–dry conditions-influence of time of wetness, *Corrosion Science*, Vol. 46, pp. 169–181.
- Yunze He, Guiyun Tian, Hong Zhang, Mohammed Alamain, Anthony Simm, Paul Jackson, 2012, Steel corrosion characterization using pulsed eddy current systems, *IEEE Sensors Journal*, Vol. 12, No. 6, pp 2113-2120.

List of Publication

A. Patent Application

Patent application number of Patent: 特願 2017-100295

Patent title: 信号生成装置及び方法、並びに歪測定ユニット

B. International Journal

1. “Development of Amplifier Circuit by Active-Dummy Method for Atmospheric Corrosion Monitoring in Steel Based on Strain Measurement”, Nining Purwasih, Naoya Kasai, Shinji Okazaki, Hiroshi Kihira on *Metals* 2018, 8(1), 5; 2018, IF = 1.984.
2. Atmospheric Corrosion Sensor based on Strain Measurement with an Active-Dummy FBG sensors, Nining Purwasih, Shinozaki Hiroki, Naoya Kasai, Shinji Okazaki, Hiroshi Kihira on *IEEE Transaction on Instrumentation and Measurement*, current state: All Reviewers Assigned (under review).
3. Atmospheric Corrosion Sensor based on Strain Measurement with an Active-Dummy circuit method in experiment with corrosion product, Nining Purwasih, Naoya Kasai, Shinji Okazaki, Hiroshi Kihira, will be submitted on *Corrosion Science*, Elsevier (submitted).

C. International Conference

1. “Application of Atmospheric Corrosion Sensor Based on Strain Measurement Case study in Da Nang City Vietnam and Yokohama Japan”, Asia Pacific Symposium on Safety, 2017, November 30th – December 1st, 2017, Kitakyushu, Japan, Nining Purwasih, Pham Ngoc Duc, Naoya Kasai, Shinji Okazaki, Yukihiisa Kuriyama, Hiroshi Kihira, Nguyen Duy Thao, Nguyen Lan.

C. Domestic Conference

1. “Corrosion Monitoring with Strain Measurement”, Non-destructive Testing Research Meeting of Kanagawa Prefecture, June 13th, 2017, Siera Watanabe, Nining Purwasih, Naoya Kasai, Shinji Okazaki, Hiroshi Kihira, and Yukihsa Kuriyama
2. “Atmospheric Corrosion Monitoring with Strain Measurement”, The Joint Mini Symposium on Maintenance Inspection and Non-destructive Evaluation of New Material, July 7th -8th, 2016, Nining Purwasih, Siera Watanabe, Naoya Kasai, Shinji Okazaki, Hiroshi Kihira, and Yukihsa Kuriyama
3. “Atmospheric Corrosion Monitoring with Strain Measurement”, Research Meeting of Surface NDT Method, October 24th, 2016, Nining Purwasih, Siera Watanabe, Naoya Kasai, Shinji Okazaki, Hiroshi Kihira, and Yukihsa Kuriyama
4. “Corrosion Monitoring with Optical Fiber”, Industrial, Chemical Machinery & Safety Division Conference 2017 Summer of The Japan Society of Mechanical Engineers, June 12th, 2017, Siera Watanabe, Nining Purwasih, Naoya Kasai, Shinji Okazaki and Hiroshi Kihira